Nanomechanical Systems Based on Tensile-Stressed Crystalline Indium Gallium Phosphide

Doctoral thesis for obtaining the academic degree

Doctor of Natural Science (Dr.rer.nat.)

submitted by

Maximilian Bückle

at the

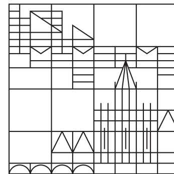

Faculty of Sciences

Department of Physics

Date of the oral examination: 13.11.2020

1. Reviewer: Prof. Dr. Eva M. Weig
2. Reviewer: apl. Prof. Dr. Johannes Boneberg

Konstanzer Online-Publikations-System (KOPS)
URL: http://nbn-resolving.de/urn:nbn:de:bsz:352-2-18flwdlcddv619

“It is oscillating...
like an oscillator.”

— M. B. (2019)

Abstract

My thesis is about nanomechanical resonators fabricated from the ternary semiconductor crystal indium gallium phosphide ($In_{1-x}Ga_xP$). The quality factor is an important characteristic of nanomechanical systems, which is often limited by material defects. This is the case for the amorphous silicon nitride, which is the gold standard material in nanomechanical systems for the past few years. Crystals have less defects than amorphous solids, and therefore the mechanical oscillation should have a higher quality factor. Additionally, the mechanical quality factor can be increased by tensile stress in nanomechanical resonators. One can epitaxially grow tensile-stressed InGaP films by changing the ratio between indium and gallium. By combining the crystallinity with a tensile stress, InGaP nanomechanical resonators have the prospect of achieving exceptional quality factors, which makes them a possible candidate for future sensor applications.

There has not yet been much research on nanomechanical systems based on tensile-stressed crystalline materials, since most crystals cannot be grown under strong tensile stress. The main task during the beginning of my thesis project was to develop fabrication processes for InGaP nano resonators. With these developed processes it is possible to reliably fabricate free-standing InGaP nano-resonators. The vibrations of those resonators are detected with a laser interferometer. This way I am able to determine the mechanical properties of the resonators. I show that the tensile stress depends on the orientation of the resonators with respect to the crystal orientation. This enables control over the tensile stress and therefore over the resonance frequency of the resonator. I also show a dependence of the tensile stress on the length of the resonator. This previously unknown effect is independent of the resonator material and is explained by a theoretical model based on elastic theory. The tensile stress of InGaP resonators reaches values of up to $775\,\mathrm{MPa}$ for a gallium content of $59.2\,\%$.

In addition, I investigate the mechanical quality factors, which show values up to $300\,000$ for resonance frequencies around $1.5\,\mathrm{MHz}$. The intrinsic Q of InGaP is on the order of high-stress amorphous SiN, presumably limited by surface altering

effects. Because exposure to air degrades the quality factors I also look into possible ways to passivate the resonators to protect them from the ambient air.

This research establishes InGaP as a crystalline, yet tensile-stressed and a high Q nanomechanical system. Additionally, InGaP profits from a suppressed two-photon absorption at telecom-wavelengths, which makes it a promising material for integrated optomechanical systems.

Zusammenfassung

In meiner Arbeit geht es um nanomechanische Resonatoren hergestellt aus dem Halbleiterkristall Indiumgalliumphosphid ($In_{1-x}Ga_xP$). Kristalline Materialien haben in der Regel weniger Defekte als amorphe Festkörper, was zu einer verringerten Dämpfung der mechanischen Schwingungen führen sollte. Außerdem erhöht Zugspannung die mechanische Güte in nanomechanischen Resonatoren. Eine InGaP Schicht lässt sich, je nach Mischungsverhältnis von Indium und Gallium, epitaktisch und zugverspannt wachsen. Durch beide Effekte, niedrige Defektdichte und hohe Zugspannung, sollte InGaP ein Material für ausgezeichnete mechanischen Güten und somit ein möglicher Kandidat für künftige Sensortechnik sein.

Zugverspannte kristalline Materialien für nanomechanische Systeme sind bisher kaum erforscht, da sich nur wenige Kristalle zugverspannt wachsen lassen. Zu Beginn meines Promotionsprojektes ging es deshalb darum, Fabrikationsprozesse zu entwickeln. Mit diesen Prozessen können zuverlässig freitragende InGaP Nanoresonatoren hergestellt werden. Die Schwingungen der fertigen Resonatoren werden anschließend mit einem Laser interferometrisch vermessen, um daraus ihre mechanischen Eigenschaften zu bestimmen. Damit konnte ich zeigen, dass die Zugspannung von der Kristallrichtung abhängt, wodurch man gezielt Kontrolle über die Stärke der Zugspannung erhält. Ich zeige auch, dass die Zugspannung von der Resonatorlänge abhängt. Dieser bisher noch unbekannte Effekt ist materialunabhängig und kann durch ein theoretisches Modell erklärt werden, das auf der Elastizitätstheorie basiert. Die Zugspannung von InGaP Resonatoren erreicht Werte von bis zu $775\,\mathrm{MPa}$ für einen Galliumanteil von $59.2\,\%$.

Außerdem habe ich die mechanischen Güten der Resonatoren untersucht, welche Werte bis zu $300\,000$ zeigen. Die intrinsische Güte von InGaP ist in der Größenordnung von stark zugverspanntem, amorphen SiN und wahrscheinlich durch Oberflächeneffekte limitiert. Jedoch greift Umgebungsluft die Resonatoren an und sorgt für eine Verschlechterung der Güten. Deswegen habe ich Möglichkeiten der Passivierung untersucht, um die Resonatoren vor der Umgebungsluft zu schützen.

Diese Forschung etabliert InGaP als ein nanomechanisches System mit hohen Güten und umfangreicher Kontrolle über die Zugspannung. Des Weiteren profitiert InGaP von unterdrückter Zwei-Photonen-Absorption im Telecom Wellenlängenbereich, wodurch es ein vielversprechendes Material für integrierte optomechanische Systeme ist.

Acknowledgments

Here is the place where I can *give credit where credit is due*. To everyone that helped and supported me during my time as PhD student.

First and foremost I have to thank you *Eva*. You gave me the opportunity to work on this project. Already in a student seminar, during my master studies, you got me excited about nanomechanics and introduced me to a very interesting research field with a great scientific community. As I was one of your first students, I could watch the group growing as you attracted many great people and built up a nice group here in Konstanz. With your calm nature, you create a nice group atmosphere and working environment. You let me independently work on the project, but when I needed some advice or encountered a problem you always found some time to discuss it. During those years I could grow a lot on a professional and personal level. I will look back to many awesome years. Thank you for the good and interesting times.

Prof. Johannes Boneberg, I thank you for agreeing to be the second reviewer and taking your time to read and review this thesis. I also thank you together with *Prof. Peter Nielaba* to be the examiners for my PhD defense.

I thank my collaborators on this PhD project.

Rémy Braive at the Centre de Nanosciences et de Nanotechnologies, CNRS, Université Paris-Saclay for the collaborating work on InGaP and sharing of new InGaP wafers for investigation.

Ivan Favero at the Université Paris Diderot for collaborating in surface passivation of InGaP, namely the ALD of alumina on the string resonators.

And also *Jörg Grenzer* at the Helmholtz-Zentrum Dresden-Rossendorf for all the XRD measurements and the fruitful discussions about crystalline systems.

Special thanks go out to *Garrett* and *Claus*. Since both of you have traveled the world quite a bit, I am not sure if I should still associate you to the University of

Vienna, but that is were the stressed InGaP nanomechanics started out. First of all, thank you for sharing some of your InGaP wafers with us to get my PhD project started and also the many great discussions about fabrication in order to tackle all the problems of the first wafers. Garrett, I am amazed how you always dug out some papers from your grad school days when we encountered new problems, and this all the while you also managed your company. Claus, you probably know better than anyone else the joys of the initial InGaP fabrication. It was really nice and helpful to have someone to talk about InGaP and I am grateful for the collaboration. In the end we managed the InGaP fabrication and got some great results.

When it comes down to nanofabrication in Konstanz, no one gets around you *Matthias*. You are the heart of the Nanolab and keep things running. You were and are always available when I needed some fabrication advise and always continued to improve the fabrication conditions in the lab. Not to mention all the times we spent together taking care of the ICP. Thank you for all the help and support in fabrication.

All the past years I spent on this PhD project I was surrounded by an amazing group of colleagues that also became dear friends. Besides all the physics and work stuff, we also did super nice leisure activities together, might it be spending time at the lake, doing game nights, cooking dinner together, making liquid nitrogen ice cream or just going for drinks. Thanks to all former and current group members for the amazing time.

Big thanks to my former students *Valentin* (Master Thesis) and *Nathanael* (Bachelor Thesis). You were always highly motivated and did a fantastic job in the lab. With your contributions we gained many interesting insights on InGaP.

Wenn man das Reich der Nano- und Micromechanik verlässt, dann ist *Louis* einfach der Meister wenn es um Grob- und Feinmechanik geht. Ohne dich würden die Versuchsaufbauten wohl nur halb so gut funktionieren, da du immer tolle und vor allem nützliche Ideen einbringst, welche alles nochmal deutlich verbessern. Dabei habe ich persönlich auch viel über Feinmechanik und allgemeines Handwerken gelernt. Außerdem habe ich die Zeit mit dir im Büro sehr geschätzt, inklusive den kleinen Pausenplauschs und dem dazugehörigen Stückchen Schoki.

Only saying "Thx *Juliane*" might be concise and enough for a Swabian, but this would be simply too short. You have been a awesome office buddy and are a good friend. May it be Spätzle or just some drinks. We had a lot of interesting conversations as well as controversial discussions, where we many times agreed to disagree. It was and is always a pleasure talking and discussing with you.

Katrin you were also someone I spent many years together, going back to the Master Thesis. We had good times at the Uni, in the labs or at conferences. But you are also a good friend and you were always in for non-work-related activities. You showed me that Fasnacht can be fun, when you have the right people around you.

Alexandre, even though we had opposite organization styles ;) you always had a helping hand when I had a question about optics.

Your knowledge about bikes was quite helpful to me *Yannick*. But the length dependent stress gave us quite a headache, I guess we finally understand everything(?). Anyhow, we could always find something funny to laugh about, even if it is only a watermelon in a slingshot.

Felix you somewhat turned out to be the most stoic person in our group. But when you liven up it is always a fun time, may it be in the office, the lab or during sailing lessons.

Jana, as an ambassador of the Reichenau you showed me nice places and fun cultural events on your small island. It is a really nice place.

Tuan you are probably the most Bavarian Asian I know. Nonetheless, it is always fun spending time with your lively personality.

Learning a new language can be hard. My (nearly) perfect Spanish came as far as: *perdona*. But you are more than a Spanish teacher *Irene*, we actually talked more about gender-related topics. It is a good thing to promote physics for everyone, independent of their background.

Writing is definitely not my forte, but I did it (somehow). This version would not have been possible without all the people proof-reading parts of my thesis. Many thanks go to (sorted in alphabetical order): *Claus*, *Dave*, *Eva*, *Felix*, *Irene*, *Jana*, *Juliane*, *Pia*, *Tuan*, and *Yannick*. With all your helpful input you got me out of my tunnel vision and making this a better thesis.

Close to the end I want to thank my *parents* and *family*. You raised me to be an open-minded and curious person (at least that is what I think about myself). You were supporting me in every possible way all my live and during my student years. Thank you for everything.

Last but not least I have to thank you *Pia*. The past years with you have been very enjoyable and I hope there are many more to come. Also thank you for all your support during my writing-time in general and in particular in times of the COVID-19 pandemic.

Without the contribution of all you people, this PhD project and thesis would not have turned out the way it did. Thank you very much.

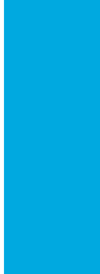

Contents

Abstract iii

Zusammenfassung v

1 Introduction 1

2 Basics 5
- 2.1 Nanomechanical Systems . . . 5
  - 2.1.1 Flexural Vibrations of Elastic Bodies . . . 5
  - 2.1.2 Dissipation Dilution Model . . . 7
- 2.2 Indium Gallium Phosphide . . . 8
  - 2.2.1 Crystal Structure . . . 8
  - 2.2.2 Lattice Mismatch and Strain . . . 9
  - 2.2.3 Critical Thickness . . . 10
  - 2.2.4 Calculating Young's Modulus . . . 12

3 Fabrication 15
- 3.1 Electron Beam Lithography . . . 17
- 3.2 Reactive Ion Etching . . . 21
- 3.3 Wet Etching . . . 26
- 3.4 Freely Suspended InGaP String Resonators . . . 28
- 3.5 Degradation of High Al Content AlGaAs . . . 30

4 Mechanical Characterization 33
- 4.1 Interferometric Setup . . . 33
- 4.2 Choice of Wavelength . . . 35

5 Orientation Dependent Stress 39

6 Length Dependent Stress 45

6.1 Finite Element Method Simulations 48
6.2 Theoretical Stress Model 50
6.3 Discussion 54

7 Quality Factor Measurements 57
7.1 Quality Factors and Intrinsic Q 57
7.2 Degradation in Ambient Conditions 62
7.3 Passivation by Atomic Layer Deposition 65

8 Conclusion 69

A InGaP Wafers 73

B Fabrication Details 77

C High Resolution X-Ray Diffraction Measurements 81

Bibliography 87

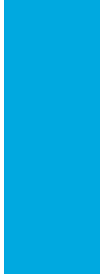

List of Figures

2.1 Sketch of the two fundamental flexural modes of doubly-clamped beam resonators 6
2.2 Crystal structure of InGaP 8
2.3 Miller indices and crystal orientations 9
2.4 Lattice mismatch. 11
2.5 Critical thickness, calculated for $In_{1-x}Ga_xP$ on GaAs 12
2.6 Young's modulus of InGaP 14

3.1 Schematic fabrication flow for doubly-clamped string resonators 16
3.2 Schematic write fields for electron beam lithography 17
3.3 Delamination of resist 18
3.4 Comparison of resist development 20
3.5 Schematic of an ICP etcher 22
3.6 SEM images of ICP etching without and with thermal coupling 24
3.7 ICP etch rate vs. table temperature 25
3.8 Phase diagram of CO_2 for critical point drying 28
3.9 Freely suspended InGaP string resonators 29
3.10 AlGaAs degradation under ambient conditions 30
3.11 Destruction of InGaP string resonators due to AlGaAs degradation 31
3.12 RTO treated sample 32

4.1 Schematic of the mechanical characterization setup 34
4.2 A typical frequency response of an InGaP string resonator 35
4.3 Frequency shifts due to laser heating 36
4.4 InGaP string resonator destroyed due to high laser irradiation 36

5.1 Epitaxial heterostructure 40
5.2 Orientation dependent resonance frequencies 40
5.3 Angle dependent Young's modulus in $In_{1-x}Ga_xP$ 41
5.4 Angular stress dependence of tensile-strained $In_{1-x}Ga_xP$ string resonators 42

5.5 Reciprocal space maps and cathodoluminescence measurements 43
5.6 Angle dependent change ΔE of the Young's modulus 44

6.1 Schematic design of string resonators 46
6.2 Eigenfrequencies of the out-of-plane modes as a function of the mode number for InGaP string resonators 47
6.3 Tensile stress of InGaP string resonators vs. resonator length 47
6.4 Eigenfrequencies and tensile stress of SiN string resonators 48
6.5 Stress values extracted from FEM simulations for different pedestal heights 49
6.6 Stress values extracted from FEM simulations for different undercuts . . 49
6.7 FEM simulation of the stress distribution and the resulting deformation 50
6.8 Sketch for the theoretical model of length dependent stress 52
6.9 Experimentally determined tensile stress as a function of the length of the string resonators 55

7.1 Frequencies and tensile stress of wafer 5LS 58
7.2 Quality factor vs. mode number of the wafers 3HS and 4HS 59
7.3 Quality factor vs. mode number of string resonators fabricated from the low-stress wafer 5LS 60
7.4 Intrinsic Q of InGaP string resonators vs. resonator length 60
7.5 Q factors and intrinsic Q of SiN string resonators 61
7.6 Influence of ambient air on the frequency 63
7.7 Tensile stress vs. resonator length before and after air exposure 63
7.8 Influence of ambient air on the Q factor 64
7.9 Influence of ambient air on the intrinsic Q 64
7.10 Frequency vs. mode number before and after ALD of alumina 66
7.11 Tensile stress vs. resonator length before and after ALD of alumina . . 66
7.12 Quality factor vs. mode number before and after ALD of alumina . . . 67
7.13 Influence of ambient air on the intrinsic Q 67

C.1 HRXRD reciprocal space maps depicting the symmetric 002 and 004 and asymmetric 224 reflections of the 1HS wafer for a x-ray beam oriented along the $[110]$ direction 82
C.2 HRXRD reciprocal space maps depicting the symmetric 002 and 004 and asymmetric $\overline{2}24$ reflections of the 1HS wafer for a x-ray beam oriented along the $[\overline{1}10]$ direction 83
C.3 HRXRD reciprocal space maps depicting 404 and 044 reflection of the 1HS wafer 83
C.4 HRXRD curve of the 002 reflection of the 1HS wafer 84
C.5 HRXRD reciprocal space maps depicting the symmetric 002 and 004 and asymmetric 224 reflections of the 2LS wafer for a x-ray beam oriented along the $[110]$ direction 84

C.6 HRXRD reciprocal space maps depicting the symmetric 002 and 004 and asymmetric $\overline{2}24$ reflections of the 2LS wafer for a x-ray beam oriented along the $[\overline{1}10]$ direction 85
C.7 HRXRD reciprocal space maps depicting 404 and 044 reflection of the 2LS wafer 86

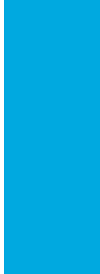

List of Tables

2.1 Miller index notation for cubic crystals 9

3.1 Electron beam lithography exposure parameters 20

6.1 Geometric parameters of the investigated samples 51
6.2 Mechanical parameters of the investigated samples 51
6.3 Calculated and fitted parameters of the investigated samples 54

A.1 Structure of wafer 1HS 73
A.2 Structure of wafer 2LS 74
A.3 Structure of wafer 3HS 74
A.4 Structure of wafer 4HS 75
A.5 Structure of wafer 5LS 75

B.1 Fabrication preparations 77
B.2 Lithography 78
B.3 Etching 79
B.4 Wet etch solutions and etch rates 79

C.1 Heterostructure of the 1HS wafer 85
C.2 Nominal heterostructure composition of the 1HS wafer 86

Acronyms

AFM	atomic force microscope
ALD	atomic layer deposition
AlGaAs	aluminum gallium arsenide
BHF	buffered hydrogen fluoride
CPD	critical point dryer
CL	cathodoluminescence
DC	direct current
DI	deionized
EBL	electron beam lithography
GaAs	gallium arsenide
HF	hydrogen fluoride, hydrofluoric acid
HRXRD	high resolution x-ray diffraction
IC	integrated circuit
ICP	inductively coupled plasma
InGaP	indium gallium phosphide
IPA	isopropyl alcohol
KOH	potassium hydroxide
MBE	molecular beam epitaxy

MEMS microelectromechanical system

MOCVD metalorganic chemical vapour deposition

MOVPE metalorganic vapour-phase epitaxy

NEMS nanoelectromechanical system

PBS polarizing beam splitter

PD photodiode

PZT piezoelectric transducer

Q quality (factor)

RF radio frequency

RIE reactive ion etching

RSM reciprocal space map

RTA rapid thermal annealing

RTO rapid thermal oxidation

sccm standard cubic centimeters per minute

SEM scanning electron microscope

SiN silicon nitride

VNA vector network analyzer

XRD x-ray diffraction

Chapter

1 Introduction

In his 1959 lecture "There's Plenty of Room at the Bottom" Richard Feynman envisioned the field of nanotechnology and the accompanying efforts towards miniaturization.

Shortly after, the first computers using integrated circuit (IC) chips appeared in the 1960s, which replaced computers based on vacuum tubes. This considerably reduced their size and increased the computation power. The developments in microfabrication enabled further scaling down of the chips.

Nowadays everyone can carry a computer in the form of a smartphone in the palm of their hand. These smartphones are not only highly sophisticated computers, but also feature a whole set of different sensors like accelerometers or gyroscopes. These types of sensors are based on microelectromechanical systems (MEMS) that also emerged from the developments in IC fabrication technology [1]. As fabrication technology continues to scale down so do electromechanical systems. Current research is on a sub-micron and nano-meter scale, exploring nanoelectromechanical systems (NEMS).

Because NEMS have a very small mass and size they can measure extremely small masses [2–6] and extremely weak forces [7–9]. Another important feature of NEMS is that they dissipate very little energy, which is evident from the small line width or the high quality (Q) factor [10]. Thus NEMS devices are strongly affected by external damping mechanisms. A high sensitivity is crucial for many sensing applications, therefore the Q factor of NEMS is continuously improved.

Resonators made from single-crystal materials show very high intrinsic quality factors. At room-temperature single-crystal silicon cantilevers have Q factors of up to $100\,000$ [11] and single-crystal diamond cantilevers can even reach values of up to 1 million for resonance frequencies in the $30\,\mathrm{kHz}$ regime [12].

Cantilevers fabricated from amorphous silicon nitride (SiN) only show quality factors of up to $30\,000$ [13]. The reason for this are additional defects in amorphous solids [14, 15], which increase the dissipation and thus reduce the Q factor. Despite those defects SiN has evolved to a standard material in nanomechanics in recent

years. This is due to the fact that amorphous SiN films can be grown tensile-strained. Dissipation dilution [16, 17] that arises from the high tensile stress in silicon nitride leads to high quality factors of several $100\,000$ at room temperature and resonance frequencies in the $10\,\mathrm{MHz}$ regime [18–21]. Additional soft clamping and stress engineering can further increase the Q by a few orders of magnitude [20, 22, 23].

Combining the high intrinsic Q of crystalline materials with dissipation dilution could open a way to reach ultimate mechanical Q at room temperature.

In the recent years a few candidates emerged for tensile-strained crystalline nanomechanical resonators. Those include heterostructures of the silicon based 3C-SiC [24] and the III-V semiconductors GaAs [25], GaNAs [26] and $\mathrm{In}_{1-x}\mathrm{Ga}_x\mathrm{P}$ [27]. The ternary $\mathrm{In}_{1-x}\mathrm{Ga}_x\mathrm{P}$ (InGaP) has the advantages of a direct bandgap (for $x < 63\,\%$) and a broad strain tunability. When it is grown on GaAs wafers it can be compressively-strained, strain-free, or tensile-strained by varying the group-III composition x. For the case of tensile strain, the tensile stress value might even exceed $1\,\mathrm{GPa}$.

The prospects of InGaP in NEMS range from applications in cavity optomechanics [27–29] to coupling with quantum-electronic systems, such as quantum wells [30] and quantum dots [31]. Furthermore, InGaP has piezoelectric properties which could be used to couple optical, electrical and mechanical degrees of freedom in a hybrid system [32]. Similar systems are used to couple microwave and optical photons, to potentially enable microwave-to-optical quantum state transfer [33, 34]. Such systems additionally profit from suppressed two-photon absorption in InGaP when operating at telecom wavelengths [35]. With tensile-strained InGaP it could also be possible to combine high Q nanomechanical systems with quantum photonic integrated circuits on a single chip [36, 37].

This thesis deals with nanomechanical resonators fabricated from $\mathrm{In}_{1-x}\mathrm{Ga}_x\mathrm{P}$. The thesis is structured in the following way.

In chapter 2 I will introduce the basics of nanomechanical systems and crystals that are needed to understand the following chapters. For nanomechanical systems this mainly covers the frequency response of flexural vibrations as well as the dissipation dilution model to describe the quality factor of tensile-stressed resonators. Then I introduce the InGaP crystal with its structure and lattice mismatch for strained thin films. I also show how to calculate the critical thickness and the Young's modulus for any desired crystal direction.

Chapter 3 deals with the fabrication of free-standing, doubly-clamped InGaP resonators. The whole process flow has been implemented from the ground up, starting with the electron beam lithography going to the anisotropic dry etching and the final isotropic wet etching. I go through all process steps and address the necessary details to ensure a smooth fabrication. At the end I will address a way to protect high aluminum content AlGaAs from detrimental hydrolysis due to the exposure to ambient air.

The mechanical characterization setup and the measurement principle are described in chapter 4. The frequency response is recorded via an interferometric de-

tection scheme. The choice of laser wavelength will also be discussed, since it can strongly influence the resonance frequency and even lead to the destruction of InGaP resonators.

The finding of an orientation dependent stress are presented in chapter 5. I investigate the tensile stress of the resonators in relation to the crystal direction. The stress changes by up to $50\,\%$ as a function of the crystal orientation and reaches stress values of up to $650\,\mathrm{MPa}$. The orientation dependence arises from an anisotropic Young's modulus, which is combined with an unexpected change of elastic properties caused by defects.

In chapter 6 I look into a length dependent tensile stress of doubly-clamped string resonators. For short resonators the tensile stress increases by $20\,\%$ compared to long resonators. A similar length dependence of the stress is also visible for silicon nitride string resonators. This suggests that this effect is material independent. Together with my colleague Yannick S. Klaß, we develop a theoretical model based on elastic theory to describe this unexpected length dependence.

The quality factors of InGaP string resonators are discussed in chapter 7. I investigate and compare string resonators fabricated from $\mathrm{In}_{1-x}\mathrm{Ga}_x\mathrm{P}$ wafers with different Ga contents x. The Q factors reach values of up to $300\,000$ at room temperature. By applying the dissipation dilution model I can extract an intrinsic Q factor of up to 2400. I show that Q_{intr} depends on the wafer material, which suggests that the wafer growth conditions play a crucial role for the material quality. With the exposure to ambient air the Q factors degrade. Therefore, I test a resonator passivation by the atomic layer deposition of alumina, which is done in collaboration with the group of Ivan Favero in France.

In the end I conclude my thesis with a summary and an outlook towards future research.

CHAPTER

2 Basics

2.1 Nanomechanical Systems

This section gives a brief overview of the theoretical models used to describe the mechanical behavior of nanomechanical resonators. The first part introduces the flexural vibrations of doubly-clamped resonators that are investigated in this thesis. The second part will take a closer look on the quality factor and how it is influenced by tensile stress.

2.1.1 Flexural Vibrations of Elastic Bodies

The behavior of weakly driven nanomechanical resonators can be easily explained by a damped, driven harmonic oscillator. This is a general and quite idealized model, which assumes the movement of a point mass. Real nanomechanical systems, such as rods, strings, beams, and membranes, are elastic bodies where the mass and deformations are continuously distributed. The vibrations of such resonators are described by the Euler-Bernoulli beam theory, which describes the flexural vibrations of isotropic, linear, and homogeneous solids. In this section, I will give an overview of the main results of the Euler-Bernoulli theory that are needed for this thesis.

Figure 2.1 shows a sketch of two doubly-clamped beam resonators. A beam with a rectangular cross section $A = w \cdot h$, of width w and height h, has two orthogonal flexural modes. Vibrations normal to the substrate are called *out-of-plane* modes and vibrations parallel to the substrate are called *in-plane* modes.

For a more detailed description of flexural vibrations I refer the reader to the literature, such as Timoshenko 1990 [38], Cleland 2002 [39], or Schmid 2016 [40].

The flexural vibration of tensile-stressed beams is described by the generalized Euler-Bernoulli equation:

$$EI\frac{\partial^4}{\partial x^4}u(x,t) - \sigma A\frac{\partial^2}{\partial x^2}u(x,t) = \rho A\frac{\partial^2}{\partial t^2}u(x,t) \tag{2.1}$$

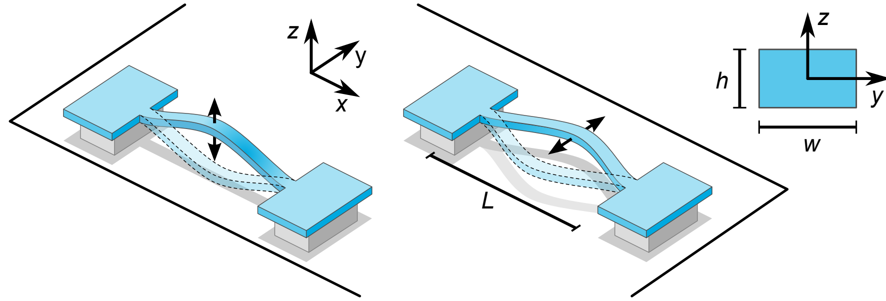

Figure 2.1: Sketch of the two fundamental flexural modes of doubly-clamped beam resonators with length L. Left: vibration mode normal to the substrate in z direction, the so-called *out-of-plane* mode. Middle: vibration mode parallel to the substrate in y direction, the *in-plane* mode. Right: cross-section of a rectangular beam with a width w and height h.

where $u(x, t)$ is the deflection at point x and time t, E is the Young's modulus, I the area moment of inertia, ρ the mass density, and σ the intrinsic pre-stress of the resonator material.

By solving this differential equation we can express the eigenfrequency of the n-th harmonic of the out-of-plane vibration as

$$f_n = \frac{n^2\pi}{2L^2}\sqrt{\frac{Eh^2}{12\rho}}\sqrt{1+\frac{12\sigma L^2}{n^2\pi^2 Eh^2}}, \tag{2.2}$$

using the area moment of inertia for a rectangular cross section $I_y = (wh^3)/12$. For the case of sufficiently strong tensile stress, lengths much greater than the thickness, and small mode numbers n, Eq. (2.2) reduces to

$$f_n \approx \frac{n}{2L}\sqrt{\frac{\sigma}{\rho}} \quad \text{for} \quad \frac{12\sigma L^2}{n^2\pi^2 Eh^2} \gg 1, \tag{2.3}$$

which describes the resonance frequency of strings.

The frequency response of the resonator modes to an external sinusoidal force F_ex, at a frequency f, can be approximated by a damped, driven harmonic oscillator with an effective mass m_eff and an effective spring constant k_eff. This leads to the mechanical susceptibility

$$u_0(f) = \frac{1}{(2\pi)^2}\frac{QF_\text{ex}}{Q\left(f_n^2 - f^2\right) + \mathrm{i} f_n f} = |u_0(f)| \cdot \mathrm{e}^{\mathrm{i}\phi}, \tag{2.4}$$

with the mechanical amplitude

$$|u_0(f)| = \frac{1}{(2\pi)^2}\frac{QF_\text{ex}}{\sqrt{Q^2\left(f_n^2 - f^2\right)^2 + f_n^2 f^2}}, \tag{2.5}$$

where Q is the mechanical quality factor and ϕ the phase difference compared to the driving oscillation. The Q factor of an harmonic oscillator can be expressed as $Q = 2\pi f_n/\Gamma$, with the damping rate Γ given by the full width at half maximum.

The general definition of Q is the ratio between the stored energy and the lost energy during one cycle at resonance

$$Q = 2\pi \frac{\text{total energy stored in the system}}{\text{energy loss during one cycle of oscillation}}. \tag{2.6}$$

2.1.2 Dissipation Dilution Model

The most basic and unavoidable dissipation is elastic loss or "internal friction" and arises from the materials itself. During the oscillation of a resonator it is periodically bending and deforming. This gives rise to oscillating stresses and strains in the material. In case stress and strain have a phase difference, the material dissipates energy. This energy dissipation can be phenomenologically modeled by considering a complex Young's modulus [16]

$$E = E_{\mathrm{Re}} + \mathrm{i}E_{\mathrm{Im}}, \tag{2.7}$$

where E_{Re} is the conventional (real-valued) Young's modulus and E_{Im} is the dissipative part also called the loss modulus. E_{Im} can be considered to be a property of the material and its defects [13]. With these parameters one can derive an intrinsic Q factor of the material itself. It is defined by the ratio

$$Q_{\mathrm{intr}} = \frac{E_{\mathrm{Re}}}{E_{\mathrm{Im}}}. \tag{2.8}$$

When a string resonator is subjected to tensile stress, its mechanical properties will be influenced. The tension from tensile stress increases the stored energy in the system, and therefore the quality factor, assuming that the dissipation is not negatively affected by an increase in tensile stress. We can see this from Eq. (2.6). The theoretical model of dissipation dilution, which was developed by several groups in the past 5–10 years, shows good agreement with the measurements [17, 41–43]. The tensile stress in the material enhances the Q_{intr} by

$$Q = Q_{\mathrm{intr}} \left(\underbrace{2\lambda}_{\text{clamping}} + \underbrace{n^2\pi^2\lambda^2}_{\text{antinode}} \right)^{-1} \quad \text{with} \quad \lambda = \frac{h}{L}\sqrt{\frac{E_{\mathrm{Re}}}{12\sigma}}, \tag{2.9}$$

where the factor in brackets is called the enhancement factor and consists of two terms. The left term is independent of the mode number and arises from the bending at the clamped ends, while the right term depends on the mode number and arises from the bending of the antinodes [42]. Since this enhancement factor is smaller than 1 for high tensile stress, it enhances the intrinsic Q. One could also say that the losses or dissipation of the material are diluted by this factor, hence the name 'dissipation dilution model'.

2.2 Indium Gallium Phosphide

This section addresses the material properties of InGaP that arise from its crystallinity. First, a brief overview of the crystal structure and crystal orientations is given. Next, lattice mismatch and the resulting strain is explained, which is the mechanism to introduce high tensile stress in InGaP thin films. Moreover, the limits of tensile stress due to a critical film thickness will be discussed. Finally, we look at the Young's modulus and its dependence on crystal directions.

2.2.1 Crystal Structure

$In_{1-x}Ga_xP$ has a zincblende crystal structure, in which the phosphide atoms are located at one sub-fcc lattice and the indium and gallium atoms share the other sub-fcc lattice. The Ga atoms take up the fraction x of the sub-fcc lattice and the In atoms the remaining $(1-x)$. The cubic unit cell is depicted in Fig. 2.2.

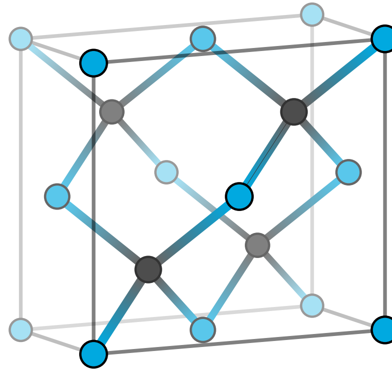

Figure 2.2: Crystal structure of InGaP. InGaP has a zincblende unit cell, where the phosphide atoms are located at one sub-fcc lattice (blue), and the indium and gallium atoms share the other sub-fcc lattice (gray).

To describe crystal-orientation-dependent material properties, we have to describe crystal orientations. For this, the Miller indices ("hkl") corresponding to an XYZ coordinate system are used to describe crystallographic planes and directions [44]. Table 2.1 lists the Miller index notation for cubic crystals.

Figure 2.3 shows some general directions and planes as well as wafer orientation and important directions for InGaP wafers. All our investigated InGaP wafers are grown on GaAs substrate wafers that have a (001) surface. The 100-nm-diameter wafers have a flat ending with a $\{110\}$ plane. Also when cleaving a (001) wafer it breaks along a $\langle 110\rangle$ crystal direction. Therefore the $\langle 110\rangle$ directions are the main directions to orient our nanoresonators on the samples.

Table 2.1: Miller index notation for cubic crystals. Taken from [44].

Notation	Meaning
$[hkl]$	Direction vector given by hkl
$\langle hkl\rangle$	Family of symmetric direction vectors equivalent to hkl
(hkl)	Crystal plane perpendicular to vector hkl
$\{hkl\}$	Family of planes equivalent to the plane perpendicular to vector hkl

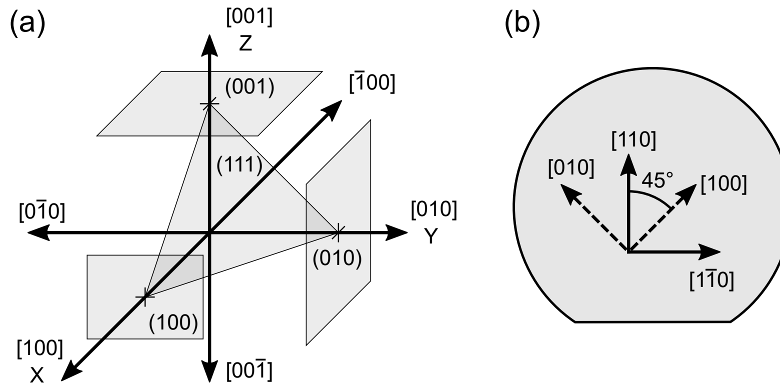

Figure 2.3: (a) Miller indices in a cubic crystal. Some important planes and directions are shown. By convention, the directions $[100]$, $[010]$, and $[001]$ are the X Y Z Cartesian axes. (b) Directions and axes in a (001) InGaP wafer. Adapted from [44].

2.2.2 Lattice Mismatch and Strain

When a thin film grows epitaxially it follows the crystalline structure and orientation of the substrate. This can be done by molecular beam epitaxy (MBE) or metalorganic vapor-phase epitaxy (MOVPE), also known as metalorganic chemical vapor deposition (MOCVD). However, there are some requirements to grow layers epitaxially on a crystalline material. The lattice constant of the layer a_{L} has to be similar to the lattice constant of the substrate a_{S}. If the difference of the respective lattice constants between the substrate and thin film to be grown are too big, crystallographic defects will be introduced, which can lead to amorphous or multi-crystalline growth. Therefore, the grown film is no longer crystalline. This condition defines which materials can be epitaxially grown on certain crystalline substrates.

This thesis deals with epitaxially grown InGaP thin films on (001) GaAs substrate wafers with a sacrificial layer of AlGaAs. The key benefit of this material system is, that the lattice constant of $\mathrm{In}_{1-x}\mathrm{Ga}_x\mathrm{P}$ can be changed by varying the Ga content x and more importantly the thin film can still be epitaxially grown even when the lattice constants differ up to a certain point.

By varying the Ga content x of InGaP, the lattice constant follows the function

$a_{\mathrm{L}}(x) = (5.8687 - 0.4182x)$ Å [45]. This results in lattice constant changes of up to 7 %. In comparison, the substrate lattice constant of $\mathrm{Al}_y\mathrm{Ga}_{1-y}\mathrm{As}$ changes by only 0.1 %, as a function of its Al content, since $a_{\mathrm{AlGaAs}}(y) = (5.6533+0.0078y)$ Å [45]. Because of this small change we assume the lattice constant of AlGaAs to equal that of plain GaAs, $a_{\mathrm{AlGaAs}} \approx a_{\mathrm{GaAs}}$.

In the case of $x = 51\,\%$, the lattice constant of InGaP equals the one of GaAs $a_{\mathrm{L}}(0.51) = a_{\mathrm{GaAs}}$, this means an InGaP layer grows strain-free (lattice-matched) on a GaAs substrate. When the composition changes, the layer is grown tensile (compressive) strained for a higher (lower) Ga content.

For cubic materials and epitaxy onto (001) substrate wafers, the applied strain in the layer is bi-axial and an initially cubic material becomes tetragonally deformed. If the substrate is several times thicker than the layer, the lattice mismatch induces lattice strain solely within the layer. The lattice mismatch is defined as [46]:

$$\delta_{\mathrm{L}}(x) = \frac{a_{\mathrm{L}}(x) - a_{\mathrm{S}}}{a_{\mathrm{S}}}. \tag{2.10}$$

Under conditions of biaxial strain, the non-vanishing strain components are [46]

$$\varepsilon^{\|}(x) = \frac{a_{\mathrm{L}}^{\|} - a_{\mathrm{L}}(x)}{a_{\mathrm{L}}(x)}, \tag{2.11a}$$

$$\varepsilon^{\perp}(x) = \frac{a_{\mathrm{L}}^{\perp} - a_{\mathrm{L}}(x)}{a_{\mathrm{L}}(x)} \tag{2.11b}$$

parallel ($\varepsilon^{\|}$) and perpendicular ($\varepsilon^{\perp}$) to the interface. $a_{\mathrm{L}}^{\perp}$ and $a_{\mathrm{L}}^{\|}$ are the lattice constants of the strained layer, as visualized in Fig. 2.4. The distorted in-plane lattice constant equals the lattice constant of the substrate $a_{\mathrm{L}}^{\|} = a_{\mathrm{S}}$, in case of a 100 % pseudomorphic layer.

With this heterostructure it is thus possible to adjust and tailor the strain in a film. However, this is only possible up to a critical layer thickness determined by the Ga content x, which will be discussed in the following section.

2.2.3 Critical Thickness

The following sections 2.2.3 and 2.2.4 are based on parts of the publication:

[47] M. Bückle, V. C. Hauber, G. D. Cole, C. Gärtner, U. Zeimer, J. Grenzer, and E. M. Weig. Stress control of tensile-strained $\mathrm{In}_{1-x}\mathrm{Ga}_x\mathrm{P}$ nanomechanical string resonators. *Applied Physics Letters*, 113(20):201903, 2018.

The calculations and writing of the manuscript was done by me.
Text and figures are reproduced from [47], with the permission of AIP Publishing.

The following section provides an overview of the existing models to calculate the critical thickness of strained epilayers, and is a summary of Refs. [48] and [49].

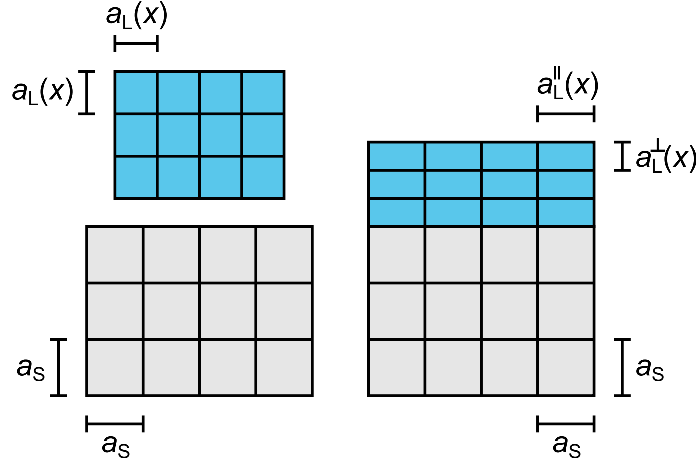

Figure 2.4: Lattice mismatch. The substrate (gray) and layer (blue) have different lattice constants, here $a_\mathrm{L}(x) < a_\mathrm{S}$. When the layer is grown on the substrate, the layer becomes tetragonally deformed so that $a_\mathrm{L}^{\|}(x) = a_\mathrm{S} > a_\mathrm{L}(x) > a_\mathrm{L}^{\perp}(x)$. This leads to tensile strain and stress in the layer.

The critical thickness is the thickness up to which a lattice mismatched thin film can grow epitaxially. Above this thickness, the layer will start to relax by introducing dislocations.

There are two different approaches to treat the generation of dislocations, which thus yield a different thickness, at which point a strained epilayer starts to relax. The first approach is the force-balancing model by Matthews 1970 [48], which considers the forces on dislocation lines. Those are misfit strain (as driving force), which is opposed by the tension in the misfit dislocation line. An epilayer starts to relax when the force exerted by the misfit strain becomes larger than the tension in a dislocation line. The other approach to calculate the critical thickness is the energy-balancing model by People & Bean 1985 [49]. It compares the homogeneous strain energy density with the energy density associated with the generation of dislocations. If the surface strain energy density exceeds the self-energy of an isolated dislocation, dislocations are introduced which lead to a relaxation.

The critical thickness for the model of Matthews is

$$h_\mathrm{c}^\mathrm{M} = \frac{b}{4\pi\varepsilon^{\|}} \frac{\left(1 - \nu\cos^2(\Theta)\right)}{(1+\nu)\cos(\alpha)} \ln\left(\frac{h_\mathrm{c}}{b}\right) \tag{2.12}$$

and for the model of People & Bean is

$$h_\mathrm{c}^\mathrm{P\&B} = \left(\frac{1-\nu}{1+\nu}\right) \frac{b^2}{16\pi\sqrt{2}\, a_\mathrm{L}\, \varepsilon^{\|2}} \ln\left(\frac{h_\mathrm{c}}{b}\right), \tag{2.13}$$

where $a_\mathrm{L}(x)$ is the lattice constant of $\mathrm{In}_{1-x}\mathrm{Ga}_x\mathrm{P}$, $b = a_\mathrm{L}(x)/\sqrt{2}$ is the magnitude of Burgers vector of a dislocation, $\nu = c_{12}/(c_{11} + c_{12})$ is the Poisson ratio of InGaP with the elastic constants c_ij, $\varepsilon^{\|}(x)$ is the in-plane strain as defined in Eq. (2.11a), Θ

is the angle between dislocation line and Burgers vector (60° for most III-V semiconductors), and α is the angle between slip direction and direction in epilayer plane which is perpendicular to the line of intersection of the slip plane and the interface (60°) [50].

By solving Eqs. (2.12) and (2.13) we obtain the curves presented in Fig. 2.5, which demonstrate that the model of Matthews gives a more conservative estimate of the critical thickness compared to the one by People & Bean. The circles in Fig. 2.5 mark the thickness and Ga contents of the investigated InGaP films. Clearly, Matthews' model is not able to describe the pseudomorphic high-stress material, which would greatly exceed the critical thickness of this model. We thus conclude that the epitaxial growth process is better described by the model of People & Bean.

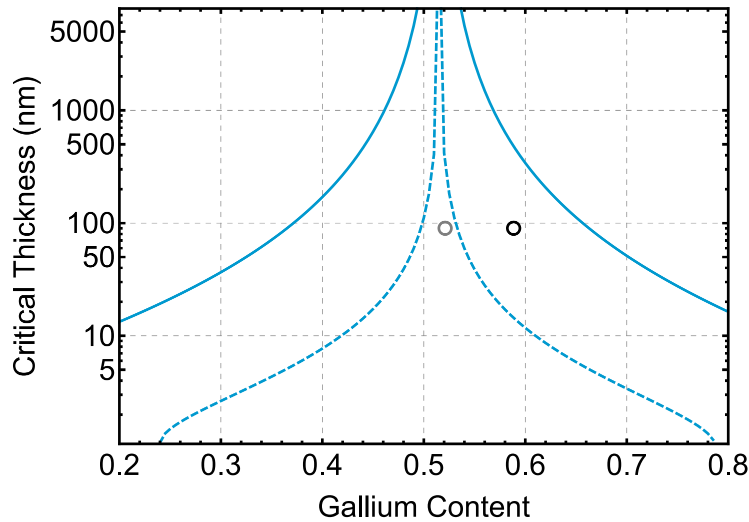

Figure 2.5: Critical thickness, calculated for $In_{1-x}Ga_xP$ on GaAs. The dashed line is the model based on the work of Matthews 1970 [48] and the solid line of People & Bean 1985 [49]. The black circle indicates the Ga contents of the high-stress wafers, which are $58.5\,\%$, $58.7\,\%$ and $59.2\,\%$. The gray circle indicates the Ga contents of the low-stress wafers, which are $51.4\,\%$ and $52.8\,\%$. InGaP films of all the wafers have a thickness between $80\,\mathrm{nm}$ and $100\,\mathrm{nm}$. The structures of the 5 different investigated wafers are given in Appendix A. Reproduced from [47], with the permission of AIP Publishing.

2.2.4 Calculating Young's Modulus

The Young's modulus relates stress and strain in the one-dimensional case of isotropic, uniaxial materials via Hooke's law $\sigma = E\varepsilon$. For anisotropic materials, stress and strain are related by the fourth rank compliance $\boldsymbol{S}$ or stiffness $\boldsymbol{C}$ tensors, $\sigma = \boldsymbol{C}\varepsilon$ and $\varepsilon = \boldsymbol{S}\sigma$ [44]. Those tensors are simplified to 6×6 matrices with three independent components, for the case of the cubic symmetry of e.g. the zincblende crystal structure. For the [100] crystal direction, the Young's modulus simply equals

the inverse first component of the compliance matrix $\boldsymbol{S}$:

$$s_{11} = \frac{1}{E}. \tag{2.14}$$

However, since we only know the elastic constants $c_{\mathrm{ij}}(x)$ of $In_{1-x}Ga_xP$ [45], we start with the stiffness matrix to calculate the Young's modulus for any desired crystal direction:

$$\boldsymbol{C}(x) = \begin{pmatrix} c_{11}(x) & c_{12}(x) & c_{12}(x) & 0 & 0 & 0 \\ c_{12}(x) & c_{11}(x) & c_{12}(x) & 0 & 0 & 0 \\ c_{12}(x) & c_{12}(x) & c_{11}(x) & 0 & 0 & 0 \\ 0 & 0 & 0 & c_{44}(x) & 0 & 0 \\ 0 & 0 & 0 & 0 & c_{44}(x) & 0 \\ 0 & 0 & 0 & 0 & 0 & c_{44}(x) \end{pmatrix}. \tag{2.15}$$

Using the rotation-matrices

$$\mathbf{Rot}_{\mathrm{X}}(\theta) = \begin{pmatrix} 1 & 0 & 0 & 0 & 0 & 0 \\ 0 & \cos^2(\theta) & \sin^2(\theta) & \sin(2\theta) & 0 & 0 \\ 0 & \sin^2(\theta) & \cos^2(\theta) & -\sin(2\theta) & 0 & 0 \\ 0 & -\frac{1}{2}\sin(2\theta) & \frac{1}{2}\sin(2\theta) & \cos(2\theta) & 0 & 0 \\ 0 & 0 & 0 & 0 & \cos(\theta) & -\sin(\theta) \\ 0 & 0 & 0 & 0 & \sin(\theta) & \cos(\theta) \end{pmatrix} \tag{2.16a}$$

$$\mathbf{Rot}_{\mathrm{Y}}(\theta) = \begin{pmatrix} \cos^2(\theta) & 0 & \sin^2(\theta) & 0 & -\sin(2\theta) & 0 \\ 0 & 1 & 0 & 0 & 0 & 0 \\ \sin^2(\theta) & 0 & \cos^2(\theta) & 0 & \sin(2\theta) & 0 \\ 0 & 0 & 0 & \cos(\theta) & 0 & \sin(\theta) \\ \frac{1}{2}\sin(2\theta) & 0 & -\frac{1}{2}\sin(2\theta) & 0 & \cos(2\theta) & 0 \\ 0 & 0 & 0 & -\sin(\theta) & 0 & \cos(\theta) \end{pmatrix} \tag{2.16b}$$

$$\mathbf{Rot}_{\mathrm{Z}}(\theta) = \begin{pmatrix} \cos^2(\theta) & \sin^2(\theta) & 0 & 0 & 0 & \sin(2\theta) \\ \sin^2(\theta) & \cos^2(\theta) & 0 & 0 & 0 & -\sin(2\theta) \\ 0 & 0 & 1 & 0 & 0 & 0 \\ 0 & 0 & 0 & \cos(\theta) & -\sin(\theta) & 0 \\ 0 & 0 & 0 & \sin(\theta) & \cos(\theta) & 0 \\ -\frac{1}{2}\sin(2\theta) & \frac{1}{2}\sin(2\theta) & 0 & 0 & 0 & \cos(2\theta) \end{pmatrix} \tag{2.16c}$$

we can perform clockwise rotations through an angle θ about a desired major crystal axis, initially X=[100], Y=[010] and Z=[001]:

$$\boldsymbol{C}(x,\theta) = \Big(\mathbf{Rot}_{\mathrm{p}}(\theta)\cdots\mathbf{Rot}_{\mathrm{q}}(\theta)\,\boldsymbol{C}(x)\Big)\mathbf{Rot}_{\mathrm{q}}^{\top}\cdots\mathbf{Rot}_{\mathrm{p}}^{\top}\;;\;\mathrm{p},\;\mathrm{q} = X,Y,Z. \tag{2.17}$$

For example, the application of $\mathbf{Rot}_{\mathrm{Z}}(45°)$ to a [100] direction produces a vector pointing along the [110] direction. By inverting the rotated stiffness matrix, we calculate the compliance matrix:

$$\boldsymbol{S}(x,\theta) = \Big(\boldsymbol{C}(x,\theta)\Big)^{-1}. \tag{2.18}$$

As in Eq. (2.14), the Young's modulus is the inverted first component s_{11} of the compliance matrix. But now it is along the rotated [100] direction, thus pointing in any desired direction:

$$E(x,\theta) = s_{11}^{-1}(x,\theta) \tag{2.19}$$

For the Young's modulus in the (001) plane, the equation can be simplified to:

$$E(x,\theta)= \frac{8(c_{11}-c_{12})(c_{11}+2c_{12})c_{44}}{c_{11}^2-2c_{12}(c_{12}-2c_{44})+c_{11}(c_{12}+6c_{44})+(c_{11}+2c_{12})(c_{11}-c_{12}-2c_{44})\cos(4\theta)} \tag{2.20}$$

which is used to calculate the contour line in Fig. 2.6 (a). A full three dimensional plot of the Young's modulus is also shown in Fig. 2.6 (b). The red line represents Eq. (2.20), which corresponds to the (001) plane.

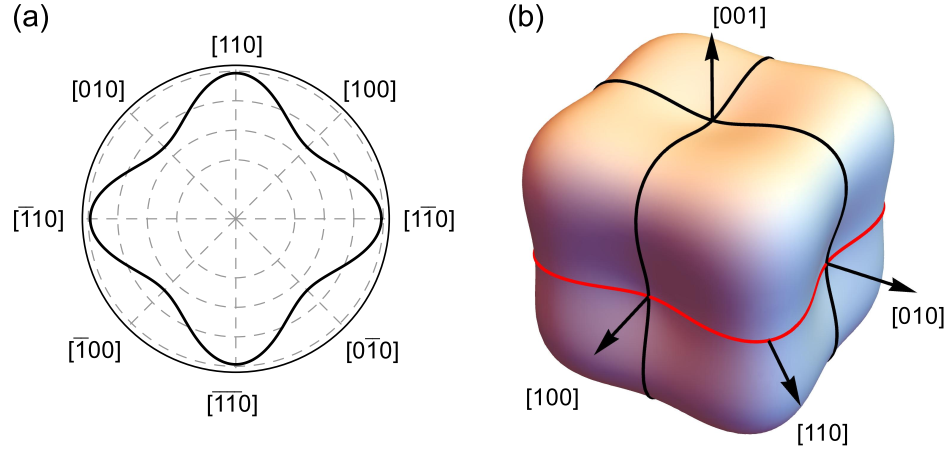

Figure 2.6: (a) Orientation dependent Young's modulus inside the (001) wafer plane, showing a 90° rotation symmetry. (b) 3D plot of the Young's modulus of InGaP. Arrows indicate major crystal directions. The solid lines correspond to the Young's modulus of the $\{100\}$ planes, the red line represents the (001) plane of (a). Reproduced from [47], with the permission of AIP Publishing.

CHAPTER

3 Fabrication

This chapter gives a general overview on how to fabricate $In_{1-x}Ga_xP$ string resonators. Since many different material compositions were investigated I will only address the general aspects for each process step. The structures of the 5 different investigated wafers are given in Appendix A. The wafer names refer to a wafer number and the tensile stress (HS for high-stress and LS for low-stress), i.e. wafer *1HS* is the first wafer and has a high tensile stress. The detailed process parameters for the different wafers are given in Appendix B.

A usual top down fabrication process consists of several different process steps to fabricate tiny nano structures. An overview of all the major fabrication steps is shown in Fig. 3.1. A more detailed explanation of the steps is given in the following sections. As a base material I use wafers consisting of several different layers on top of a substrate wafer. In the following I will only consider the most important layers that are necessary for the fabrication. The top layer is the device layer, the material used for the resonators, colored in blue in Fig. 3.1. In this work it is a thin film of $In_{1-x}Ga_xP$ with Ga content x. Below is a sacrificial layer of $Al_yGa_{1-y}As$. Those layers are epitaxially grown on top of a GaAs substrate wafer. In the first step the desired structure is patterned onto small parts of a wafer, called chips. This is done by electron beam lithography (EBL), cf. Fig. 3.1 (b)-(d), due to the small feature sizes in the range of hundreds of nanometers. A negative electron beam resist is directly used as an etch mask, which avoids an additional process step of depositing a metal or dielectric etch mask. In the second step, the previously defined pattern is transferred to the device layer by an etch process, cf. Fig. 3.1 (e). This etch process can be a wet etch or a dry etch. However, a dry etch, e.g. reactive ion etch (RIE) is preferred because of the anisotropic etch behavior, this leads to straight side walls of the defined resonator design. Afterwards the resonators are released with an isotropic wet etch, Fig. 3.1 (f). In the last step the underetched resonators are dried by means of critical point drying. This avoids stiction and destruction of the fragile nanoresonators because of the surface tension of the liquids used in the wet etch.

To protect the resonators from environmental influences, additional surface treat-

ment process steps were performed, for example rapid thermal oxidation (RTO) or atomic layer deposition (ALD).

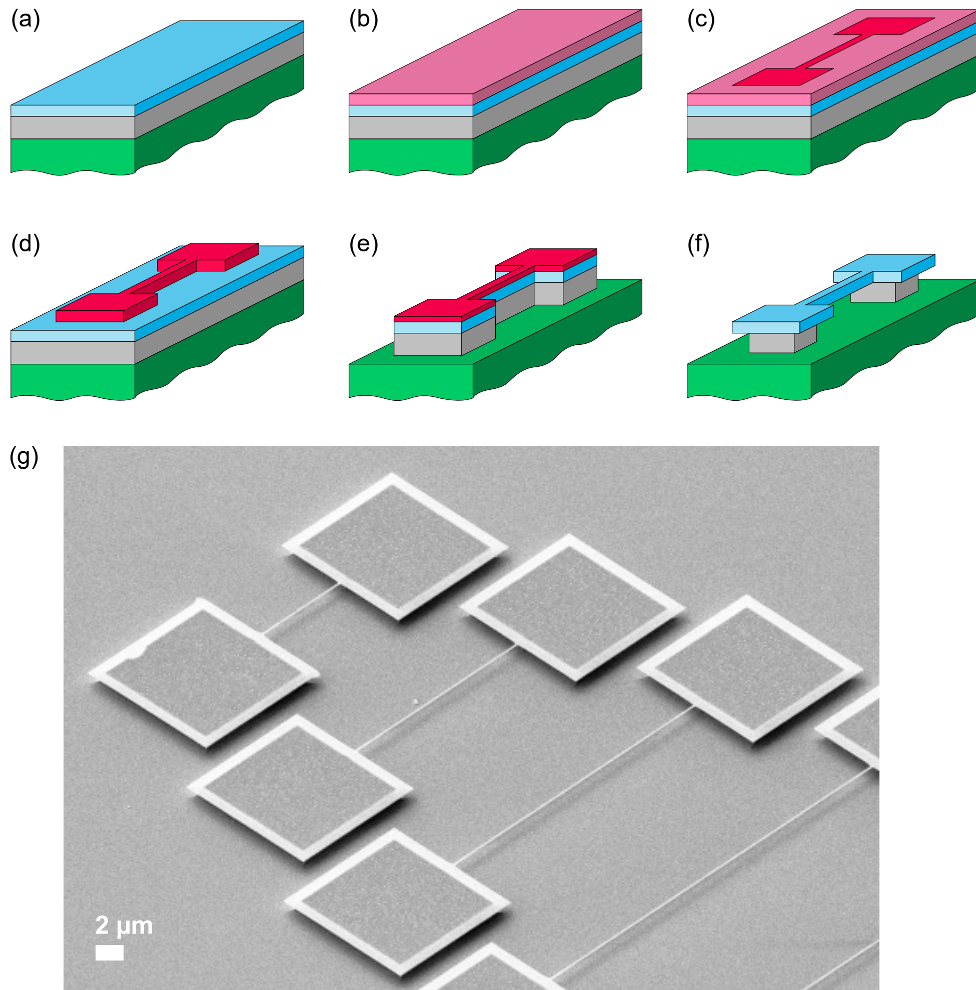

Figure 3.1: Schematic fabrication flow for doubly-clamped string resonators. (a) The most simple wafer is build up by a $In_{1-x}Ga_xP$ device layer (blue), an $Al_yGa_{1-y}As$ sacrificial layer (gray), and a GaAs substrate (green). (b) A thin layer of negative resist (pink) is spun on the sample. (c) The desired pattern (red) is defined via electron beam lithography. (d) Development leaves the exposed resist as the etch mask. (e) The pattern is transferred to the device layer by reactive ion etching. Everything that is not protected by the etch mask is etched away. (f) The resist mask is removed in an oxygen plasma, and in the end the nanoresonator is released in an isotropic wet etch. This results in the free-standing, doubly-clamped string resonators. (g) SEM image of InGaP string resonators fabricated from wafer 3HS. The bright parts are freely suspended.

3.1 Electron Beam Lithography

With electron beam lithography it is possible to define patterns in an electron sensitive resist. To fabricate string resonators like shown in Fig. 3.1, the following designs of Fig. 3.2 were used for this thesis. A typical write field, Fig. 3.2 (a)+(b) has a size of $200 \times 200\,\mu\mathrm{m}^2$ and contains several string resonator patterns with varying lengths. The string resonator structure, Fig. 3.2 (c), consists of three rectangular patterns. In the middle is a long thin string, with widths below $500\,\mathrm{nm}$ and lengths greater than $10\,\mu\mathrm{m}$. At their short ends, the strings are attached to big clamping pads, usually bigger than $8 \times 7\,\mu\mathrm{m}^2$. The clamping pads and the string usually have a small overlap to eliminate gaps in the final structure. With this design it is also possible to adjust the exposure dose of the string and pads separately.

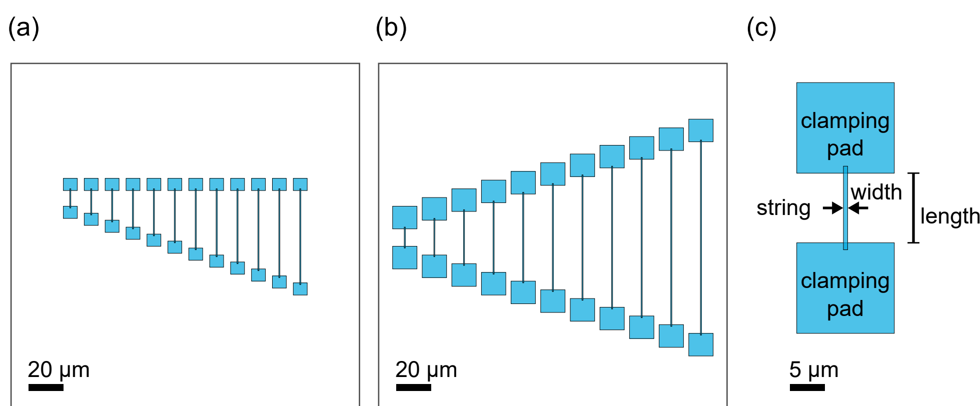

Figure 3.2: Schematic write fields for electron beam lithography. A typical write field has a size of $200 \times 200\,\mu\mathrm{m}^2$ and contains several string resonator patterns with varying lengths (blue). (a) Early write field version from the beginning of my thesis project, where the lengths range from $9\,\mu\mathrm{m}$ to $53\,\mu\mathrm{m}$ in $4\,\mu\mathrm{m}$ steps. The clamping pads have a size of $8 \times 7\,\mu\mathrm{m}^2$. Samples with this design are investigated in Ch. 5. In comparison, the updated write field layout (b) features resonators with lengths ranging from $10\,\mu\mathrm{m}$ to $110\,\mu\mathrm{m}$ in $10\,\mu\mathrm{m}$ steps, with clamping pads of the size $14 \times 13\,\mu\mathrm{m}^2$. This design is used in Chs. 6 and 7. (c) The general layout of a string resonator consists of three rectangular patterns, the string in the middle and two clamping pads at its ends. The string has a small overlap with the pads to eliminate gaps in the structure.

Design Fig. 3.2 (a) was used at the beginning of my thesis project. The samples discussed in Ch. 5 were fabricated with this design. The lengths range from $9\,\mu\mathrm{m}$ to $53\,\mu\mathrm{m}$ in $4\,\mu\mathrm{m}$ steps and the clamping pads have a size of $8 \times 7\,\mu\mathrm{m}^2$. Later, the structure was changed to design Fig. 3.2 (b). In the updated version the lengths range from $10\,\mu\mathrm{m}$ to $110\,\mu\mathrm{m}$ in $10\,\mu\mathrm{m}$ steps, so that length dependent effects can be studied better, see Ch. 6. Additionally, the size of the clamping pads was increased to $14 \times 13\,\mu\mathrm{m}^2$, based on the idea to avoid stress relaxation due to small clamping pads. Also, the measurements in Ch. 7 are done on samples with design Fig. 3.2 (b).

Preparation

Before we can start the fabrication, the heterostructure wafers are cleaved into smaller chips. Afterwards we need to clean our chips, which is necessary to ensure a uniform resist layer and a resulting high yield. This is done with a two-stage chip cleaning. First the chips are immersed in an acetone bath to remove organic residues and particles from the surface. This is followed by an isopropyl alcohol (IPA) bath to remove the contaminated acetone. One should refrain from using an ultrasonic cleaner during the acetone or IPA baths, since this can easily damage the fragile heterostructure and can lead to immediate or subsequent fracture. In the end the samples are blow dried with nitrogen and are now ready for electron beam resist application.

Resist Adhesion

Due to the hydrophobic properties of the used electron beam resist we need an adhesion promoter to avoid delamination. The problem of delamination can be seen in Fig. 3.3, where the resist structures are bent after development. This is because of insufficient contact between the resist and wafer material.

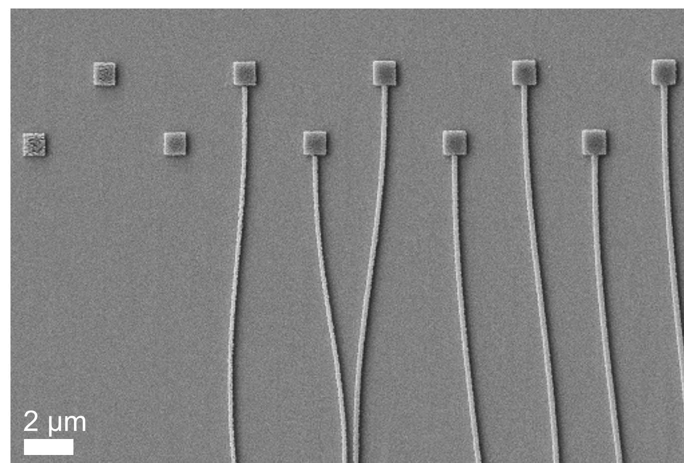

Figure 3.3: SEM picture of delaminated resist structures without adhesion promoter. Due to adhesion problems, the nominally straight structures are bent or even completely washed away (on the left) during development.

In ambient conditions, surfaces are immediately covered by several monolayers of water molecules because of the air humidity. Those water molecules form polar OH-bonds, rendering the surface hydrophilic. The resist molecules are however nonpolar and have therefore a bad affinity towards hydrophilic surfaces. Thus we need to modify the surface, in order to make it hydrophobic, water repellent and resist attractive. This is usually done by chemically binding molecules with nonpolar groups to the surface by using adhesion promoters.

TI Prime[a] is used as an adhesion promoter. It is applied by spin coating, spinning at 4000 rpm for 45 s. After the spinning only a monolayer of active substance remains on the substrate. A subsequent baking step on a hotplate for 2 min at 120 °C activates the adhesion promoter and renders the surface hydrophobic and stops water molecules from adsorbing on the surface. After cooling the substrate to room temperature the resist can be applied.

Electron Beam Resist

For the fabrication of the InGaP string resonators I chose the negative electron beam resist *ma-N 2403*[b]. A negative resist has the benefit to directly serve as an etch-mask for the later dry etch process. Therefore one can avoid additional steps to fabricate hard masks via lift-off process. This saves fabrication time and minimizes further sources of error. Especially the ma-N 2403 resist has a good etch stability for the etch chemistries used to fabricate InGaP resonators[51].

The resist is applied by spin coating to ensure a homogeneous and well defined thickness. We want to have a thin resist layer to achieve a high resolution of the lithographed structure, especially at the transition between string and clamp. This is achieved by high spin speeds, the higher the speed the thinner the layer. For this, we spin the resist at 6000 rpm for 33 s and directly softbake it on a hotplate at 90 °C for 65 s. This results in a resist thickness of about 250–270 nm after lithography and development.

Lithography

For well defined electron beam lithography one has to find the right exposure parameters. The resist needs sufficient exposure and the structures need the correct dimensions after lithography. When using a negative resist directly as a etch mask it is important to have vertical sidewalls. There are many factors that can change the lithography result. The most crucial ones are acceleration voltage, aperture size, working distance, and electron dose. All the lithography was done on a *Zeiss Crossbeam 1540XB* electron microscope. This device has two lithography systems available, which also slightly influence the result.

When using *ELPHY Plus* it was necessary to use the 10 µm aperture to achieve the low exposure dose of $40\,\mu\mathrm{C/cm^2}$, because of the slow beam speed of the pattern generator.

With the *neomicra smile2* lithography system it was also possible to use the 20 µm aperture. This enabled much faster lithography writing, due to higher electron currents. For delicate structures it can still be advantageous to use the smaller 10 µm aperture with neomicra due to a higher precision of the lower beam speeds.

[a]Microchemicals GmbH

[b]micro resist technology GmbH

The common exposure parameters are shown in Tab. 3.1. One has to note that the strings need an increased dose because of the small width. For them, the dose is increased by a factor of 1.4.

Table 3.1: Electron beam lithography exposure parameters.

Exposure dose	Acceleration voltage	Working distance
$40\,\mu\mathrm{C/cm^2}$	$10\,\mathrm{kV}$	$8.6\,\mathrm{mm}$

Development

The exposed resist is developed with the *ma-D 525*[c] developer. The development process is done in steps. First the sample is immersed in the developer for $20\,\mathrm{s}$, slowly and gently moving the sample in the liquid. Afterwards it is rinsed in deionized (DI) water for at least $30\,\mathrm{s}$ and then blow dried with nitrogen gas. This procedure is repeated four times. The DI rinsing steps in between lead to a more vertical resist profile and square corners between clamping pad and resonator, compared to only developing the structures for $80\,\mathrm{s}$ straight. This can be seen in Fig. 3.4.

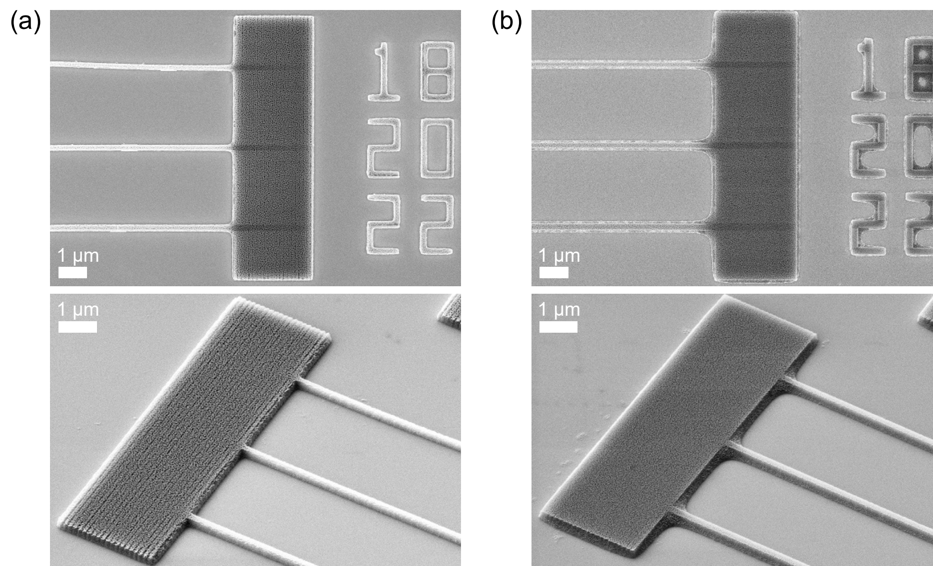

Figure 3.4: Comparison of resist development. (a) Development done in four steps of $20\,\mathrm{s}$ with rinsing in DI water between each step. (b) Development done in one step of $80\,\mathrm{s}$. With the additional rinsing steps we get sharper resist mask features. The sidewalls are more vertical and the transition from the resonator to the clamping pad is more square.

[c] micro resist technology GmbH

Hardbake

After the development a hardbake is performed. This increases the etch resistance and the thermal stability of the resist even further. The samples are baked for 10 min at 120 °C in a convection oven.

3.2 Reactive Ion Etching

This section describes the process of transferring the etch mask into the device layer. It is preferential to have an anisotropic etch process to achieve vertical sidewalls. One of the best ways to have anisotropic etching is by using an reactive ion etch (RIE). This is a dry etch process, meaning it uses reactive gases for the etching. The gas gets ionized by a high frequency electrical field. The reactive ions are then also accelerated by the field towards the sample surface. The etching therefore consists of two parts. One part is physical etching, which is done by the kinetic energy of the ions accelerated to the sample. And the other part is chemical etching by the reactive ions.

To have a better control over the ionization and acceleration of the ions, one can use an inductively coupled plasma (ICP) RIE. The InGaP samples are etched in an *Oxford PlasmaLab System 100* ICP etcher. In this machine a high frequency magnetic field is used for the ionization of gas molecules and the high frequency electric field for the acceleration. A schematic of such an etcher is shown in Fig. 3.5. The process gases are flowing through the process chamber. A coil around the top part of the chamber creates the high frequency magnetic field, which ionizes the gas and therefore supplies the inductively coupled plasma. The lower electrode, on which the samples are placed, is connected to a radio frequency (RF) power supply. Due to the small mass of the electrons they follow the oscillation of the RF field, are accelerated by it and jump into the electrodes. Because the lower electrode is connected to a capacitor, it gets negatively biased by the electrons. This generates a direct current (DC) bias between the lower and upper electrode, which in turn leads to the acceleration of the heavy ions towards the lower electrode [52]. Small samples are usually put on a carrier wafer to protect the lower electrode from being etched. For chlorine based etching, I use a silicon carrier wafer. One has to keep in mind, that the conductivity of the carrier wafer can influence the DC bias and therefore the etch result, e.g. when using an insulating SiO_2 carrier wafer instead of a semiconducting Si one.

Process Gases

To etch III-V semiconductors on GaAs or InP basis a chlorine based etch process is usually used. Our developed process to etch InGaP uses a mixture of $SiCl_4$ and Ar as reactive gases. Ionizing $SiCl_4$ provides chlorine ions for the chemical etching, while the inert Ar gas contributes to the physical etching by high energy collisions with the surface atoms. The ratio of $SiCl_4$ to Ar can therefore control whether the etching is

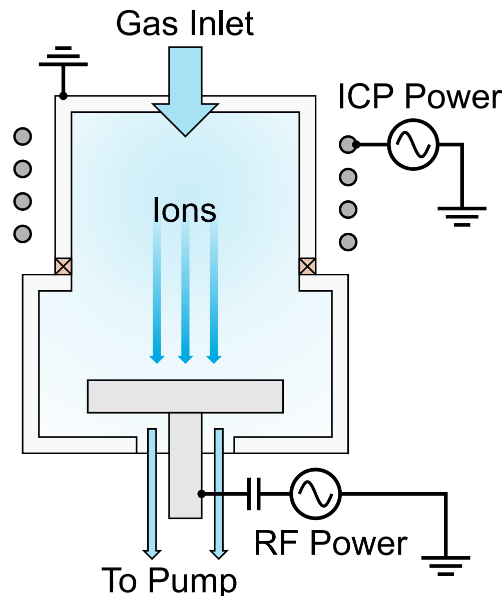

Figure 3.5: Schematic of an ICP etcher. The process gases flow through the process chamber. A coil around the top part of the chamber supplies the inductively coupled plasma, where the ions are generated. A high frequency electric field leads to the acceleration of the ions towards the lower electrode in the middle where the sample is situated.

more chemical or physical. The addition of Ar further facilitates the plasma ignition, even at lower pressures. For good etch results the literature [51] suggests a $SiCl_4$/Ar ratio of 1/3. This ratio already produced good etch results. Therefore no further studies were performed to investigate the gas composition.

Pressure

Since an anisotropic etch process is preferred, a low pressure is chosen. At low pressure there are less radicals in the etching chamber. This leads to less collisions between the radical from the point of acceleration towards the sample surface, which would divert the radicals from their straight vertical path. Thus the etch process gives more vertical etch results. Because a lower pressure uses less gas inside the process chamber, the etch rate is slightly reduced. This can be easily compensated by longer etch times. A low pressure of $1.5\,\mathrm{mTorr}$ showed good results. However, at this low pressure the plasma did not always ignite and is less stable. Therefore a slightly higher pressure of $1.7\,\mathrm{mTorr}$ was chosen, which gives similar good etch results while the process runs stable.

Power

Another important process parameters are the ICP and RF power. Those can influence the plasma density and the impact energy of the ions.

The power in the ICP coil generates most of the ions. By increasing this power more gas is ionized, this generally leads to an increase of the etch rate. However, very high ICP powers generate high magnetic fields that can confine the ions in the top of the process chamber, see Fig. 3.5. This can slightly decrease the etch rate.

The RF power accelerates the ions towards the sample. An increased RF power leads to higher etch rates, due to the higher kinetic energy of the ions. This energy puts more stress on the etch mask because it has to withstand higher impacts.

In the used ICP etch system a RF power of $60\,\mathrm{W}$ and an ICP power of $250\,\mathrm{W}$ showed the best etch results.

Temperature

Etching of InGaP can have some difficulties because of the higher average bond energy (compared to AlGaAs) and the formation of low volatile reaction products $InCl_z$ when using a chlorine-based etch chemistry [53, 54]. For this process elevated temperatures are needed for etching the less volatile $InCl_z$, since nonvolatile surface products can prevent etching. A chlorine chemistry etch also requires significant ion bombardment to obtain acceptable etching. However, high temperatures and substantial ion bombardment stretch the limits of the mask used, hence affecting its selectivity. Temperatures above $120\,°\mathrm{C}$ need to be avoided, because this can lead to melting and damage of the resist mask.

Nevertheless, it turned out that etching at nominally $30\,°\mathrm{C}$ without thermal coupling between sample and silicon carrier wafer already show good etch results. One can assume that the high plasma powers heat up the sample surface and increase the volatility of the indium byproducts. The good etch result was confirmed by later etch tests.

Figure 3.6 shows ICP etches on the 3HS wafer for different etch temperatures without and with thermal coupling, by adding a small droplet of Fomblin® oil between sample and carrier wafer. The samples without coupling have more vertical sidewalls. When the temperature is increased, the sidewall roughness increases as well. For a temperature of $120\,°\mathrm{C}$ it also seems that the InGaP surface is damaged. This could mean that selectivity of the resist is decreased at this high temperature, which is close to the melting temperature of the resist.

When employing thermal coupling the sidewalls are less vertical. All the samples with thermal coupling show smooth sidewalls even up to a temperature of $120\,°\mathrm{C}$.

The corresponding etch rates can be seen in Fig. 3.7. For samples without thermal coupling the etch rate is always in the range of $2.0\,\mathrm{nm/s}$. The thermal coupling reduces the etch rate at low temperatures. While the differences are only minor at higher temperatures.

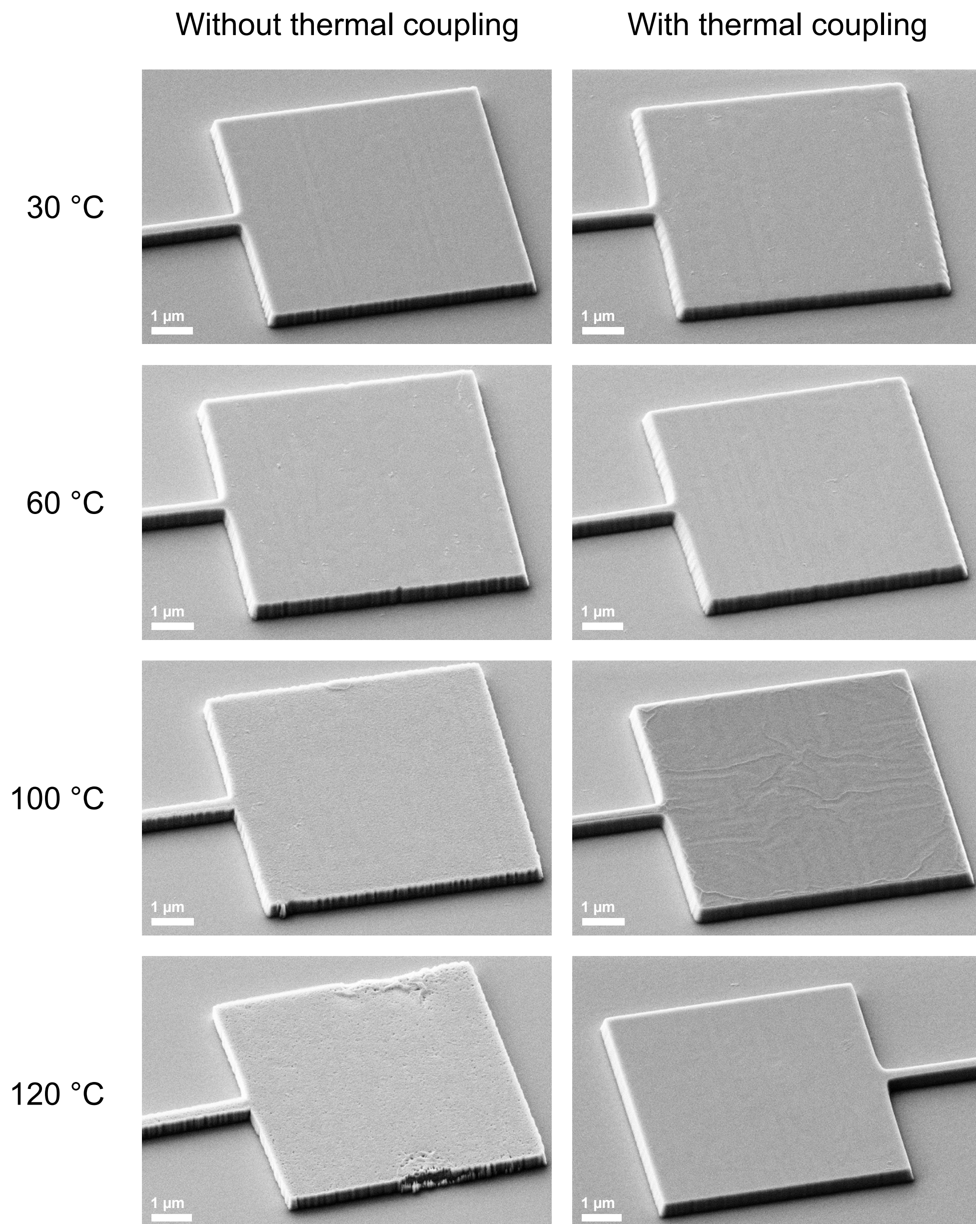

Figure 3.6: SEM images of ICP etching without and with thermal coupling. The etching was performed on wafer 3HS for different temperatures. The images on the left are without and the ones on the right with thermal coupling. The etch rate for each corresponding process is shown in Fig. 3.7.

So indeed the process without thermal coupling at 30 °C shows the best etch result, with the most vertical and smooth sidewalls.

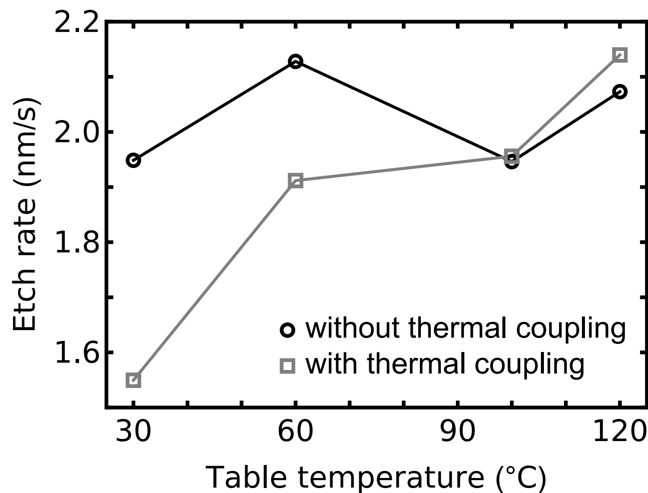

Figure 3.7: ICP etch rate vs. table temperature, corresponding to the samples in Fig. 3.6. No thermal coupling (black circle) and using Fomblin® oil to thermally couple the sample to the carrier wafer (gray squares).

Water Rinse

Etching aluminum containing materials in chlorinated gas leads to small quantities of chlorine containing residues. These include hygroscopic $AlCl_3$, that remain on the plasma exposed surface. When exposed to atmospheric conditions, hydrolysis of these species can form small quantities of hydrochloric acid (HCl), which can corrode the sample [55].

Therefore the samples are rinsed in DI water for $10\,\mathrm{min}$ immediately after the chlorine etch. This is done in order to eliminate and minimize chlorine-containing compounds that may be on the surface and their amount could increase with time in air.

Afterwards the samples are rinsed in IPA to remove further contaminations from the water and in the end blow dried with nitrogen gas.

Also the carrier wafer is thoroughly rinsed in DI water, after ICP etching is done to minimize corrosion.

Resist Removal

Due to the high powers in our ICP system, the resist mask is exposed to a lot of energy. This leads to heavy cross-linking of the resist polymers. Removal of the resist with acetone, resist-strippers or removers does not work, not even soaking the samples for several days. The only way to efficiently remove all resist residues is by using an oxygen plasma. This will oxidize and burn all the organic compounds, leaving a resist free and clean sample. Therefore, the samples are cleaned for $5\,\mathrm{min}$ in an oxygen plasma-cleaner.

3.3 Wet Etching

After the pattern is transferred to the device layer in the previous ICP process, we need to underetch the nanoresonator to make it free standing. For this we need to remove the sacrificial AlGaAs below the thin strings. We need an isotropic etch process to have etching also parallel to the sample surface. Most wet etch chemistries etch isotropically. However, some crystalline materials can have preferential etching along certain crystal directions.

More importantly we need etchants that have a high selectivity between the device and sacrificial material. This is important, so we only etch the sacrificial layer and do not attack our string resonator.

In the following subsections I will explain the used etchants for releasing InGaP string resonators on several sacrificial layer compositions, as well as additional steps to achieve a high yield and avoid destruction of the fragile structures.

Releasing of InGaP Nanoresonators

For all the investigated and processed wafers the sacrificial layer is $\mathrm{Al}_y\mathrm{Ga}_{1-y}\mathrm{As}$. However the Al content y is quite different between the wafers, it ranges from $55\,\%$ to $92\,\%$ aluminum. This difference in aluminum content can affect the etch behavior. The most common etchant for AlGaAs is hydrofluoric acid (HF), since it has a very high selectivity over InGaP or GaAs, but the etch rate of AlGaAs in HF also strongly depends on the Al content [56, 57]. For Al contents below $70\,\%$ the etch rate is quite slow, below $2\,\mathrm{nm/s}$, while higher Al contents easily achieve etch rates above $50\,\mathrm{nm/s}$.

At the beginning of my thesis project I used buffered HF (BHF)[d], which has an HF content of about $6.5\,\%$. For high Al content $\mathrm{Al}_{0.92}\mathrm{Ga}_{0.08}\mathrm{As}$ this led to etch rates in the range of 50–$90\,\mathrm{nm/s}$, slightly depending on the crystal direction. This results in etch times below $10\,\mathrm{s}$ for $300\,\mathrm{nm}$ wide resonators. Such short etch times make it hard to have good and reproducible results. The etch rate could be reduced by diluting BHF with DI water, but this would require additional HF handling.

For wafer 3HS, with the lower Al content of $y = 55\,\%$, no etching was observed in BHF for times of up to $10\,\mathrm{min}$.

To avoid handling of HF and to have an etchant for the low Al content AlGaAs, a different etch chemistry is used. The new etch chemistry uses a mixture of sulfuric acid, hydrogen peroxide and DI water, namely 1 volume part H_2SO_4 ($95\,\%$), 1 volume part H_2O_2 ($30\,\%$), and 30 volume parts H_2O. While preparing this etchant one has to mix the liquids properly, e.g. using a teflon tweezer. This is needed to always achieve the same etch rate. This etchant led to etch rates of approximately 3–$5\,\mathrm{nm/s}$ for $\mathrm{Al}_{0.55}\mathrm{Ga}_{0.45}\mathrm{As}$ and approximately $8\,\mathrm{nm/s}$ for $\mathrm{Al}_{0.85}\mathrm{Ga}_{0.15}\mathrm{As}$. With these slower etch rates it is easier to adjust the underetch depth. No significant etching of the InGaP is observed. Therefore, the selectivity is sufficiently high.

[d] *TECHNIC France BOE 7-1*

Cleaning Procedures

During fabrication residues may be deposited on the sample and could influence the mechanical properties of the resonators. These can be solid compounds such as aluminum trifluoride (AlF_3), aluminum hydroxide ($Al(OH)_3$), and other amorphous residues. To remove such residues, one can perform additional sample cleaning. The residues can be completely removed by a single digital etching cycle [58]. This is a two step process.

First the sample is immersed in an oxidizing agent, like hydrogen peroxide. This will oxidize organic residues and also a thin layer of the sample surface down to 15 Å [59].

In the second step, this thin oxide layer is removed in an oxide etching agent. This is done with a KOH solution (10 g KOH in 100 mL DI water). It could also be done with other acids or bases, but KOH has the additional advantage that it also removes other residues such as $Al(OH)_3$ [58].

This cleaning procedure is mainly used after releasing the resonators with BHF, to remove possible fluorine residues. The sulfuric acid based release already produces clean samples, since it consists of an oxidizing agent and an acid.

Critical Point Drying

After all etch processes are performed, special care in handling the samples has to be taken after the resonators are released. The thin and long strings are fragile and prone to break easily by minimal forces. Due to the wet etching of the last fabrication step, the fragile samples are in a liquid which is usually IPA as the last rinsing bath. The measurements are however performed in vacuum. Therefore the samples need to be dried.

The most general way to do this would be to simply dry it by evaporation of the liquid. But, in the last minutes of drying a droplet will form between the resonator and the substrate, and the surface tension of the liquid will pull down the string. The string will either stick to the substrate or the surface tension will even break the structure.

A much gentler method of drying is the well-known "Critical Point Drying" [60, 61]. Instead of crossing the phase boundary between liquid and gas (dashed gray arrow in Fig. 3.8) we go around this boundary to dry our sample (indicated by the solid gray arrows).

This is done by increasing the pressure and temperature of the transition liquid surrounding the sample. When you pass the critical point, the density of the "liquid" and the density of the "gas" are the same, and it is now a supercritical fluid. For this process CO_2 is a very suitable transition medium. It has a critical point of 73.8 bar and 31 °C.

The sample is still immersed in IPA when putting it into the critical point dryer. Inside the machine the IPA will be exchanged with liquid CO_2 before starting the drying process.

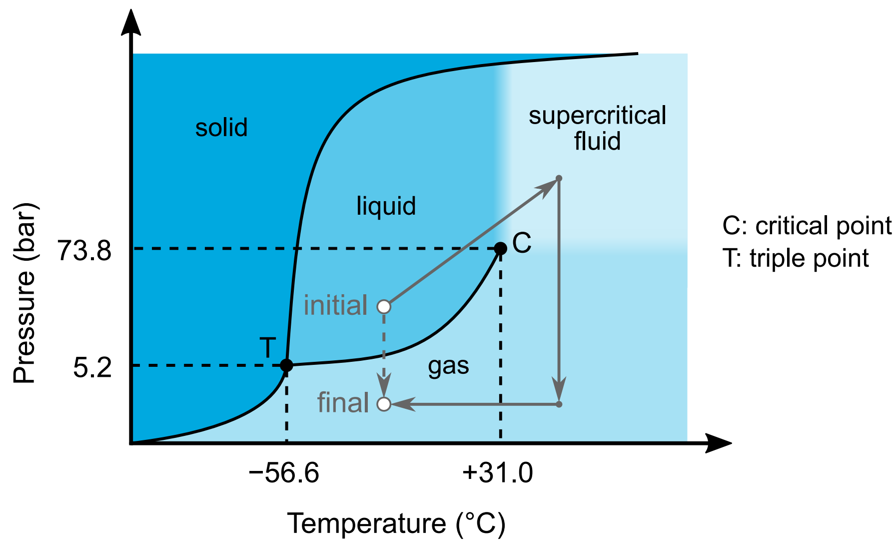

Figure 3.8: Phase diagram of CO_2. Conventional drying would follow the dashed gray arrow from the initial to final state. In this process, the transition medium would cross a phase boundary, between liquid and gaseous phase, which can damage fragile nano structures. This can be avoided by taking the alternative route of critical point drying (solid gray arrows). When we increase the temperature and pressure beyond the critical point, where the "liquid" and "gas" have the same density, it is now a supercritical fluid. We can now decrease the pressure while maintaining the temperature, this lowers the density of the transition medium until we are in the gas phase and our sample is now dry.

When the transition medium is in the supercritical phase we maintain a temperature above the critical point temperature and slowly decrease the pressure to end up in the gas phase. The sample is now dry without crossing the liquid-gas boundary and therefore avoiding the destructive surface tension.

3.4 Freely Suspended InGaP String Resonators

After carefully performing all the previously described process steps, we end up with freely suspended string resonators. A selection of resonators fabricated from the different available wafers is shown in Fig. 3.9.

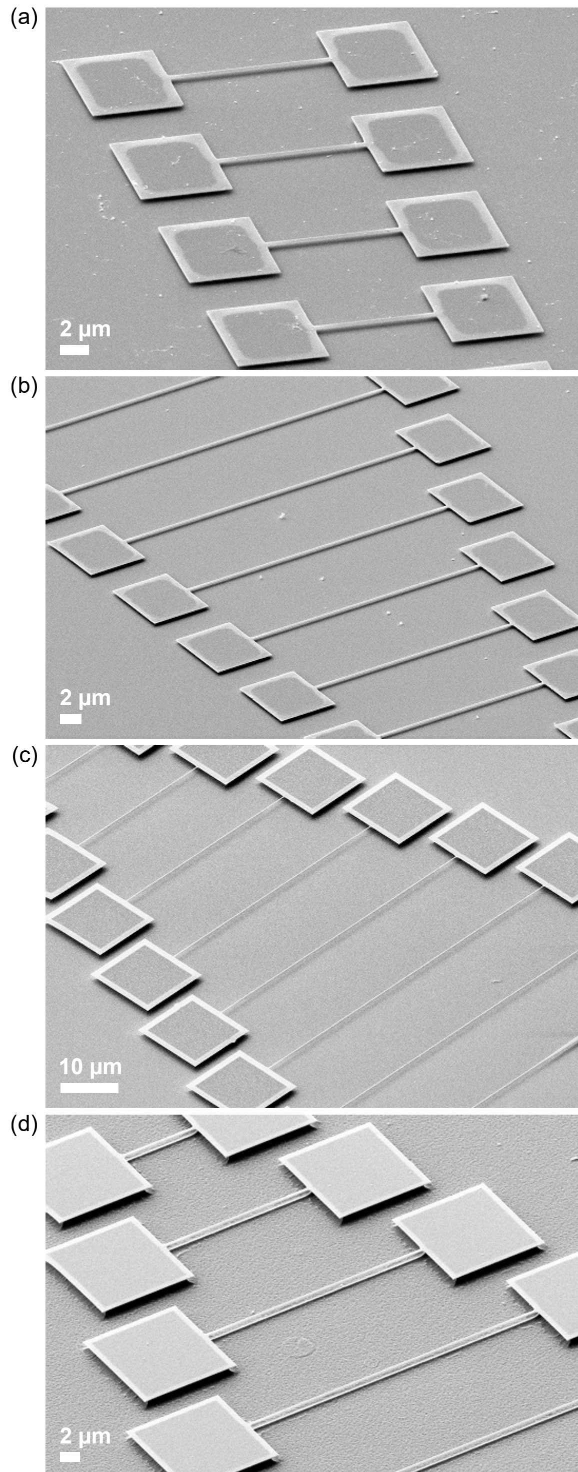

Figure 3.9: SEM images of freely suspended InGaP string resonators. (a) First InGaP string resonators where measurements were possible, fabricated from wafer 1HS. (b) Resonators from the 1HS material, with improved fabrication. (c) Strings fabricated from wafer 1HS. (d) Resonators made from the low-stress InGaP 5LS.

3.5 Degradation of High Al Content AlGaAs

The following section is based on parts of the publication:

[47] M. Bückle, V. C. Hauber, G. D. Cole, C. Gärtner, U. Zeimer, J. Grenzer, and E. M. Weig. Stress control of tensile-strained $In_{1-x}Ga_xP$ nanomechanical string resonators. *Applied Physics Letters*, 113(20):201903, 2018,

and the Master's thesis:

[62] V. C. Hauber. Herstellung von nanomechanischen Balkenresonatoren hoher Güte aus InGaP und Untersuchung der richtungsabhängigen Zugspannung des Krsitallinen Materials. Master's thesis, University of Konstanz, 2016.

Implementation of the RTO processes and the RTO experiments were done by Valentin C. Hauber during his Master Thesis under my supervision. The writing of the manuscript was done by me.
Text and figures are reproduced from [47], with the permission of AIP Publishing.

Using high aluminum content $Al_yGa_{1-y}As$ with $y > 0.9$ as sacrificial layer can pose a problem to nanofabrication. Under ambient conditions it quickly degrades and swells [63, 64], as can bee seen in Fig. 3.10. The AlGaAs layer reacts with the air humidity and swells, on the timescale of only a few days.

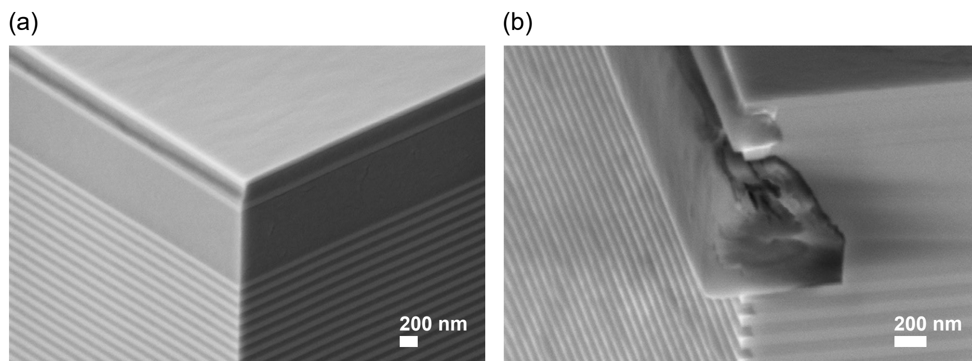

Figure 3.10: AlGaAs degradation under ambient conditions. (a) SEM image of a newly cleaved chip from the 2LS wafer. The darker areas are the high Al content $Al_yGa_{1-y}As$, the thin bright layers at the bottom are GaAs and the two bright layers atop the thick AlGaAs layer are the InGaP layers hosted by this wafer. (b) The same wafer material as in (a) after storing it 3 days under ambient conditions. The chip was cleaved along one facet right before imaging, to make the degradation visible. One can see a structural change (change in contrast) and swelling in the AlGaAs layers.

Such a swelling of sacrificial material is detrimental for nanoresonators. Figure 3.11 shows InGaP string resonators that were exposed to air. After a few days

cracks in the clamping pads are visible, already rendering the resonators useless. After a few weeks the clamping pads are completely destroyed because of the swelling of the sacrificial $Al_{0.92}Ga_{0.08}As$ layer below the clamping pads.

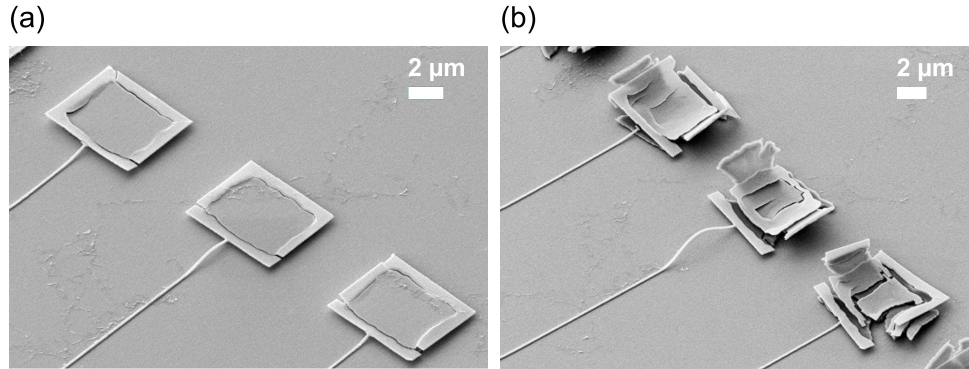

Figure 3.11: Destruction of InGaP string resonators due to AlGaAs degradation. (a) InGaP nanoresonators after a few days in ambient air. Cracks at the InGaP clamping pads are already visible due to the degradation of the underlying AlGaAs. (b) The same clamping pads as in (a) are completely destroyed after 8 weeks in ambient air.

The volume growth of the AlGaAs layer happens due to hydrolysis, where the water molecules in the air react with AlGaAs. This reaction can form several different oxygen rich compounds such as $Al_2O_3{\cdot}H_2O$, AlO(OH) or $Al(OH)_3$ [63, 64].

In order to avoid the destruction of the InGaP string resonators, one has to minimize the exposure to air. This can be done by performing the sample fabrication in one run without breaks, and afterwards put the sample immediately in the measurement setup under vacuum. This way it was possible to fabricate and measure samples from the wafers 1HS and 2LS. The results are presented in Ch. 5. For the later projects wafers with lower Al content AlGaAs layers were used, such as wafer 3HS with $Al_{0.55}Ga_{0.45}As$ and the wafers 4HS and 5LS with $Al_{0.85}Ga_{0.15}As$. Those are presented in Ch. 6 and Ch. 7. The lower Al contents made the fabrication and sample handling easier. However, as will be discussed in Ch. 7, unnecessary exposure of the sample to ambient air should still be avoided since this degrades the mechanical Q.

Rapid Thermal Oxidation

Another approach to tackle this unwanted behavior might be the passivation of the AlGaAs surface by rapid thermal oxidation (RTO) [65, 66] as shown in Fig. 3.12. So far this was only applied on AlGaAs surfaces and not yet tested on freely suspended InGaP resonators.

RTO is a dry oxidation process at high temperatures, where a thin and stable aluminum oxide film is created at the surface. Such a process is done in a rapid thermal annealing (RTA) oven in an oxygen atmosphere, hence the name rapid thermal oxidation. With a RTA oven it is possible to heat the sample in about 30 s from room

temperature to $550\,°C$. The temperature of $550\,°C$ is held for $5\,\mathrm{min}$ with an oxygen flow of $100\,\mathrm{sccm}$, and then the sample is quickly cooled down. Such a rapid process reduces the thermal impact on the material.

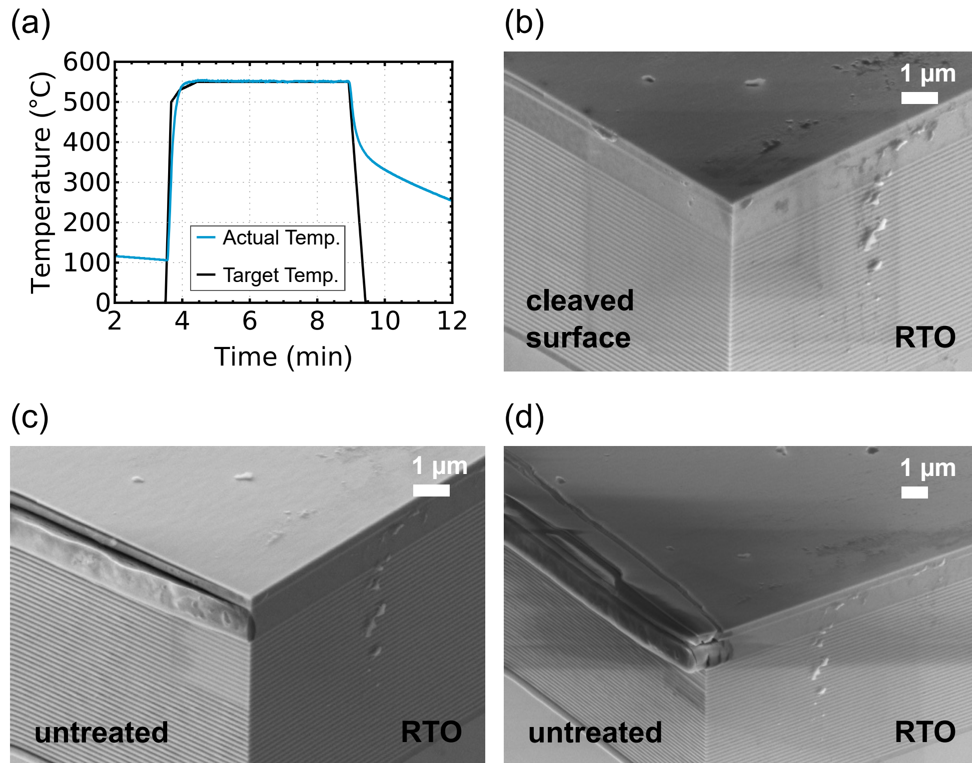

Figure 3.12: RTO treated sample. (a) Temperature profile of the $5\,\mathrm{min}$ long RTO process, with a $100\,\mathrm{sccm}$ O_2 flow. (b) Scanning electron micrograph of the heterostructure after 3 days in ambient conditions, right surface treated with RTO and left untreated surface produced by a fresh cleave right before imaging. (c) Untreated surface already shows swelling of the AlGaAs layers after 4 days. (d) Heterostructure after 21 days in ambient conditions. Untreated surface shows severe degradation from swollen AlGaAs layers while the treated surface remains unaffected.

From Fig. 3.12 we can clearly see, that RTO treatment passivates the AlGaAs against the detrimental hydrolysis. The RTO treated surface does not change when it is exposed to air. Even when exposed up to 21 days, the surface shows no signs of changes, while the untreated surface shows pronounced swelling after a few days.

Whether this treatment changes the mechanical properties of InGaP string resonators, remains a topic of further investigation.

CHAPTER

4 Mechanical Characterization

This chapter shall briefly describe the measurement setup used to measure the frequency responses of the InGaP resonators. The resonators are subjected to an external sinusoidal driving force and the resulting response is recorded. An overview of various characterization schemes can be found in Refs. [40], [67] and [68]. In this work a piezoelectric actuation and interferometric detection is used. All measurements are performed at room temperature.

4.1 Interferometric Setup

The schematic characterization setup is shown in Fig. 4.1. A laser beam is guided through several optical components onto the sample, which is situated in a vacuum chamber to minimize gas damping. The first half-wave plate ($\lambda/2$) and quarter-wave plate ($\lambda/4$) are used to adjust the linear polarization of the laser beam, before it passes through a polarizing beam splitter (PBS). By changing the polarization one can also adjust the laser power that impinges on the sample. The second quarter-wave plate changes the linear polarization to circular polarization. A microscope objective is used to focus the laser beam onto the string resonators. Since the laser spot is bigger than the resonator's width, the light gets reflected from the resonator as well as the substrate surface. The optical path lengths of both reflections are different, which leads to interferences. When the resonator oscillates it periodically changes the optical path length, and therefore modulates the intensity of the reflected light. So the resonator and substrate surface effectively form a Fabry-Pérot cavity. Also the laser light gets a phase shift of π by the reflection in respect to the incident light. With this phase shift and an additional pass through the quarter-wave plate the reflected light has again a linear polarization before arriving at the PBS. This time the linear polarization is orthogonal to the incident light. So the light is now reflected in the PBS and guided to a photodiode (PD) to measure the modulation of the light.

To image the sample, two 92:8 beam splitters are inserted in the optical path. One directs light of a LED onto the sample for illumination. The second one directs the

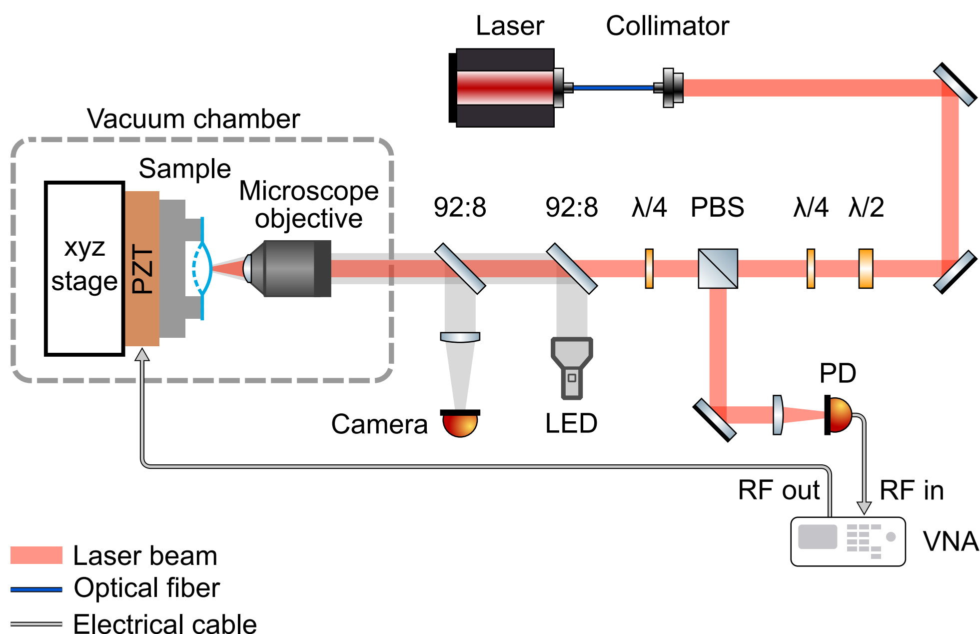

Figure 4.1: Schematic of the mechanical characterization setup. PBS: polarizing beam splitter, PD: photodiode, PZT: piezoelectric transducer, VNA: vector network analyzer

reflected LED light to a camera for imaging. This facilitates the positioning of the string resonator under the laser spot.

Inside the vacuum chamber the sample is positioned via a xyz nano-positioner stage.

The RF output of a vector network analyzer (VNA) is connected to a piezoelectric transducer (PZT), on which the sample is glued on with conductive silver paint, to actuate the string resonators. The detected signal from the photodiode is fed back into the VNA. The VNA measures the electrical power level between its output to the PZT and the input from the photodiode.

This power level is converted to an electrical voltage which is proportional to the deflection of the string resonator. This corresponds to the amplitude in the frequency response curve. The measured voltage could also be converted to the actual mechanical amplitude. However, this requires a calibration of the setup by measuring the thermal induced amplitude of a resonator to determine the measurement sensitivity. Figure 4.2 shows a typical Lorentzian frequency response curve of an InGaP string resonator. By fitting Eq. (2.5) to the data, one obtains the resonance frequency and the quality factor. All resonance frequencies and Q factors in this thesis were determined in this way. Those values are then used to extract further mechanical properties of InGaP nanomechanical resonators, as we will see in the following chapters.

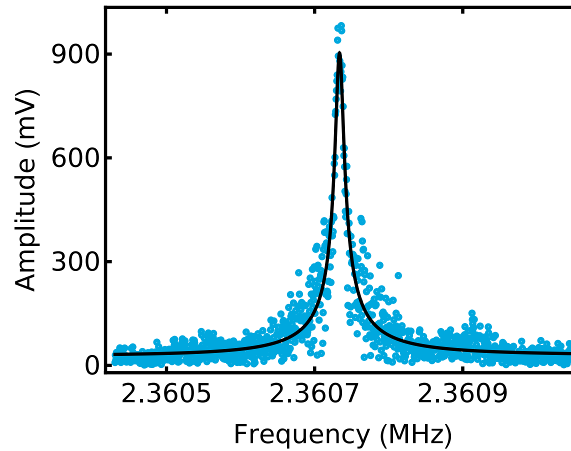

Figure 4.2: A typical frequency response (blue) of an InGaP string resonator, which has a Lorentzian shape. Depicted here is the fundamental out-of-plane mode of a $80\,\mu\mathrm{m}$ long string made of wafer 3HS. By fitting Eq. (2.5) to the data (black line), we extract a resonance frequency of $f_1 = 2.360\,73\,\mathrm{MHz}$, a line width of $\Gamma = 12.87(28)\,\mathrm{Hz}$, and a quality factor of $Q = 198\,937(4773)$ for this mode. The measurement was performed with a $1550\,\mathrm{nm}$ laser.

4.2 Choice of Wavelength

The following section is based on parts of the Master's thesis:

[62] V. C. Hauber. Herstellung von nanomechanischen Balkenresonatoren hoher Güte aus InGaP und Untersuchung der richtungsabhängigen Zugspannung des Krsitallinen Materials. Master's thesis, University of Konstanz, 2016.

The frequency measurements were performed by Valentin C. Hauber during his Master Thesis under my supervision.

In the beginning of my thesis project a red laser ($\lambda = 635\,\mathrm{nm}$) was used to detect the motion. Although InGaP has a high absorption at $\lambda = 635\,\mathrm{nm}$ [45], only interferometric setups at this wavelength were available in our group at that time. All the measurements in Chapter 5 were done with such a red laser. However, this wavelength is unfavorable to investigate InGaP string resonators. Changing the laser power leads to strong shifts of the resonance frequency. Figure 4.3 (a) shows the laser power dependent resonance frequency of a $45\,\mu\mathrm{m}$ long resonator. The incident power was measured after the objective right before it hits the resonators. Since the laser spot is bigger than the resonator width, only parts of the laser light impinges on the resonator.

The frequency shift is in the range of a few $100\,\mathrm{kHz}$ when changing the incident laser power by a few $10\,\mu\mathrm{W}$. Also the resonance frequency depends on the overlap between the laser spot and the string resonator, as can be seen in Fig. 4.3 (b).

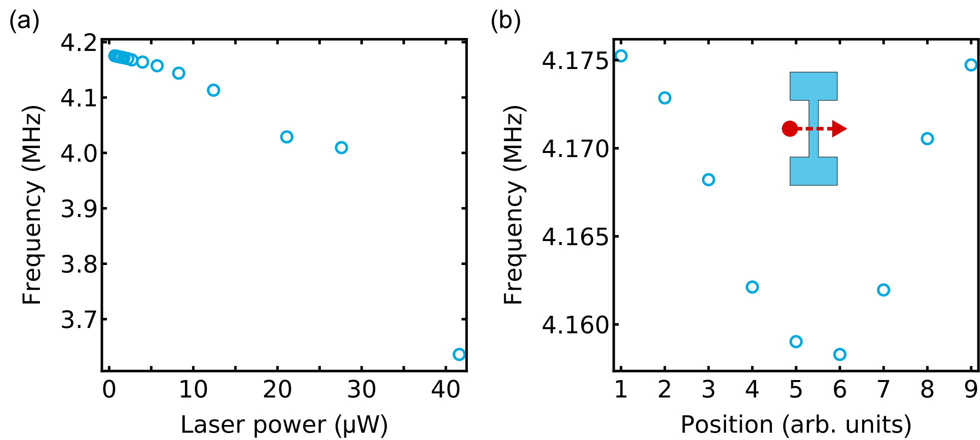

Figure 4.3: Frequency shifts due to laser heating at a wavelength of $\lambda = 635\,\mathrm{nm}$. The measurement was performed on a $45\,\mu\mathrm{m}$ long and $600\,\mathrm{nm}$ wide resonator made from wafer 1HS. (a) Resonance frequency in dependence of incident laser power. (b) Frequency in dependence of laser position, as indicated in the inset, while the laser power is kept constant.

When changing the laser spot position, the amount of laser light illuminating the the resonator is changed. Optical absorption leads to the observed frequency shifts of up to $15\,\mathrm{kHz}$. Even for this resonator with a relative low quality factor of $Q = 15\,000$, this shift is about 8 times higher than the corresponding line width of about $\Gamma \approx 1.75\,\mathrm{kHz}$.

High laser powers are observed to not only shift the resonance frequency but even destroy InGaP string resonators, as is shown in Fig. 4.4. When the incident laser power is too high, the string breaks at the position of the laser spot. The remaining parts of the resonator collapse and stick to the substrate. The gap between both resonator parts originates from the stress relaxation of the string after the fracture.

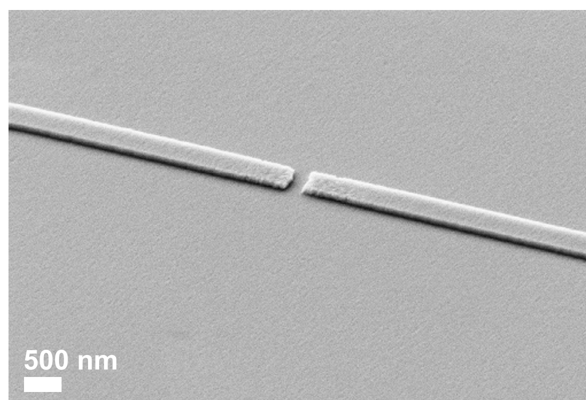

Figure 4.4: InGaP string resonator destroyed due to high laser irradiation. The resonator broke at the position of the laser spot. Because of this stress release the resonator collapsed and stuck to the substrate.

This unwanted behavior can be explained by the energy of the laser photons. A wavelength of $635\,\mathrm{nm}$ corresponds to a photon energy of $1.95\,\mathrm{eV}$. This energy is slightly above the bandgap of $1.91\,\mathrm{eV}$ for the shown InGaP sample with a Ga content of $x_{1\mathrm{HS}} = 58.7\,\%$ [45]. When the photon energy exceeds the bandgap, excitons can be created by absorbing the photons. This can explain the high optical absorption in InGaP, which translates to a heating of the resonator. The heating leads to the observed frequency shifts.

Because of the aforementioned reasons we decided to switch to another laser wavelength for further measurements. The choice fell on C band telecom lasers with wavelengths of 1530–$1565\,\mathrm{nm}$. These wavelengths correspond to photon energies of 0.79–$0.81\,\mathrm{eV}$, which is way below the bandgap of InGaP. An interferometric mechanical characterization setup with a wavelength of $1550\,\mathrm{nm}$ was build up, as is shown schematically in Fig. 4.1. This new setup dramatically reduced the optical absorption. Thus the frequency shifts are on the order of a few $100\,\mathrm{Hz}$ when changing the laser power. It minimizes the uncertainty in the frequency measurement and enables the use of higher laser powers to increase the detection efficiency.

CHAPTER

5 Orientation Dependent Stress

The following chapter is based on the publication:

[47] M. Bückle, V. C. Hauber, G. D. Cole, C. Gärtner, U. Zeimer, J. Grenzer, and E. M. Weig. Stress control of tensile-strained $In_{1-x}Ga_xP$ nanomechanical string resonators. *Applied Physics Letters*, 113(20):201903, 2018.

Fabrication and characterization of the high-stress samples was done by Valentin C. Hauber during his Master Thesis under my supervision. I performed the fabrication and characterization of the low-stress samples. The HRXRD measurements were performed and evaluated by Jörg Grenzer and the CL measurements by Ute Zeimer. Data evaluation of the nanomechanical measurements and writing of the manuscript was done by me.
Text and figures are reproduced from [47], with the permission of AIP Publishing.

This chapter focuses on the orientation dependent stress in InGaP string resonators.

To investigate this property we used the two MBE grown wafers 1HS and 2LS, illustrated in Fig. 5.1 (a) and (b). The detailed structure for both wafers is given in Appendix A. Note that only the top InGaP and AlGaAs layers were employed as resonator and sacrificial layer, respectively, in this work.

Figure 5.2 presents the measured eigenfrequencies of the fundamental modes for several sets of resonators fabricated from the high-stress InGaP epitaxial structure as a function of the resonator length L for two different resonator orientations on the chip. Resonators with an angle of $0°$ are oriented parallel to the cleaved chip edges, see inset of Fig. 5.2, which correspond to the $\langle 110 \rangle$ crystal directions for III-V heterostructures on (001) GaAs substrate wafers. Hence, the strings point along a $\langle 110 \rangle$ direction. For comparison, we also discuss resonators which are rotated clockwise by $45°$, and hence are oriented along a $\langle 100 \rangle$ direction of the crystal.

The resonance frequencies shown in Fig. 5.2 are fitted with Eq. (2.3), $f_1 = 1/(2L)\sqrt{\sigma/\rho}$. They both follow the expected $1/L$ dependence of highly

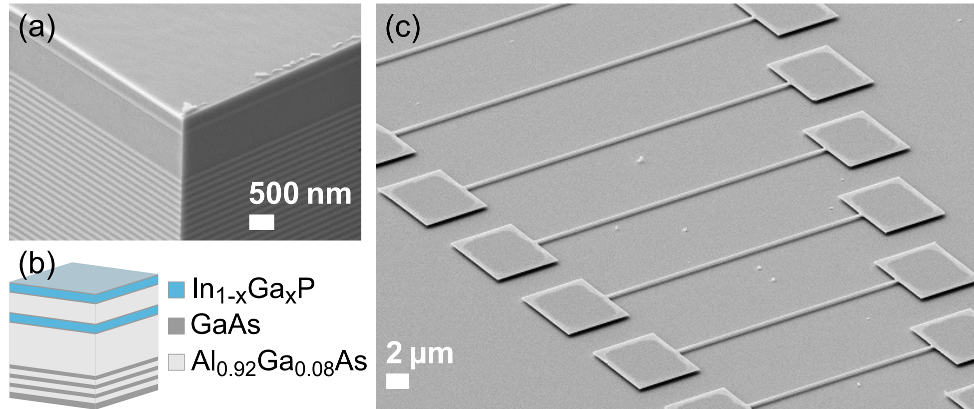

Figure 5.1: Epitaxial heterostructure. Scanning electron micrograph (a) and schematic (b) of the employed heterostructure. Only the top InGaP and AlGaAs layers are used as resonator and sacrificial layer, respectively. (c) String resonators with a thickness of $86\,\mathrm{nm}$ and lengths ranging from $9\,\mathrm{\mu m}$ to $53\,\mathrm{\mu m}$. Micrographs in (a) and (c) show high-stress InGaP of wafer 1HS. Reproduced from [47], with the permission of AIP Publishing.

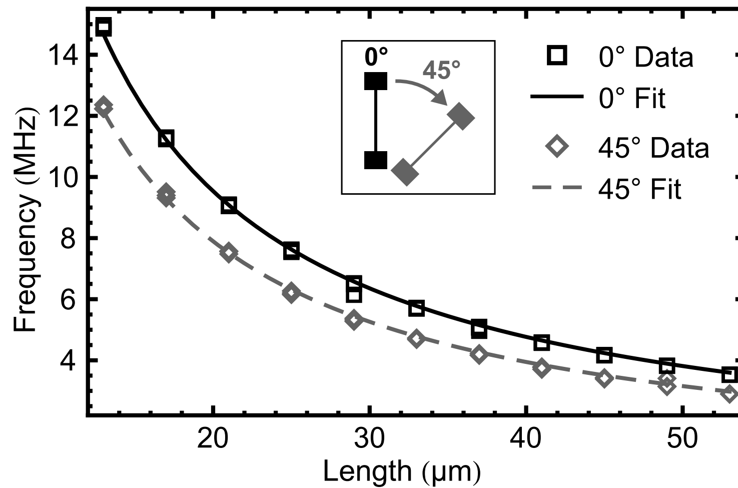

Figure 5.2: Orientation dependent resonance frequencies. Mechanical frequencies of stressed $\mathrm{In}_{1-x}\mathrm{Ga}_x\mathrm{P}$, $x_{1\mathrm{HS}} = 58.7\,\%$, string resonators as a function of their length, for two different orientations on the chip. Resonance frequencies for $0°$-resonators are plotted in black rectangles and resonators rotated clockwise by $45°$ in gray diamonds. Fits of both datasets show the $1/L$ frequency-dependence expected for the case of strongly prestressed string resonators. Calculating the weighted mean yields stress values of $\sigma(x_{1\mathrm{HS}}, 0°) = 642.3(33)\,\mathrm{MPa}$ and $\sigma(x_{1\mathrm{HS}}, 45°) = 440.2(26)\,\mathrm{MPa}$. Inset: Resonator orientations with respect to chip edges. Reproduced from [47], with the permission of AIP Publishing.

stressed string resonators. Because the resonators are fabricated from the same material, they all have the same density. Therefore, a change in frequency for a given reso-

nator length can only originate from a different tensile stress σ. The frequency mismatch between the 0° and 45° data indicates that the stress depends on the resonator's orientation. Solving Eq. (2.2) for σ and calculating the weighted mean from all data points yields $\sigma(x_{1\mathrm{HS}}, 0°) = 642.3(33)\,\mathrm{MPa}$ and $\sigma(x_{1\mathrm{HS}}, 45°) = 440.2(26)\,\mathrm{MPa}$, indicating that the tensile stress varies by almost $50\,\%$ with crystal direction.

As was already shown in Ch. 2.2.4, one can calculate the angle dependent Young's modulus $E(x, \theta)$ of an ideal and defect free system. Figure 5.3 shows $E(x, \theta)$ for the two different Ga contents $x_{1\mathrm{HS}} = 58.7\,\%$ and $x_{2\mathrm{LS}} = 52.8\,\%$. The Young's modulus varies between $80\,\mathrm{GPa}$ and $125\,\mathrm{GPa}$, between the $\langle 100 \rangle$ and $\langle 110 \rangle$ crystal directions, respectively. Additionally, we can directly calculate the strain of the InGaP layers by using Eq. (2.11a). The resulting strain values are $\varepsilon^{\|}(x_{1\mathrm{HS}}) = 5.24 \times 10^{-3}$ and $\varepsilon^{\|}(x_{2\mathrm{LS}}) = 0.95 \times 10^{-3}$, for InGaP on GaAs, respectively. To calculate the tensile stress we multiply the Young's modulus by the strain according to Hooke's law:

$$\sigma(x, \theta) = E(x, \theta)\varepsilon^{\|}(x). \tag{5.1}$$

The resulting stress values for both angles, $\sigma(x_{1\mathrm{HS}}, 0°) = 655.3\,\mathrm{MPa}$ and $\sigma(x_{1\mathrm{HS}}, 45°) = 454.9\,\mathrm{MPa}$, coincide well with the experimental results.

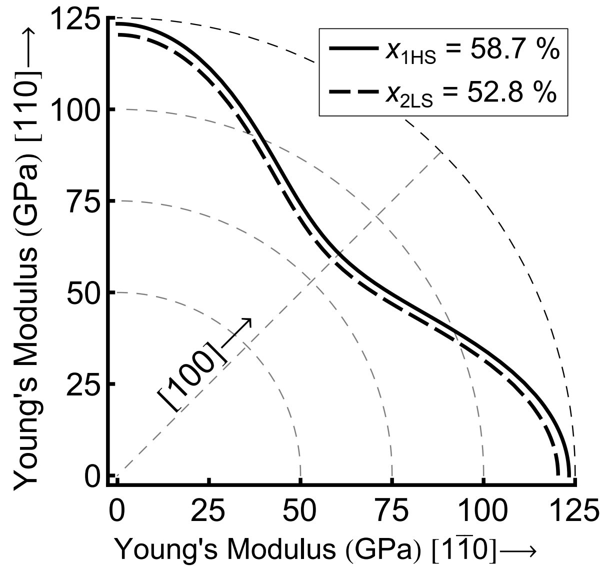

Figure 5.3: Angle dependent Young's modulus in $\mathrm{In}_{1-x}\mathrm{Ga}_x\mathrm{P}$, showing the first quadrant of the polar plot in Fig. 2.6 (b). Solid line for $x_{1\mathrm{HS}} = 58.7\,\%$ and dashed line for $x_{2\mathrm{LS}} = 52.8\,\%$. Reproduced from [47], with the permission of AIP Publishing.

To investigate the angular stress dependence of InGaP in more detail, we fabricated similar sets of resonators with angles changing in $\Delta\theta = 11.25°$ steps. For each orientation the tensile stress is extracted using Eq. (2.2). Figure 5.4 shows the resulting angular stress dependence for the two different Ga contents. In both cases, local stress maxima are observed at 0° and 90°, i. e. along $\langle 110 \rangle$ crystal directions.

Accordingly, the minima are found at $45°$ and $135°$, which correspond to $\langle 100 \rangle$ directions. The gray dashed line in Fig. 5.4 depicts the stress values obtained by using Eqs. (2.11a) and (5.1), which does not completely coincide with the experimental data. While the model conforms with the data at $0°$ and $180°$, there are deviations around $90°$ for both $x_{1\mathrm{HS}} = 58.7\,\%$ and $x_{2\mathrm{LS}} = 52.8\,\%$.

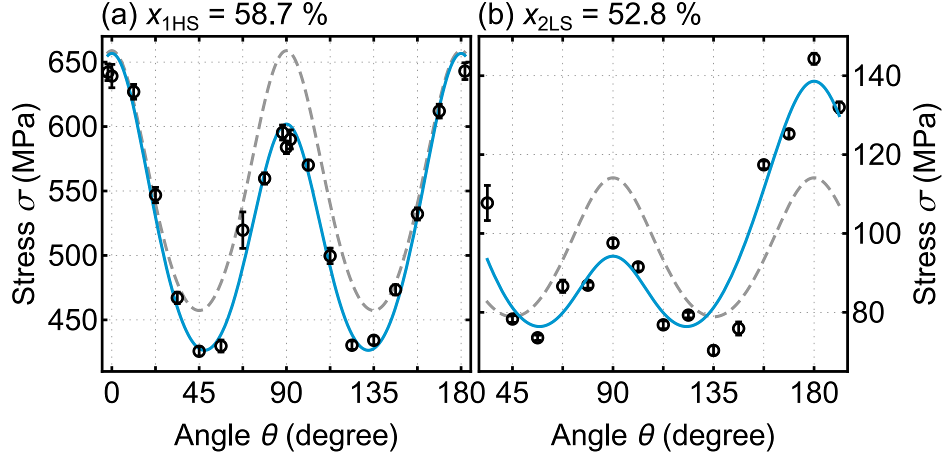

Figure 5.4: Angular stress dependence of tensile-strained $\mathrm{In}_{1-x}\mathrm{Ga}_x\mathrm{P}$ string resonators. (a) High-stress InGaP with Ga content of $x_{1\mathrm{HS}} = 58.7\,\%$. Stress varying between $430\,\mathrm{MPa}$ and $640\,\mathrm{MPa}$. (b) Low-stress InGaP with $x_{2\mathrm{LS}} = 52.8\,\%$. The stress varies between $70\,\mathrm{MPa}$ and $145\,\mathrm{MPa}$. Dashed gray line: Theoretically calculated stress, using Eqs. (2.11a) and (5.1). Blue line: Taking a change of elastic properties due to defects into account by a $\cos(2\theta)$ angle dependent change ΔE of the Young's modulus $E(x, \theta)$, see Eqs. (5.3) and Fig. 5.6. Error bars represent the uncertainty from the weighted mean calculation. Reproduced from [47], with the permission of AIP Publishing.

In collaboration with Jörg Grenzer from the Helmholtz-Zentrum Dresden-Rossendorf, we have performed high resolution x-ray diffraction (HRXRD) reciprocal space map (RSM) measurements [46] to elucidate the deviation of stress. The RSM measurements are along two orthogonal $\langle 110 \rangle$ crystal directions as shown in Fig. 5.5 (a). Further information about the HRXRD measurements and additional RSMs are given in Appendix C.

The diffraction peak arising from the InGaP layer lies directly above the substrate peak (marked by circles in Fig. 5.5 (a)), i.e. at the same $Q_{\langle 110 \rangle}$ positions, and coincides with the expectation for a $100\,\%$ pseudomorphic film within an accuracy of $10^{-3}\,\text{Å}^{-1}$. In particular the HRXRD measurements show the same out-of-plane strain for both the $[110]$ and $[\bar{1}10]$ sample orientations. However, the InGaP layer peaks show a different diffuse scattering which can be mainly attributed to point defects [69], indicating different defect densities along the orthogonal $\langle 110 \rangle$ crystal directions.

Additional cathodoluminescence (CL) measurements in Fig. 5.5 (b) are done to obtain further insight on the dislocation density in the epitaxial material. Disloca-

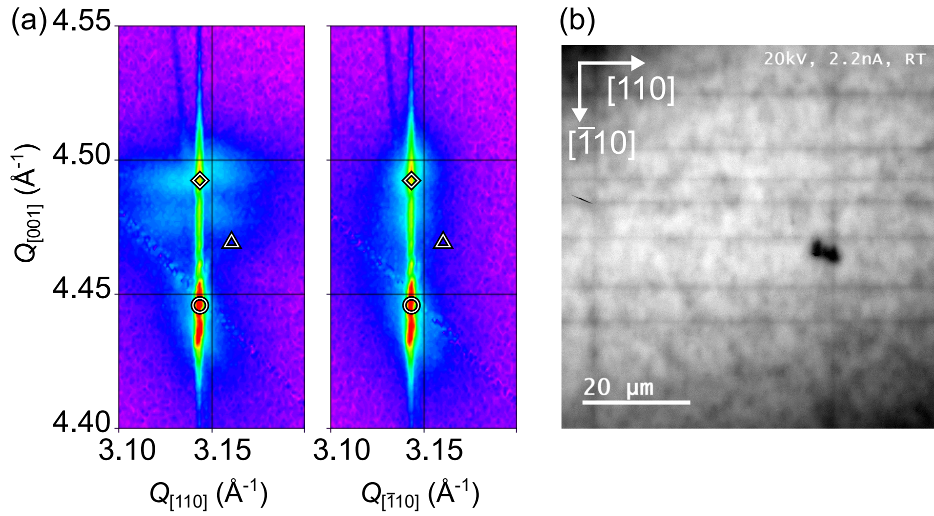

Figure 5.5: (a) Reciprocal space maps depicting the asymmetric 224 reflections of the HRXRD measurement. On the left the impinging x-ray beam is oriented along the $[110]$ and on the right along the $[\bar{1}10]$ direction. $Q_{[hkl]}$ are the reciprocal lattice vectors. The circle indicates the substrate peak. The layer peak position for a $100\,\%$ pseudomorphic InGaP layer is indicated by a diamond. In contrast, the triangle indicates the position of a fully relaxed layer. The coincidence of the observed layer peak with the diamond confirms that the unstructured InGaP is $100\,\%$ pseudomorphic. (b) Cathodoluminescence measurements are used to elucidate the dislocation density in the strained epitaxial structure. As shown in this image, the orthogonal $\langle 110 \rangle$ crystal directions exhibit a different density of dislocation lines (horizontal and vertical dark lines), resulting in variations of the defect structure as a function of orientation. Reproduced from [47], with the permission of AIP Publishing.

tion lines have a higher density along the $[\bar{1}10]$ direction than along $[110]$. These measurements confirm different defect densities along the orthogonal $\langle 110 \rangle$ crystal directions.

It has been shown, that defects can influence the elastic properties of crystalline materials, and can lead to a softening as well as a hardening of the elastic constants [70, 71].

This change of elastic properties can be treated as an effective Young's modulus

$$E_{\text{eff}}(x,\theta) = \frac{\sigma(x,\theta)}{\varepsilon^{\parallel}(x)} = E(x,\theta) + \Delta E(\theta). \tag{5.2}$$

We extract the deviation $\Delta E(\theta)$ from the experimentally obtained stress, the strain using Eq. (2.11a), and the theoretically calculated Young's modulus determined in Fig. 5.3. The extracted values are shown in Fig. 5.6 and clearly reveal an angular deviation from the theoretical Young's modulus. Both the softening and hardening of elastic constants can be seen for our two different InGaP compositions. One can see softening for the high-stress sample, while the low-stress sample shows both

softening and hardening. Fitting a phenomenological $\cos(2\theta)$ function to the data, leads to the deviation functions

$$\Delta E_{1\mathrm{HS}}(\theta) = (-5.53 + 5.13\cos(2\theta))\ \mathrm{GPa}, \tag{5.3a}$$
$$\Delta E_{2\mathrm{LS}}(\theta) = (2.44 + 23.40\cos(2\theta))\ \mathrm{GPa} \tag{5.3b}$$

for the high-stress and low-stress InGaP respectively. Adding those functions to the theoretical Young's modulus to calculate the angular stress (Eq. (5.1)), we obtain the solid blue lines in Fig. 5.4 which indicate the added effect.

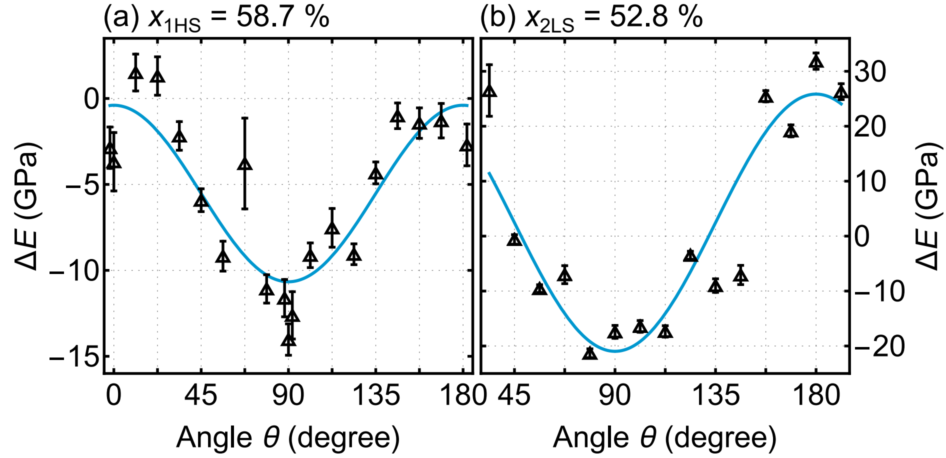

Figure 5.6: Angle dependent change ΔE of the Young's modulus of tensile-strained $\mathrm{In}_{1-x}\mathrm{Ga}_x\mathrm{P}$ string resonators. (a) High-stress InGaP with Ga content of $x_{1\mathrm{HS}} = 58.7\,\%$. A softening of elastic constants due to defects is visible by the negative change of Young's modulus. A $\cos(2\theta)$ function (blue line) is fit to the data to get the angle dependent change ΔE of the Young's modulus $E(x, \theta)$. (b) Low-stress InGaP with $x_{2\mathrm{LS}} = 52.8\,\%$. Both softening and hardening is visible for the low-stress sample. Error bars represent the uncertainty from the weighted mean calculation. Reproduced from [47], with the permission of AIP Publishing.

For the given composition we extracted an angle-dependent tensile stress of up to $650\,\mathrm{MPa}$. InGaP with a Ga content of $x_{2\mathrm{LS}} = 52.8\,\%$ shows lower tensile stress around $100\,\mathrm{MPa}$ with a similar angle-dependence as the high-stress InGaP.

The anisotropic Young's modulus is expected from the crystal structure as it was already theoretically calculated in Ch. 2.2.4. However, the orientation dependent defect densities add a significant effect to the resulting tensile stress. This illustrates to have a closer look on the microscopic material properties, since the reality can not always be fully captured by simple models.

CHAPTER

6 Length Dependent Stress

The following chapter is based on the unpublished manuscript:

[72] M. Bückle, Y. S. Klaß, F. Nägele, R. Braive, and E. M. Weig. Universal dependence of tensile stress on the length of nanomechanical string resonators. In preparation, 2020.

Yannick S. Klaß did the fabrication of the SiN sample, while the fabrication of the InGaP samples was done by me. I performed the measurements and data evaluation of the presented InGaP and SiN samples. The theoretical model was a joint work by Yannick S. Klaß and me, as well as the writing of the manuscript.

In the previous chapter we had a look on the stress distribution that arises from the crystal structure of the samples. In this chapter we take a closer look on the tensile stress as a function of the resonator length.

Two III-V heterostructures hosting a $81\,\mathrm{nm}$ thick $In_{0.408}Ga_{0.592}P$ film (wafer 3HS) and a $100\,\mathrm{nm}$ thick $In_{0.415}Ga_{0.585}P$ film (wafer 4HS), have been epitaxially grown atop sacrificial layers of $Al_{0.555}Ga_{0.445}As$ and $Al_{0.85}Ga_{0.15}As$, respectively, on a GaAs wafer. Wafer 4HS was kindly provided by our collaborator Rémy Braive. See Appendix A for full details of the wafers.

The lower Al contents of the sacrificial layers made it possible to further improve the fabrication steps, because of better control over the etch rate and without detrimental hydrolysis (cf. Ch. 3.5). The detection sensitivity is increased by the implementation of a new interferometric characterization setup at a telecom wavelength as addressed in Ch. 4.2. Both improvements made it possible to measure several higher harmonics of the resonators. This makes the determination of mechanical material properties more accurate.

A series of nanomechanical string resonators with varying length, ranging from $10\,\mathrm{\mu m}$ to $110\,\mathrm{\mu m}$ in steps of $10\,\mathrm{\mu m}$, cf. Fig. 3.2 (b), are defined on both wafers. All resonators in this chapter have a $0°$ orientation. Figure 6.1 (a) shows such a series of

resonators fabricated from wafer 3HS. A schematic sketch of such string resonators with the definition of the used parameters are shown in Fig. 6.1 (b) + (c).

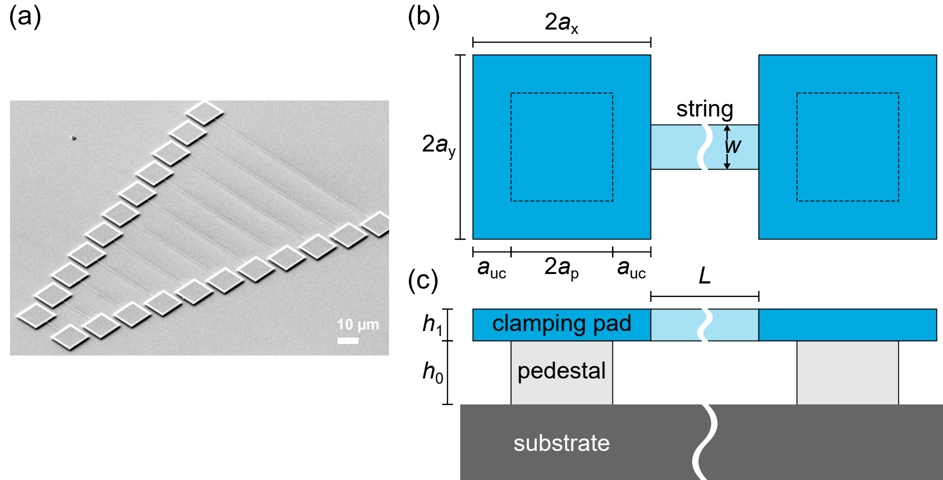

Figure 6.1: (a) SEM image of a series of string resonators with lengths increasing from $10\,\mu\mathrm{m}$ to $110\,\mu\mathrm{m}$ in steps of $10\,\mu\mathrm{m}$, fabricated from wafer 3HS. Schematic design of string resonators, (b) in top view and (c) in side view. The device layer (dark and light blue) has a thickness h_1 and the pedestal (light gray) has a height of h_0. The clamping pads (dark blue) have a size of $2a_x \cdot 2a_y$. Due to undercutting during the wet etch, the size of the pedestal is reduced by the undercut a_{uc} from all sides, leading to a pedestal length along the string direction of $2a_{\mathrm{p}} = 2a_x - 2a_{\mathrm{uc}}$. The pedestal size is indicated by dashed lines in (b). The string (light blue) has a length L and a width w.

For each resonator length we probe the fundamental out-of-plane mode as well as a series of higher harmonics, and determine the corresponding eigenfrequencies as previously described in Ch. 4. The resonance frequencies shown in Fig. 6.2 are fitted with Eq. (2.2). Unless stated otherwise, error bars that are smaller than the plot markers are omitted for clarity. To a very good approximation, the eigenfrequencies of all resonators scale nearly linearly with the mode number as expected for stress dominated string resonators, see Eq. (2.3).

The fit of the eigenfrequency as a function of mode number allows us to extract the tensile stress of each string resonator. The obtained values are shown as a function of the resonator length for both InGaP wafers in Fig. 6.3. It is clear that the tensile stress is not constant, but decreases for increasing length of the resonator. For the 3HS material the stress decreases from about $775\,\mathrm{MPa}$ for a length of $20\,\mu\mathrm{m}$ down to roughly $635\,\mathrm{MPa}$ for $110\,\mu\mathrm{m}$ and for wafer 4HS from $700\,\mathrm{MPa}$ to $565\,\mathrm{MPa}$. This is a change in tensile stress of about $22\,\%$ for both wafers.

To check if such a behavior generally applies to string resonators or if it is unique to InGaP, I also measured the tensile stress values of silicon nitride (SiN) resonators. The sample was fabricated by my colleague Yannick S. Klaß. It features a $100\,\mathrm{nm}$ thick layer of high-stress SiN on a fused silica wafer. The extracted stress values are

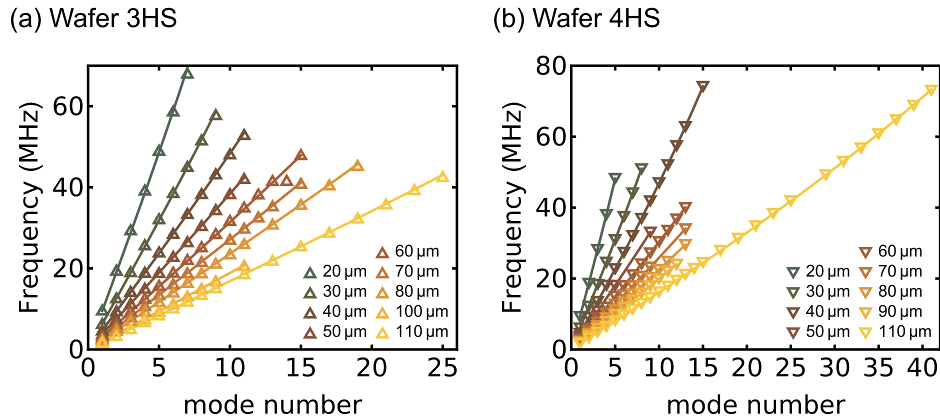

Figure 6.2: Eigenfrequencies of the out-of-plane modes as a function of the mode number for InGaP string resonators. Measurements are shown for samples fabricated (a) from wafer 3HS and (b) from 4HS. Equation (2.2) (solid lines) is fitted to the eigenfrequencies to extract the tensile stress.

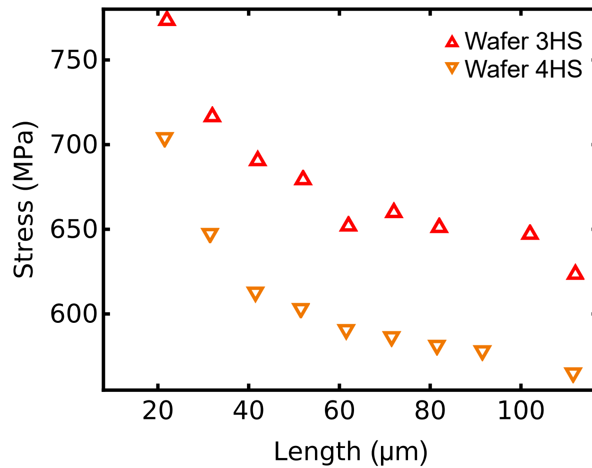

Figure 6.3: Tensile stress of InGaP string resonators vs. resonator length, fabricated from the wafers 3HS (red up-triangle) and 4HS (orange down-triangle). The stress is determined by fitting Eq. (2.2) to the eigenfrequencies, see Fig. 6.2.

shown in Fig. 6.4. They show the same qualitative behavior as the InGaP resonators. Additionally my colleague Yannick S. Klaß can see the same behavior for his silicon carbide string resonators. This indicates a general stress dependence on the resonator length. It is an effect, which has, to the best of our knowledge, not been observed or described in literature.

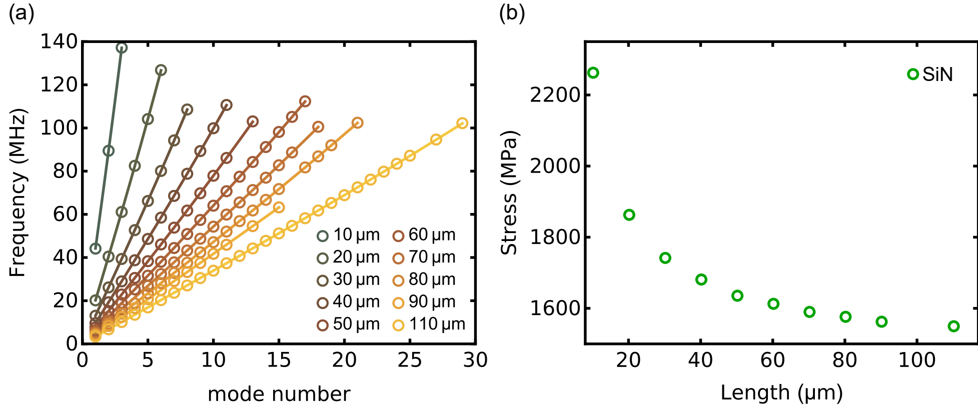

Figure 6.4: Eigenfrequencies and tensile stress of SiN string resonators. (a) Frequencies of the out-of-plane modes as a function of the mode number for SiN string resonators. Equation (2.2) (solid lines) is fitted to the eigenfrequencies to extract the tensile stress as a function resonator length (b).

6.1 Finite Element Method Simulations

To further support this hypothesis I performed finite element method (FEM) simulations with *COMSOL Multiphysics*. For simplicity I simulated $100\,\mathrm{nm}$ thick SiN resonators on a SiO_2 substrate, since SiN is a known and common material in NEMS and has no orientation dependent stress. As an initial film stress in the SiN layer I chose $2.9\,\mathrm{GPa}$ to match the qualitative stress dependence, see Fig. 6.4.

Figure 6.5 shows the simulated stress over resonator length for different pedestal heights h_0. The FEM simulations show a length dependent tensile stress. Even without an undercut, $a_{\mathrm{uc}} = 0\,\mathrm{\mu m}$, we can see a length dependence. The pedestal height seems to have only a minor influence on the stress, and only seems to play a role for very short strings.

Figure 6.6 shows simulated tensile stress for different undercuts while having a fixed pedestal height. An increased undercut leads to an increased overall stress for all resonator lengths. This increase is even more pronounced for shorter resonators. For a length of $10\,\mathrm{\mu m}$ and an undercut of $5\,\mathrm{\mu m}$ the stress in the resonator even surpasses the initial film stress of $2.9\,\mathrm{GPa}$

The simulated stress distribution of a resonator structure is shown in Fig. 6.7. We see that the highest stress is located in the thin string. We also see a slight deformation of the pedestals and clamping pads. The contraction of the clamping pads can be best seen in Fig. 6.7 (b).

Such a contraction leads to an elongation of the string ΔL, which directly translates into an additional strain

$$\Delta\varepsilon = \frac{\Delta L}{L}. \tag{6.1}$$

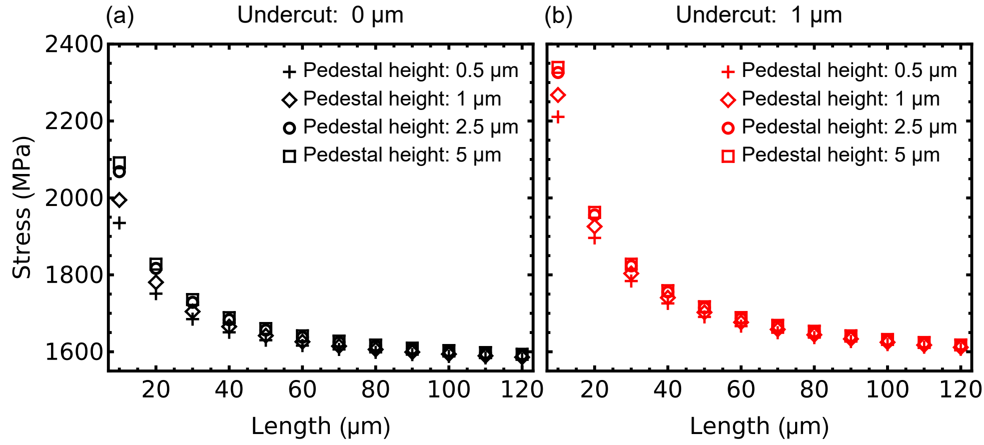

Figure 6.5: Stress values from FEM simulations for different pedestal heights. The stress is extracted in the middle of the string. Simulations with an undercut of (a) $a_{\mathrm{uc}} = 0\,\mathrm{\mu m}$ and (b) $a_{\mathrm{uc}} = 1\,\mathrm{\mu m}$. Even without an undercut we can see a length dependence of the stress. In both cases the stress levels off at about $1600\,\mathrm{MPa}$ for long resonators. Different pedestal heights only have a minor influence on strings longer than $30\,\mathrm{\mu m}$.

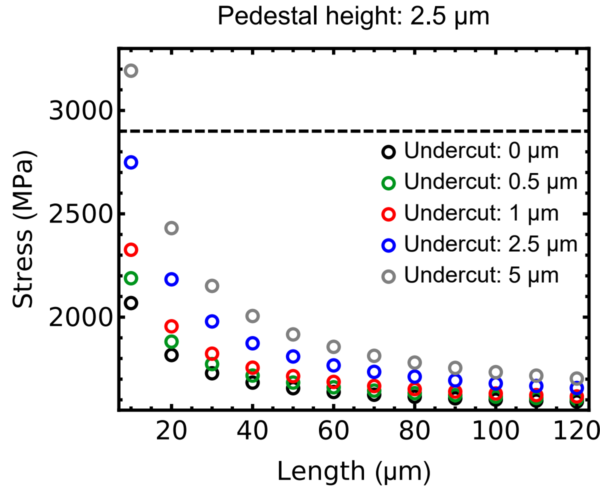

Figure 6.6: Stress values extracted from FEM simulations for different undercuts. The stress is extracted in the middle of the string. The pedestal height is set to $h_0 = 2.5\,\mathrm{\mu m}$ and the undercut is changed between 0–$5\,\mathrm{\mu m}$. An increased undercut increases the overall tensile stress. For a length of $10\,\mathrm{\mu m}$ and an undercut of $5\,\mathrm{\mu m}$ the stress in the resonator even surpasses the initial film stress (dashed horizontal line) of $2.9\,\mathrm{GPa}$.

Together with the Young's modulus we get a change of the tensile stress

$$\Delta\sigma = E\Delta\varepsilon = E\frac{\Delta L}{L}, \tag{6.2}$$

where we can already see a $1/L$ length dependence.

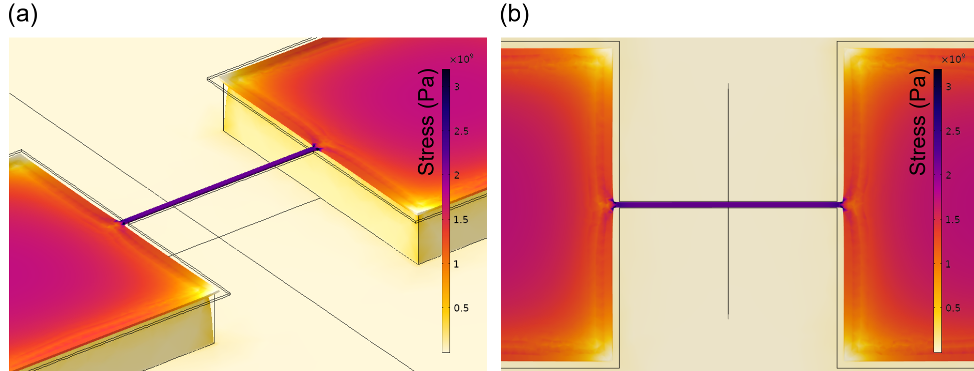

Figure 6.7: FEM simulation of the stress distribution and the resulting deformation. (a) Angled view on a $10\,\mu\mathrm{m}$ long resonator on $2.5\,\mu\mathrm{m}$ high pedestals and an undercut of $0.5\,\mu\mathrm{m}$. (b) Top view of the same structure as in (a). The highest stress is located in the thin string. The clamping pads are contracting and pulling on the string.

6.2 Theoretical Stress Model

To quantify this phenomenon, Yannick S. Klaß and I have developed a simple theoretical model. Our model is based on elastic theory. As such, it is material independent and can be applied to any material system. Our model assumes a prismatic string as illustrated in Fig. 6.1, of length L, width w and thickness h_1. Its cross sectional area is $A_\mathrm{s} = w \cdot h_1$. On both ends, the string is attached to a rectangular clamping structure. These consist of a clamping pad in the device layer with dimensions $2a_x$ and $2a_y$, as well as thickness h_1, which is supported by a pedestal of height h_0 in the underlying sacrificial or substrate layer.

As a result of the isotropic wet etching process required to suspend the nanostrings, the clamping pads exhibit a certain undercut a_uc, therefore the width of the pad $2a_x$ is larger than that of the pedestal $2a_\mathrm{p} = 2a_x - 2a_\mathrm{uc}$. The cross sectional area of the clamping pad along the string direction is $A_\mathrm{p} = 2a_y \cdot h_1$. The thickness of the device layer h_1 is obtained from the wafer growth protocol, whereas the height of the pedestal h_0 was determined by atomic force microscopy. The half-widths of the clamping pad a_x and a_y have been measured with a SEM. Also the undercut a_uc was estimated using a SEM. The geometric and mechanical parameters of the samples are listed in Tabs. 6.1 and 6.2. Because the Al content of the sacrificial AlGaAs layer changes the mechanical parameters only slightly, see Ch. 2.2.2, we use the parameters of plain GaAs for all InGaP samples.

As we will show in the following, the tensile stress in the device layer atop an unstressed sacrificial layer or substrate gives rise to a balance of forces which in turn leads to a length- and geometry-dependent change in the resultant tensile stress of

Table 6.1: Geometric parameters of the investigated samples.

	h_1 (nm)	h_0 (nm)	a_{uc} (nm)	$2a_x$ (μm)	$2a_y$ (μm)	w (nm)
3HS	81(1)	990(10)	1325(170)	13.5(2)	14.0(2)	160(8)
4HS	100(1)	990(10)	1325(170)	13.0(2)	13.7(2)	265(15)
SiN	100(5)	460(20)	300(100)	14.2(2)	15.0(2)	333(7)

Table 6.2: Mechanical parameters of the investigated samples.

	E_1 (GPa)	E_0 (GPa)	ν_1	ν_0	$\varepsilon^{\parallel}(x)$ (%)
3HS	123.6[a]	85.9[b]	0.32[b]	0.31[b]	0.57[c]
4HS	123.2[a]	85.9[b]	0.32[b]	0.31[b]	0.52[c]
SiN	240.0[d]	73.0[e]	0.25[e]	0.17[e]	—

[a]Calculated with Eq. (2.20). [b]Taken from Ref. [45]. [c]Calculated with Eq. (2.11a).
[d]Determined by measurements in our group. [e]Taken from Ref. [73].

the string resonator. The initial device layer is biaxially stressed with a film stress

$$\sigma_{\mathrm{film}} = \frac{E_1}{1-\nu_1}\varepsilon^{\parallel} \tag{6.3}$$

with E_1 and ν_1 as the Young's modulus for the 0° orientation and Poisson ratio of the device layer, and $\varepsilon^{\parallel}$ as the initial biaxial strain in the device layer, cf. Eq. (2.11a).

Also one has to note that, when releasing the string during wet etching, the biaxial film-stress relaxes in the direction perpendicular to the string. This leads to an uniaxial stress σ_{s} along the string. That is the reason why the stress in the string is usually below the initial film stress.

To quantify the contributing forces, we separately look at different relaxation mechanisms in our resonator structure. This division is sketched in Fig. 6.8. On the one hand, we assume shearing of the pedestal due to the stressed device layer atop. We know this from the simulations without an undercut, see Fig. 6.5 (a). The device layer will contract until the stress is compensated by the shearing force of the pedestal, Fig. 6.8 (b). On the other hand, the undercut parts of the tensile-stressed clamping pad relax and thus apply additional stress on the string, Fig. 6.8 (c). This can also be supported by the simulations as we see in Fig. 6.6. The effect is similar to the known strain engineering and clamp tapering [23, 74].

The combination of the described effects gives rise to the modified tensile stress inside the string, which we are measuring (see Eq. (2.2) and Figs. 6.3 and 6.4 (b)). The model assumes a clear separation between these two effects and that they do not

influence each other. It also neglects geometric and elastic reconfigurations of the sheared pedestal and stressed clamping pad arising from the shearing of the pedestal and from the release of the resonator, which is assumed to be small.

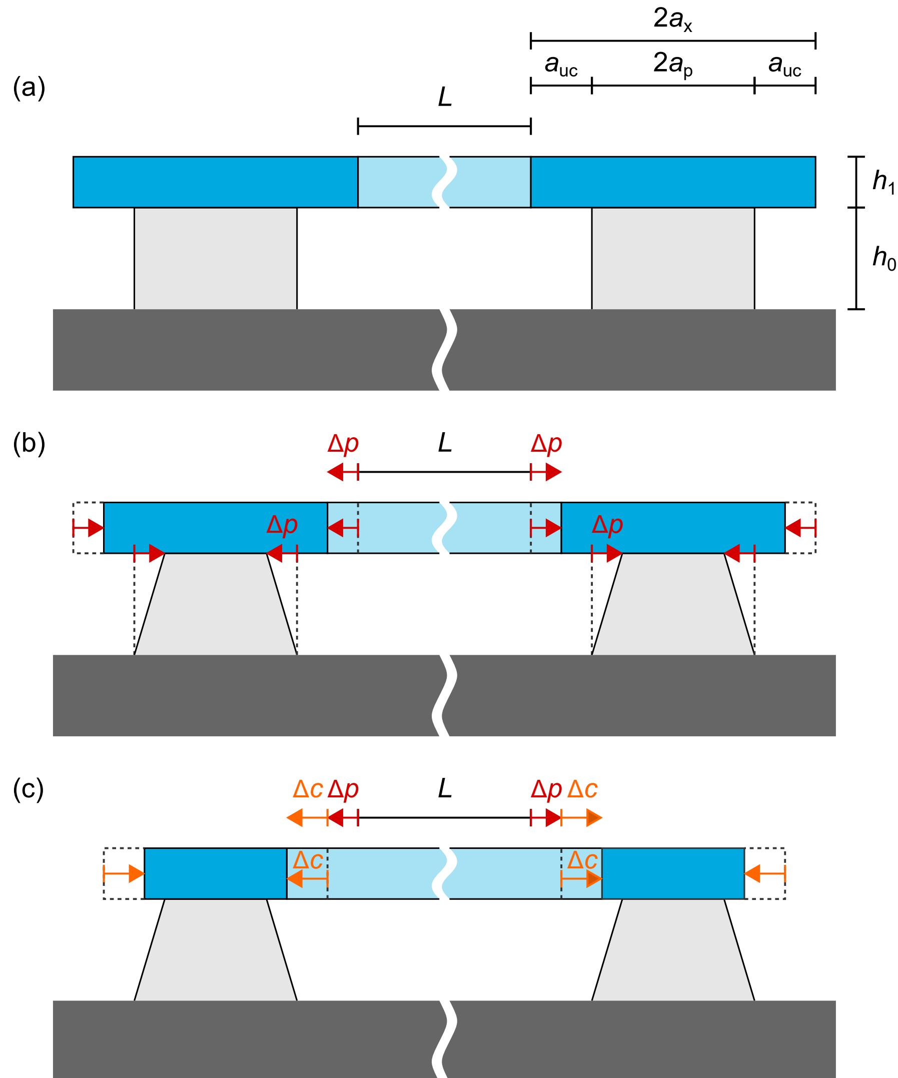

Figure 6.8: Sketch for the theoretical model of length dependent stress. (a) We start with our undeformed resonator structure as was already shown in Fig. 6.1 (b) The stress of the device layer (blue) leads to shearing of the pedestal (light gray) by an amount of Δp. (c) In addition, the undercut parts of the tensile stressed clamping pad contract by Δc, which is determined by a balance of forces between the string and undercut pad. Both effects lead to a length change of $\Delta L = 2\Delta c + 2\Delta p$, which relates to a change of strain $\Delta\varepsilon = \Delta L/L$.

To evaluate the shear of the pedestal induced by the vertical release of the structure, we will first consider an isolated clamping structure and focus on its cross sec-

tion along the x-z-direction as indicated in Fig. 6.8(b). For simplicity, we neglect any forces of the string that could act on the pedestal. The strong tensile stress in the device layer leads to a contraction of the clamping pad in order to minimize internal forces. This contraction produces an increasing shear of the pedestal. The reconfiguration of the clamping structure stops once equilibrium between the reduced tensile force and the counteracting shearing force is reached. Taylor & Yuan [75] analytically calculated the shear stress τ of such a shear-constrained material system

$$\tau = E_1 h_1 \, k \, \varepsilon^{\parallel}(x) \tanh(k a_{\mathrm{p}}) \,, \quad k = \sqrt{\frac{G_0}{h_0} \frac{1}{E_1 h_1}} \tag{6.4}$$

where h_0 and h_1 are the height of the pedestal and the clamping pad, respectively, a_{p} is half the pedestal width, $G_0 = E_0 / \left(2(1+\nu_0)\right)$ is the shear modulus of the pedestal, E_1 is Young's modulus of the device layer, and $\varepsilon^{\parallel}(x)$ is the initial biaxial strain in the device layer, cf. Eq. (2.11a). With this shear stress and using Hooke's law for materials under shear, we can express the resulting maximum contraction of the clamping pad Δp from its original half-width a_x as:

$$\Delta p = \frac{h_0}{G_0} \tau = \frac{\varepsilon^{\parallel}(x)}{k} \tanh(k a_{\mathrm{p}}) \,. \tag{6.5}$$

Now we look at the undercut parts of the clamping pads and how they interact with the string. The rim of the clamping pad is freely suspended by the amount of a_{uc}. This enables a relaxation of the tensile force in the undercut parts of the pads which gives rise to a contraction by an amount Δc, see Fig. 6.8(c). This force due to the undercut, acts on the interface between the clamping pad and the nanostring, and can be expressed as

$$F_{\mathrm{c}} = \sigma_{\mathrm{film}} A_{\mathrm{p}} - E_1 \frac{\Delta c}{a_{\mathrm{uc}}} A_{\mathrm{p}}, \tag{6.6}$$

where σ_{film} (see Eq. (6.3)) is the initial stress of the device layer, which is reduced by $E_1 \Delta c / a_{\mathrm{uc}}$ in the undercut part of the clamping pad, again according to Hooke's law. At the outside of the clamping pad, where there is no string resonator, the suspended part of the clamping pad fully relaxes such that $F_{\mathrm{c}} = 0$. At the inner face with the attached string, the contracting force of the clamping pad is counteracted by a second force acting on the interface between the clamping pad and the string which is associated with the elongation ΔL of the nanostring, cf. Eq. (6.1),

$$F_{\mathrm{s}} = \sigma_{\mathrm{s}} A_{\mathrm{s}} + E_1 \frac{\Delta L}{L} A_{\mathrm{s}}, \tag{6.7}$$

where σ_{s} is the stress of the string after the lateral release, and $E_1 \Delta L / L$ is its modification according to Hooke's law.

The equilibrium condition for the clamping pad – string interface

$$F_{\mathrm{c}} = F_{\mathrm{s}} \tag{6.8}$$

describes the final geometric reconfiguration of the clamping pad and the string, under the boundary condition that the total length,

$$2\Delta p + 2\Delta c = \Delta L \tag{6.9}$$

of the compound has to be conserved.

Equations (6.8) and (6.9) form a second order system of linear equations with the unknown parameters ΔL and Δc. Solving for the elongation of the resonator yields

$$\Delta L = L \cdot \frac{2\left(A_{\mathrm{p}} a_{\mathrm{uc}} \sigma_{\mathrm{film}} + A_{\mathrm{p}} E_1 \Delta p - A_{\mathrm{s}} a_{\mathrm{uc}} \sigma_{\mathrm{s}}\right)}{E_1\left(2 A_{\mathrm{s}} a_{\mathrm{uc}} + A_{\mathrm{p}} L\right)}. \tag{6.10}$$

This length change of the resonator directly translates into an additional strain, see Eq. (6.1), giving rise to a length dependent stress $\sigma(L)$ of the doubly clamped string resonators using Eq. (6.2)

$$\sigma(L) = \sigma_{\mathrm{s}} + E_1 \frac{\Delta L}{L}. \tag{6.11}$$

6.3 Discussion

To validate our theoretical model, we fit Eq. (6.11) to the experimental data of both InGaP wafers, using the geometric and material parameters specified in Tabs. 6.1 and 6.2, and Δp from Eq. (6.5). Only the one dimensional stress σ_{s} is employed as fit parameter for both wafers. The obtained fit parameters are summarized in Tab. 6.3 and the results for InGaP are plotted in Fig. 6.9 (a). The shaded area represents the

Table 6.3: Calculated and fitted parameters of the investigated samples.

	σ_{film} (GPa)	σ_{s} (MPa)
3HS	1.04[a]	607[b]
4HS	0.95[a]	539[b]
SiN	5.37[b]	1476[b]

[a]Calculated with Eq. (6.3). [b]From fit.

model's uncertainty arising from the error of the input parameters, see Tab. 6.1.

For SiN we need two fit parameters, σ_{s} and σ_{film}, since we do not know the initial film stress or strain of the device layer. The fit corresponding to the SiN data is shown in Fig. 6.9 (b).

As long as $A_{\mathrm{s}} \ll A_{\mathrm{p}}$ and $a_{\mathrm{uc}} \ll L$, we can approximate the length dependence of Eq. (6.11) as $\sigma(L) \propto 1/L$. This holds true for all nanostrings under investigation, such that an $1/L$ dependence of the stress can be assumed. We see a remarkable agreement between the model and the experimental data. It is particularly noteworthy

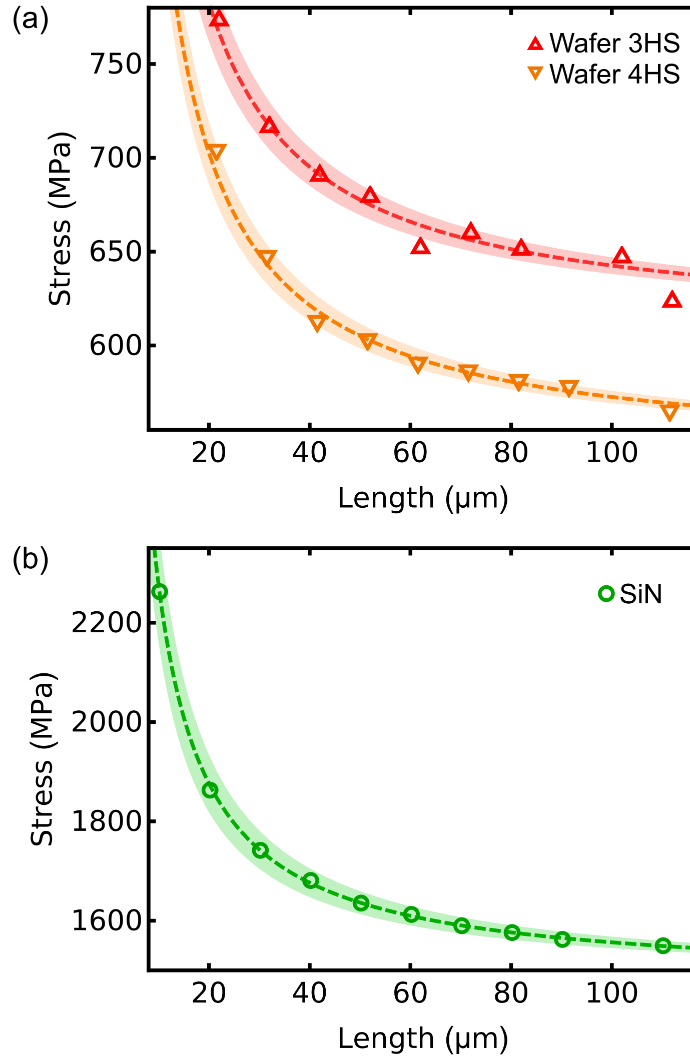

Figure 6.9: Experimentally determined tensile stress as a function of the length of the string resonators for (a) both InGaP wafers and (b) for SiN. Fits of Eq. (6.11) are included as dashed lines. The obtained fit parameters are summarized in Tab. 6.3. The shaded areas indicate the uncertainty of the fit resulting from measurement errors of the pedestal height h_0 and undercut a_{uc}.

that only one fit parameter, σ_{s}, is employed for the InGaP samples. For the approximation of small A_{s} and a_{uc} this corresponds to a vertical offset and thus the limit of very long resonators $\sigma(L \rightarrow \infty)$.

The film stresses of the 3HS and 4HS wafers are $1.04\,\mathrm{GPa}$ and $0.95\,\mathrm{GPa}$ and the extracted string stresses are $607\,\mathrm{MPa}$ and $539\,\mathrm{MPa}$. This means that initial film stress is reduced nearly by a factor of two for very long string resonators. For SiN this value is even higher, about 3.5, where the film stress of $5.31\,\mathrm{GPa}$ reduces to $1.48\,\mathrm{GPa}$. At first glance the film stress of SiN seems to be quite high, however it is

still below the yield strength of about $6.4\,\mathrm{GPa}$ [76, 77].

Using elastic theory one would expect that the biaxial film stress σ_{film} and the uniaxial stress in the string σ_{s} are related by $\sigma_{\mathrm{film}} = \sigma_{\mathrm{s}}/(1-\nu)$, cf. Eq. (6.3). However, when the uniaxial stress is calculated like in the previous chapter 5 with Eq. (5.1), it yields values of $\sigma(x_{3\mathrm{HS}}, 0°) = 706\,\mathrm{MPa}$ and $\sigma(x_{4\mathrm{HS}}, 0°) = 640\,\mathrm{MPa}$. Both values are higher than the measured ones for long strings, see Fig. 6.9 and the extracted σ_{s} in Tab. 6.3. The reason why both wafers 3HS and 4HS have lower stress values than one would expect from Eq. (5.1) is not clear. It could be that stress of the InGaP films did slightly relax. Compared to wafer 1HS in Ch. 5, which was grown using MBE, the wafers 3HS and 4HS were grown using MOCVD. This may be a reason for higher defect densities, which would influence the elastic constants. HRXRD and CL measurements of both wafers would be required to further investigate the origin of the slightly lower stress.

Nonetheless, a universal dependence of the tensile stress on the length of the resonator is evident. Even though the assumptions of the theoretical model are quite crude and simplified, e.g. we only assume shearing in the pedestal and that it is independent of the forces of the string or undercut, it shows remarkable agreement with the data. It is a simple and general description of the stress dependence in tensile stressed string resonators.

CHAPTER

7 Quality Factor Measurements

Until now we looked at the tensile stress of several InGaP wafers and how it is distributed along different orientations and for different resonator lengths. In this chapter we will closely examine the Q factors we extract from the response curves.

As in the previous chapter the samples are fabricated from two high-stress wafers 3HS and 4HS. For the wafers 1HS and 2LS it was not possible to reliably measure their quality factors because of the high Al content of the sacrificial layer and the resultant problems, cf. Ch. 3.5.

Additionally we look at resonators made from the low-stress wafer 5LS. This wafer hosts a $100\,\mathrm{nm}$ thick $In_{0.486}Ga_{0.514}P$ film epitaxially grown on top of a sacrificial $Al_{0.85}Ga_{0.15}As$ layer on a GaAs wafer. With a Ga content of only $x_{5\mathrm{LS}} = 51.4\,\%$, the InGaP layer is close to the lattice-matched case. This layer therefore has an average stress of only $42(5)\,\mathrm{MPa}$. Figure 7.1 shows the resonance frequencies and corresponding extracted stress. Unless stated otherwise, error bars that are smaller than the plot markers are omitted for clarity. The low-stress is already visible in the frequency data, where the frequency does not scale linearly with the mode number and we are no longer in the stress dominated regime, cf. Eq. (2.2).

7.1 Quality Factors and Intrinsic Q

The quality factors are extracted from the frequency response curves, see Fig. 4.2, by fitting Eq. (2.5) to the data. All the measurements are performed in the linear frequency response regime of the resonator.

Figures 7.2 and 7.3 show the quality factor vs. mode number for different resonators made from the wafers 3HS, 4HS and 5LS. The fundamental mode has the highest Q. As expected from the dissipation dilution model, the Q factors of the resonators decreases as the mode number increases. Higher harmonics of the resonator have a larger number of nodes and antinodes. Those introduce more bending in the resonator, since the smaller wavelength is accompanied with smaller bending radii. Thus there is an increase in the internal dissipation, which in turn decreases the Q.

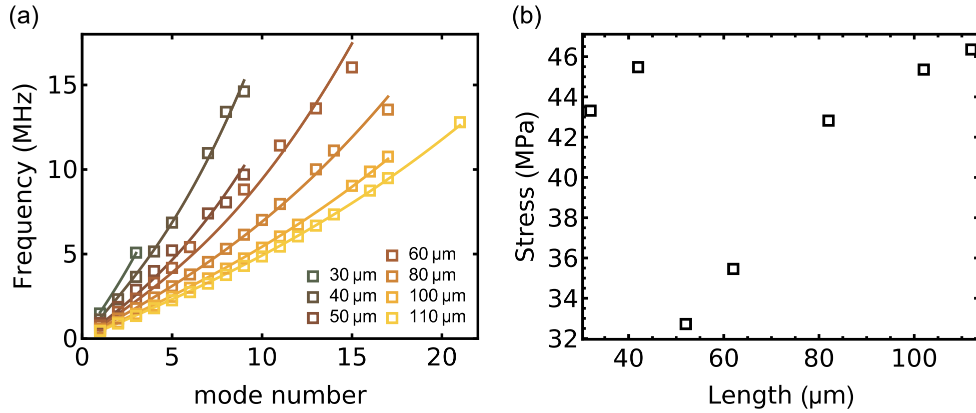

Figure 7.1: Frequencies and tensile stress of wafer 5LS. (a) The frequency vs. mode number shows a nonlinear dependence for all the resonator lengths. This indicates a low tensile stress. When fitting Eq. (2.2) (solid lines) to the data we get the tensile stress displayed in (b). The average stress over all lengths is $42\,\mathrm{MPa}$, which is one order of magnitude below that of the high-stress wafers.

For the high-stress wafers (Fig. 7.2) the Q of the fundamental mode goes up to $300\,000$ for $110\,\mathrm{\mu m}$ long strings.

The Q factors for the low-stress material (Fig. 7.3) are smaller than for the high-stress InGaP. The lower tensile stress leads to less dissipation dilution and hence lower Q factors. Nevertheless the Q factors of the low-stress resonators go as high as $75\,000$, which is remarkable for the low stress value.

By applying the dissipation dilution model we can fit Eq. (2.9) to the data, which is represented by the solid lines in Figs. 7.2 and 7.3. With this we can extract the intrinsic Q, which is an indication of the intrinsic defects or internal dissipation of a material. This enables a comparison between different material systems and materials with different tensile stress values.

The extracted values for the intrinsic Q for all three wafers are shown in Fig. 7.4. The error bars correspond to the uncertainty of the fits. Wafer 3HS shows values between 1000–1200, while the other two wafers 4HS and 5LS have values nearly twice as high and go up to 2400. It is interesting that the wafers 4HS and 5LS have similar Q_{intr}, even though their InGaP layers greatly differ in gallium content and tensile stress. Both wafers 4HS and 5LS were grown by our collaborators at the *Centre de Nanosciences et de Nanotechnologies, CNRS, Université Paris-Saclay*. Also both InGaP layers of the wafers have a nominal thickness of $100\,\mathrm{nm}$, while wafer 3HS was grown by the *Fraunhofer Institute for Applied Solid State Physics IAF* with an InGaP thickness of $81\,\mathrm{nm}$. All three wafers were grown via MOCVD. The differences in intrinsic Q could be an indication that they could depend on the growth conditions and also on the machines growing the thin films. Since Q_{intr} reflects the number of defects in a material, it would mean that the growth at CNRS produces higher quality material with less defects.

The intrinsic Q factors of all InGaP samples from this work are below 2500. To

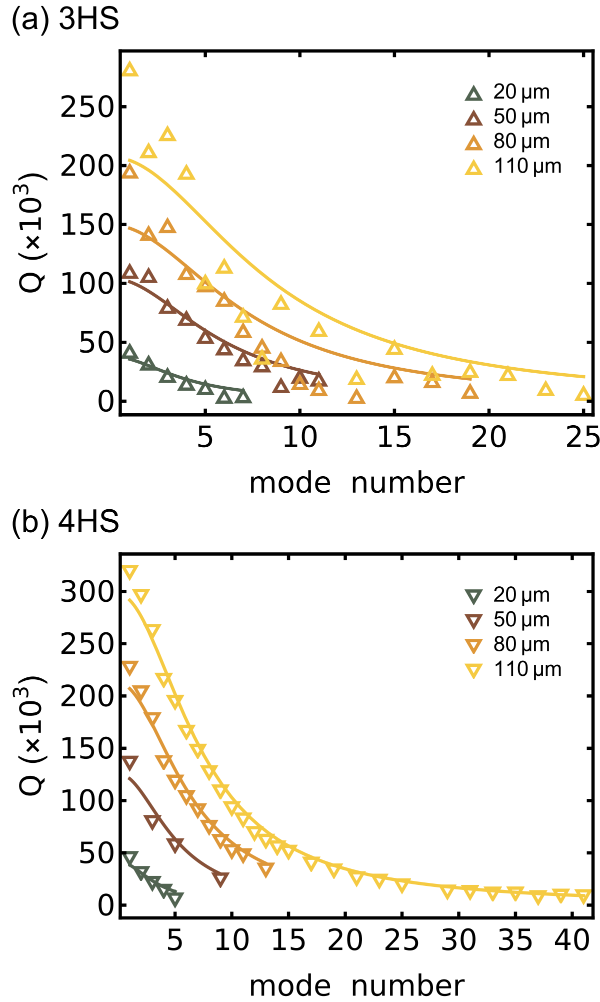

Figure 7.2: Quality factor vs. mode number of the wafers 3HS and 4HS. For clarity only the resonator lengths 20 µm, 50 µm, 80 µm, and 110 µm are shown. The samples were fabricated from the high-stress wafers (a) 3HS and (b) 4HS. For all samples Eq. (2.9) (solid lines) is fit to the data, to extract the intrinsic Q for all the resonator lengths.

classify these values we have to compare them to other materials. The most commonly used material for stressed nanomechanical systems is silicon nitride (SiN). The stoichiometric SiN features a high tensile stress of up to $1.46\,\mathrm{GPa}$ (see Ch. 6), is easy to handle, robust and readily available. Due to its high tensile stress and the resultant dissipation dilution, high Q factors in the range of millions have been achieved by other groups [22, 23].

The extracted Q_{intr} for stoichiometric SiN is in the range of 3000, see Fig. 7.5, while literature values go even up to 4400 [42]. For short resonators the Q_{intr} decreases. It could be that the dissipation dilution model is no longer applicable for

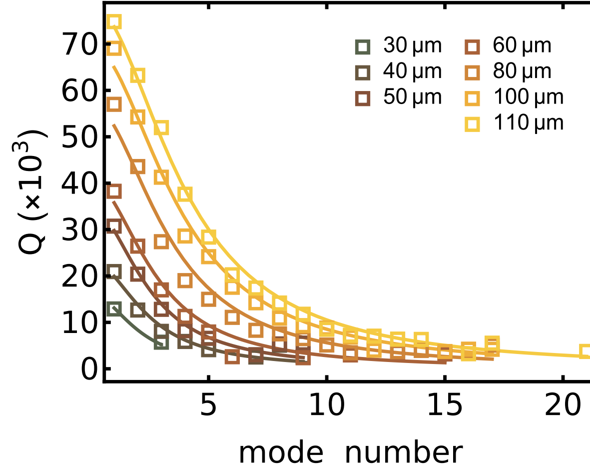

Figure 7.3: Quality factor vs. mode number of string resonators fabricated from the low-stress wafer 5LS. The Q factors go up to $75\,000$. Equation (2.9) (solid lines) is fit to the data to extract the intrinsic Q for all the resonator lengths.

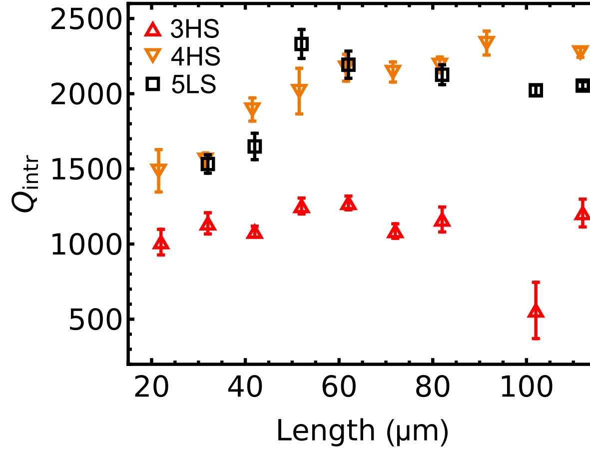

Figure 7.4: Intrinsic Q of InGaP string resonators vs. resonator length for the two high-stress wafers 3HS and 4HS and the low-stress wafer 5LS. The values are extracted by fitting Eq. (2.9) to the Q over mode number data for each resonator length. The error bars correspond to the uncertainty of the fits. Wafer 3HS shows values of around 1100, while the other two wafers have values up to 2400.

short resonators, which leads to lower extracted Q_{intr}, and one would have to perform further tests of the dissipation dilution model for this resonator regime. Another possibility is that for short strings clamping losses could start to dominate and thus reduce Q_{intr} [78].

The extracted SiN values of $Q_{\mathrm{intr}}^{\mathrm{SiN}} \approx 3000$ are at least $20\,\%$ higher than the ones we extracted for InGaP $Q_{\mathrm{intr}}^{\mathrm{InGaP}} < 2500$, which is quite peculiar. SiN is an amorphous material and inherently has a lot of defects due to its microscopic structure [14, 15]. One would assume that InGaP would have very few defects because of its

crystallinity. We therefore expected that InGaP has higher Q_{intr} than SiN, which is not the case as one can clearly see from the measurements. This could support the findings of Villanueva & Schmid [42], where the intrinsic Q of resonators with a thickness below $100\,\mathrm{nm}$ is mainly surface loss limited. It would suggest that higher resonator thicknesses are needed to benefit form InGaP's crystallinity.

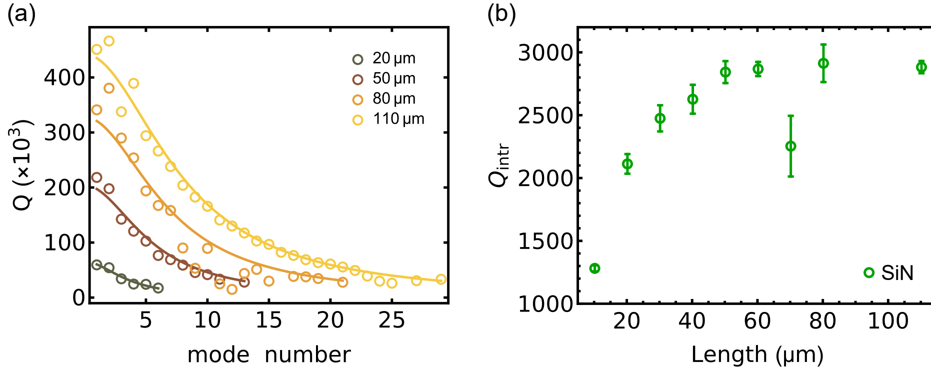

Figure 7.5: Q factors and intrinsic Q of SiN string resonators. (a) Quality factor vs. mode number. For clarity only the resonator lengths $20\,\mu\mathrm{m}$, $50\,\mu\mathrm{m}$, $80\,\mu\mathrm{m}$, and $110\,\mu\mathrm{m}$ are shown. Equation (2.9) (solid lines) is fit to the data, to extract the intrinsic Q for all the resonator lengths. (b) Intrinsic Q of SiN string resonators vs. resonator length, the value goes up to $Q_{\mathrm{intr}}^{\mathrm{SiN}} \approx 3000$. The error bars correspond to the uncertainty of the fits.

Additionally, from HRXRD measurements (see Ch. 5) we know that InGaP is not defect-free. To understand the origin of the defects and their influence on Q_{intr} would require a microscopic material analysis of InGaP. This is however out of the scope of this thesis.

At the end of this discussion I should also mention the quality of the fits from the dissipation dilution model. For all the InGaP resonators the model can not fully reproduce the progression of Q factors vs. the mode number. The quality factors for low mode numbers are mostly above the fitted model and for higher harmonics slightly below the curve. This behavior is most pronounced for wafer 3HS, see Fig. 7.2 (a), but also visible for 5LS, see Fig. 7.3. It seems that the dissipation dilution model can not fully describe the InGaP data. For the SiN the model shows a slightly better agreement with the data, see Fig. 7.5.

To my knowledge this model has so far only been applied for SiN resonators and also only for low numbers of higher harmonics [17, 21, 22, 42]. There it showed good agreement with the data. It is possible that other materials have additional dissipation mechanisms that are not fully captured by this model.

In addition to InGaP, this behavior was also observed in silicon carbide string resonators by my colleague Yannick S. Klaß. Together with Ignacio Wilson-Rae, from the University of York, they are developing an updated dissipation model for a more complete description of nanomechanical string resonators. So at the moment of this thesis this issue is part of current research.

Therefore one should take the accuracy of the intrinsic quality factors with a grain of salt.

7.2 Degradation in Ambient Conditions

Having InGaP samples exposed to air can have negative effects on their structure, as I already showed in Ch. 3.5. A high aluminum content $Al_{0.92}Ga_{0.08}As$ sacrificial layer reacts with the air humidity and this leads to a destruction of the InGaP resonator atop. This can be circumvented by lower Al contents in the AlGaAs layer. The humidity no longer destroys the samples. However, the ambient conditions still influence the mechanical properties of the resonators, as I will show in this section.

To investigate the influence of ambient air on InGaP string resonators, the frequency response of resonators with varying length was measured right after fabrication and after some time exposed to ambient air. The sample was fabricated from wafer 3HS. All the measurements are performed under vacuum. Afterwards the sample is taken out of the vacuum chamber and stored under ambient conditions in the laboratory for 13 days. Then the sample is put back into the measurement setup, again in vacuum. The frequency measurements are now repeated on the same resonators.

Figure 7.6 shows resonance frequencies vs. mode number, as an example for the resonator lengths $40\,\mu\text{m}$ and $110\,\mu\text{m}$. The resonance frequencies coincide both times, therefore the exposure to air does not influence the frequency. This indicates that the tensile stress did not change. We can now fit Eq. (2.2) to the data points and extract the tensile stress for various resonator lengths, as in described in Ch. 6. The stress is depicted in Fig. 7.7. Again we see the length dependence. The changes due to air exposure on the stress are only minor, and no clear trend of an influence of the air is visible.

The situation changes when one looks at the Q factors. Figure 7.8 shows Q factors as a function of the mode number, of the same resonators as in Fig. 7.6. But after the resonators have been exposed to air, their Q factor is decreased. Nearly all Q factors are below the previously measured values. When we again fit Eq. (2.9) to this Q factor data, we can obtain Q_{intr}. All the extracted values are displayed in Fig. 7.9. The error bars correspond to the uncertainty of the fits. It is clearly visible that the exposure to air reduced the intrinsic Q for all resonator lengths. Before air exposure the intrinsic Q has a mean value of $Q_{\text{intr}} = 1085(215)$. After the air exposure it is reduced down to $Q_{\text{intr}}^{\text{air}} = 756(140)$. This is a change of about $40\,\%$.

Even though the dissipation dilution model again does not fully reproduce the data, the reduction in Q_{intr} is clear and also visible in the raw quality factor data. Since the resonance frequencies and tensile stress did not change due to air exposure, this drop in Q factors has to come from additional dissipation.

The origin of this detrimental effect is still unclear. But most likely the surface reacts with the air or air humidity, which leads to defects at the surface. It has been shown in GaAs disk resonators, by the group of our collaborator Ivan Favero at the

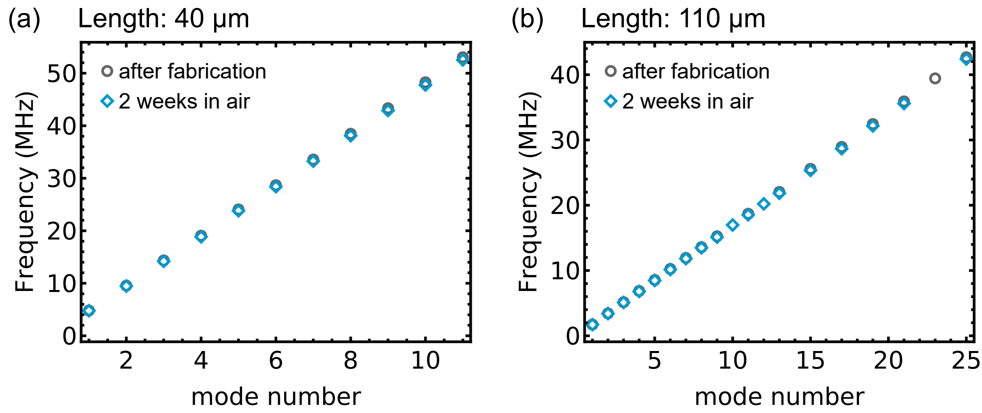

Figure 7.6: Influence of ambient air on the frequency. Resonance frequency vs. mode number, shown for the two resonator lengths (a) 40 μm and (b) 110 μm. The measurements were done right after fabrication (gray circles) and after 2 weeks in air (blue diamonds). The frequencies before and after air exposure are the same, indicating that the tensile stress did not relax.

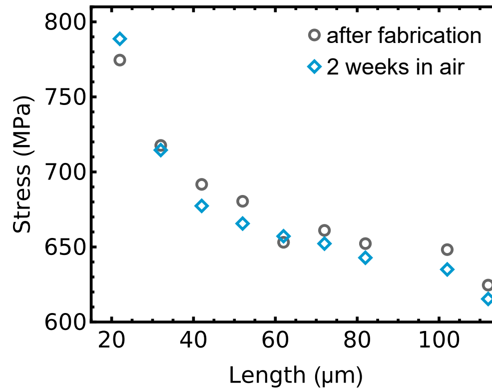

Figure 7.7: Tensile stress vs. resonator length before (gray circles) and after (blue diamonds) air exposure. The air exposure has only minor effects on the tensile stress.

Université Paris Diderot, that an amorphous reconstruction layer is forming at the surface due to air humidity [79]. A similar observation was made for single-crystal silicon [11]. There a layer of native SiO_2 forms under ambient air exposure, which reduces the mechanical quality factor. In both cases the dissipation is increased by the amorphous surface layer.

It is possible, that InGaP also forms an amorphous surface layer when it is exposed to ambient air. Therefore, the increasing number of surface defects degrade the mechanical Q of the InGaP samples

If one wants to perform measurements on high quality resonators one has to make sure to install them in a vacuum chamber right after fabrication and minimize air exposure. Another possible way to tackle this problem will be discussed in the

following section. There we look into surface treatments to stop the degradation.

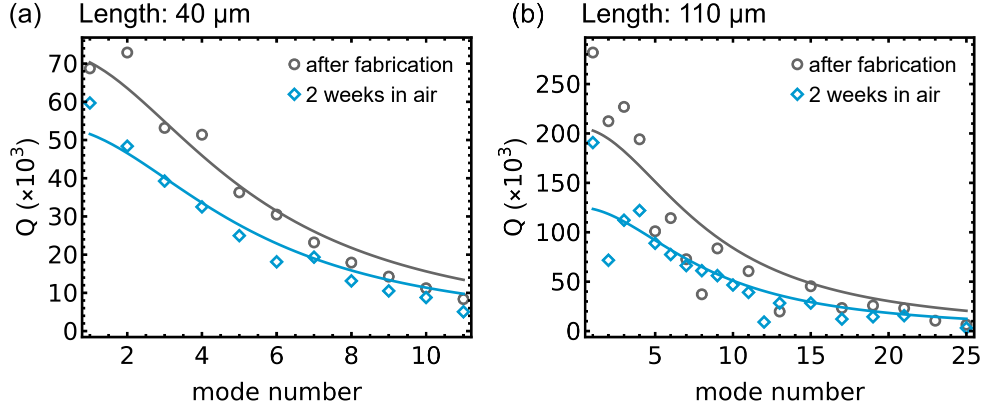

Figure 7.8: Influence of ambient air on the Q factor. Quality factor vs. mode number, shown for the two resonator lengths (a) $40\,\mu\mathrm{m}$ and (b) $110\,\mu\mathrm{m}$. The measurements were done right after fabrication (gray circles) and after 2 weeks in air (blue diamonds). The Q factors are lowered due to the air exposure. The solid lines are fits of Eq. (2.9) to the data, to extract the intrinsic Q factors.

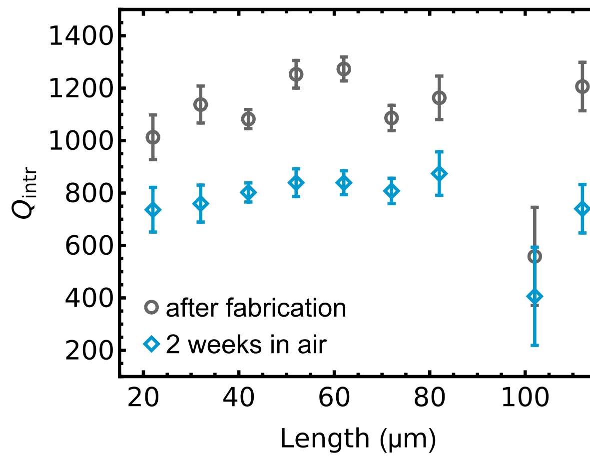

Figure 7.9: Influence of ambient air on the intrinsic Q. Intrinsic Q factors vs. resonator length. The measurements were done right after fabrication (gray circles) and after 2 weeks in air (blue diamonds). The values are obtained by fitting Eq. (2.9) to the Q factors vs. mode number for each resonator length, cf. Fig. 7.8. The error bars correspond to the uncertainty of the fits. Before air exposure the intrinsic Q has a mean value of $Q_{\mathrm{intr}} = 1085(215)$. After the air exposure it is reduced to $Q_{\mathrm{intr}}^{\mathrm{air}} = 756(140)$. We can clearly see, that the exposure to air reduces the Q_{intr}, and hence increasing the internal dissipation.

7.3 Passivation by Atomic Layer Deposition

As it was already mentioned, the group of our collaborator Ivan Favero showed that GaAs forms an amorphous surface reconstruction layer when it is exposed to ambient conditions [79]. In their following work [80] they introduced methods to modify the resonators surface. They use atomic layer deposition (ALD) to passivate the surface. First they remove the surface reconstruction layer by an hydrogen plasma. Then they grow few nanometers of alumina (Al_2O_3) via plasma-enhanced ALD. The advantage of alumina is that it is stable under ambient conditions, thus protecting the GaAs. This method significantly enhanced their resonators' optical properties [80]. In a further work, they looked into the changes of the mechanical properties [81]. Their main findings are that the ALD of alumina adds defects and thus dissipation to their samples. This is because alumina itself is an amorphous material and has a lot of intrinsic defects. In the end one removes an amorphous reconstruction layer and replaces it with another amorphous layer.

However, an alumina layer can still be beneficial. It is a stable layer that can prevent further deterioration of the surface. This would make handling and storage of samples a lot easier. In the end one has to balance both effects, depending on the application.

Samples were fabricated from the 3HS wafer. After the fabrication, some of resonators where characterized to verify that the resonators are fine. Then I sent the samples to France, to the Group of Ivan Favero for the ALD treatment. The ALD was performed by Cherif Belacel. A hydrogen plasma process was carried out to clean the surface and then he grew $8\,\mathrm{nm}$ of alumina on the InGaP resonators.

In Fig. 7.10 we can see changes of the ALD treatment on the InGaP resonators. The resonance frequencies are lower than before the ALD of alumina. It has been shown, that the deposition of a stress-free material on a stressed resonator can reduce the effective stress of the bilayer system [82]. This might be even more pronounced in the case of ALD, since it covers all sides of the resonator.

The lowered frequency obviously translates to lower extracted stress values, as we see in Fig. 7.11. Note that the stress values extracted for this sample are below the value of other samples made from the same wafer, e.g. see Fig. 7.7, even for the measurements before the ALD treatment.

Even though the tensile stress is smaller for this sample, it still has relatively high Q factors as we see in Fig. 7.12.

Again we use the dissipation dilution model to extract the intrinsic Q factors, shown in Fig. 7.13. The error bars correspond to the uncertainty of the fits. Because of the relative low stress and the high Q factors of this sample, the intrinsic Q factors are quite high before ALD. The mean value is $Q_{\mathrm{intr}} = 1551(176)$. The ALD treatment decreased this value down to $Q_{\mathrm{intr}}^{\mathrm{ALD}} = 721(34)$. This value is similar to the sample that has been exposed to air for two weeks, which means that ALD could not conserve the Q factors.

All in all, the treatment did not have a beneficial effect on the quality factors. One problem might be that the sample was sent by mail to France where the alumina

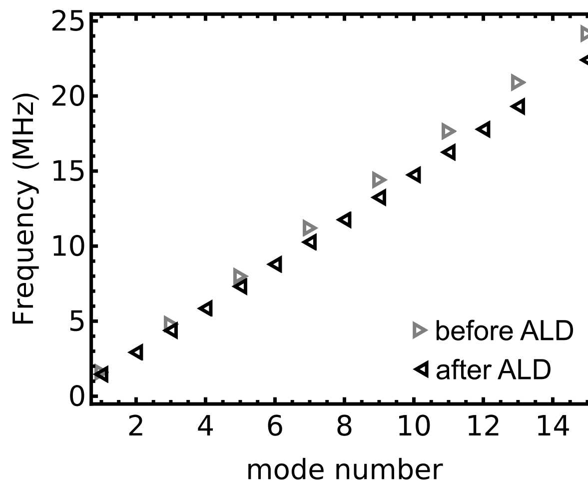

Figure 7.10: Frequency vs. mode number before (gray right-triangle) and after (black left-triangle) ALD of alumina, of a $110\,\mu\mathrm{m}$ long string resonator.

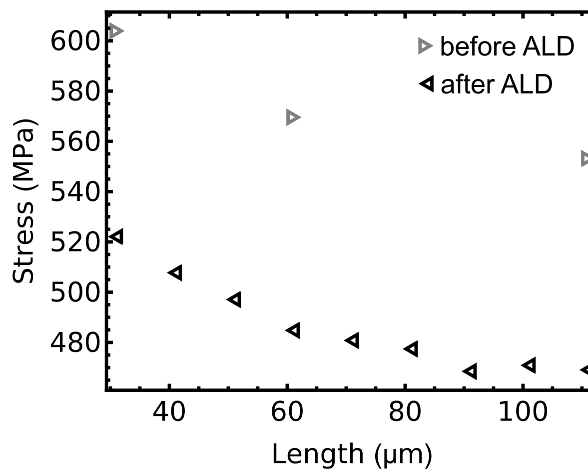

Figure 7.11: Tensile stress vs. resonator length before (gray right-triangle) and after (black left-triangle) ALD of alumina. Note that the stress of this sample before the treatment is already lower than samples from the same wafer, e.g. see Fig. 7.7.

was deposited. During this time, the sample was exposed to ambient conditions, already attacking the InGaP. The hydrogen plasma clean prior to the ALD might not have completely removed the surface reconstruction layer. Thus keeping the bad Q factors because of air exposure. Even though it cannot be completely ruled out that the shipment of the samples led to the bad quality factors, it seems more likely that the amorphous alumina layer leads to an increased dissipation due to two-level systems [81].

On the first glance, the ALD of alumina seems not to be a good choice, since the Q factors are reduced significantly. However the possible long term benefits have yet to be determined. Namely how the Q factors will develop on longer time scales and

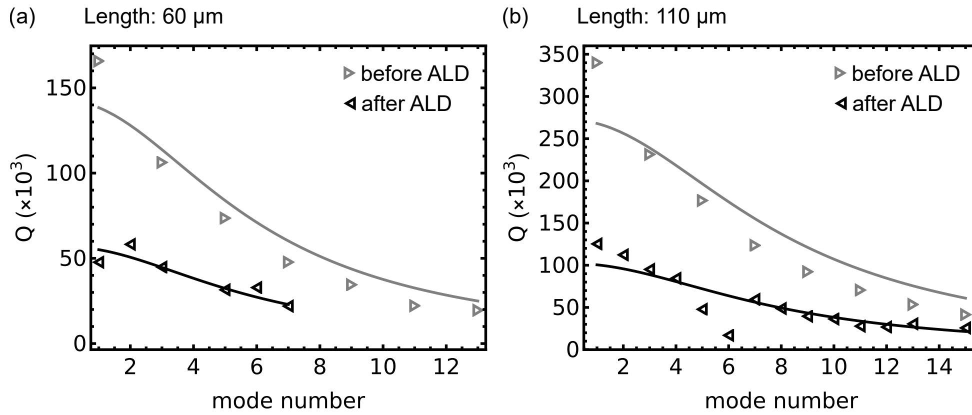

Figure 7.12: Quality factor vs. mode number before (gray right-triangle) and after (black left-triangle) ALD of alumina. Shown here are the Q factors of a (a) $60\,\mu\mathrm{m}$ and (b) $110\,\mu\mathrm{m}$ long string. The Q factors are lowered due to ALD of alumina. The solid lines are fits of Eq. (2.9) to the data, to extract the intrinsic Q factors.

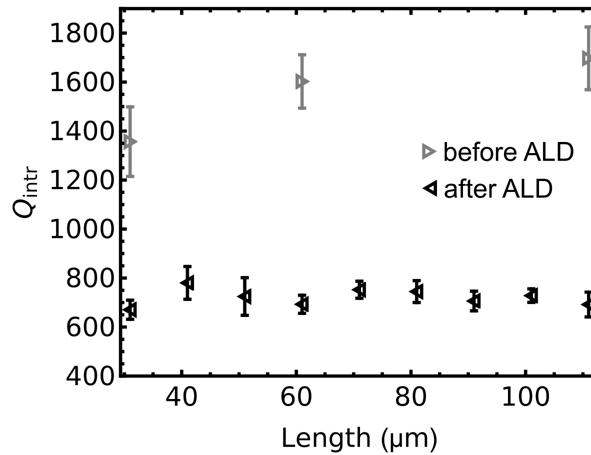

Figure 7.13: Influence of ambient air on the intrinsic Q. Intrinsic Q vs. resonator length before (gray right-triangle) and after (black left-triangle) ALD of alumina. The values are obtained by fitting Eq. (2.9) to the Q factors vs. mode number for each resonator length, cf. Fig. 7.12. The error bars correspond to uncertainty of the fits. Before ALD the intrinsic Q has a mean value of $Q_{\mathrm{intr}} = 1551(176)$ and after ALD it is reduced to $Q_{\mathrm{intr}}^{\mathrm{ALD}} = 721(34)$. This is a similar value as for the resonators that were exposed to air for two weeks.

if the ALD samples do not further degrade. Also one could think about depositing other materials than alumina, which could add less dissipation.

Another possible alternative could be the use of rapid thermal oxidation. This was already used to passivate the high Al content AlGaAs sacrificial layer, see Ch. 3.5. Here again a thin oxide layer could form on the InGaP surface and stop further attack on resonators.

At this point it is also not clear if the reason for the degradation of InGaP is

caused by a surface reconstruction layer, since this has only been shown for GaAs. However we know that the sacrificial AlGaAs layer reacts with air, depending on the Al content. It could be possible that the AlGaAs changes and therefore influence the mechanical properties of InGaP, e.g. influencing the clamping conditions. We already know that we can passivate AlGaAs by RTO. So this would also be a solution for this possible degradation.

Performing RTO on freely suspended InGaP resonators could provide further insights on dissipation mechanisms in InGaP, fostering an even deeper understanding of nanomechanical systems.

CHAPTER 8

Conclusion

This thesis deals with nanomechanical systems based on crystalline $In_{1-x}Ga_xP$. By changing the Ga content x it is possible to change the tensile stress in the InGaP thin film. The investigated nanomechanical resonators feature stresses of up to $775\,\mathrm{MPa}$ for $x = 59.2\,\%$. The quality factor is an important figure of merit for nanomechanical systems. Dissipation dilution facilitates high Q factors, because the tensile stress increases the stored energy. Additionally one hopes to decrease dissipation by using crystalline materials and thus further increase the Q.

During my thesis project I investigated doubly-clamped string resonators fabricated from $In_{1-x}Ga_xP$ with various compositions. Those range from the nearly stress-free case $In_{0.486}Ga_{0.514}P$ to the high tensile stress regime $In_{0.408}Ga_{0.592}P$.

The first goal of my thesis project was to implement a fabrication process for InGaP string resonators, since this material was new to our group. The initial fabrication was accompanied with some obstacles. III-V heterostructures are fragile and prone to break easily, which is even more pronounced for the low-stress material. This obstacle could be tackled by careful sample handling and critical point drying.

The detrimental hydrolysis of high Al content AlGaAs posed a bigger problem. The degradation starts directly after the anisotropic ICP etching. This complicated the optimization of the following process steps. Also one could not take breaks until the fabrication is done and the sample is mounted in the vacuum chamber to minimize air exposure. By thorough planning of the process steps, it was possible to fabricate the first InGaP string resonators and establish a high yield fabrication flow.

With those resonators I could investigate an orientation dependent stress with a maximum value of $650\,\mathrm{MPa}$. The anisotropic Young's modulus leads to an angular dependence of the tensile stress. Defects in the InGaP thin film change the elastic properties, which breaks the theoretical $90°$ symmetry of the tensile stress in the (100) crystal plane. With the combination of both effects, we observe a stress variation of up to $50\,\%$ as a function of the crystal orientation.

Despite the challenges of the first generation wafers we gained a lot of knowl-

edge about crystals and III-V semiconductors in particular. This led to tremendous improvements in the heterostructure of new InGaP wafers. The new and improved InGaP wafers facilitated a reliable and high yield fabrication of high Q string resonators with lengths above $100\,\mu\mathrm{m}$. In combination with the improved optical characterization setup at a wavelength of $1550\,\mathrm{nm}$ it was possible to measure numerous higher harmonics of the vibrational resonator modes. With this I could extract more precise mechanical properties.

With the measurement of several higher harmonic modes one can extract the tensile stress of a single string resonator. Doing this for different resonator lengths revealed a length dependent stress of doubly-clamped resonators. Moreover this behavior is not unique to InGaP and is also shown for SiN string resonators. It is an intrinsic design property of tensile stressed doubly-clamped nanomechanical resonators. A simple, material independent, theoretical model based on elastic theory was developed to quantitatively and qualitatively describe this universal phenomenon. The theoretical model perfectly reproduces the measured data with the need of only one fit parameter for the InGaP material system. This is an additional mechanism to tune the tensile stress of string resonators, which can be changed by more than $20\,\%$ as a function of the resonator length. Enabling more accurate stress tuning with the chosen resonator design.

In the last part of this thesis, I had a closer look on the mechanical quality factor of the InGaP resonators. The Q factors reach values above $300\,000$ for resonance frequencies around $1.5\,\mathrm{MHz}$ for the high-stress InGaP wafers 3HS and 4HS. Also the low-stress wafer 5LS shows high quality factors of up to $75\,000$, even though the stress is an order of magnitude below the high-stress wafers. By applying the dissipation dilution model one can extract the intrinsic quality factor of the InGaP wafers, which is an indication of the defects inside a material. The dissipation dilution model yields intrinsic Q values of up to 2400. Averaging the Q_{intr} for the different resonator lengths gives an average value of about 2000 for the 4HS and 5LS wafers. The 3HS wafer only has an average Q_{intr} of 1000. This could indicate that the intrinsic quality depends on the growth conditions, since the wafer 3HS was grown in a different machine. The growth process and growth conditions might be an important parameter to achieve high Q resonators. Additionally the intrinsic Q of the InGaP resonators reduces when subjected to air. One possible explanation might be that the surface of the resonators react with the ambient air, which leads to an amorphous surface reconstruction layer. This might add surface defects and thus decrease the intrinsic Q over time. To tackle this problem a passivation technique with ALD was tested. A thin layer of $8\,\mathrm{nm}$ alumina was deposited on the resonators to block the air from degrading them. However, this layer of alumina also reduces the intrinsic Q because of its amorphous nature and the corresponding defects. One might deposit a thinner layer of alumina or even try other materials that add less defects. Rapid thermal oxidation might be another way to passivate the resonators. There is a possibility that InGaP forms a thin and stable oxide layer similar to RTO treated AlGaAs. One would have to check how thick such a layer would be and how many defects it would add.

When comparing the Q_{intr} with other materials, the value for InGaP is lower than the one of SiN. Even though crystalline resonators promise higher intrinsic Qs due to their crystalline structure, the experimental results have shown the opposite. This might be due to the detrimental surface effects such as the formation of oxide layers and the accompanied creation of additional material defects during fabrication, as well as detrimental material effects over time. Future temperature dependent Q factor measurements could help to get further insights to the dissipation mechanisms and the types of defects in InGaP resonators [14, 81]. This is topic of ongoing research within our group.

Furthermore, one can think about implementing on-chip dielectric actuation [83] and microwave-cavity based detection [19] schemes. By fabricating electrodes close to the resonator it would be possible to have on-chip access to the resonator without the need of optical components. This requires the development of additional fabrication processes for the electrodes on the semiconducting substrate, to prevent leakage currents particularly when operating at room temperature.

Appendix

A InGaP Wafers

Table A.1: Structure of wafer 1HS, by courtesy of our collaborator Garrett D. Cole.
The high-stress InGaP wafer with Ga content of $x_{\mathrm{1HS}} = 58.7\,\%$ and InGaP thickness of $86\,\mathrm{nm}$ was grown using MBE by the company *IQE NC*. The wafer identification is: 056164-069SU.
The GaAs/$Al_yGa_{1-y}As$ superlattice is a distributed Bragg reflector intended to be used by our collaborator in optomechanical experiments. Additionally both InGaP layers are each capped by $1\,\mathrm{nm}$ of GaAs.

Layer	Repeat	Material	Thickness (µm)
0	1	GaAs substrate	—
1	1	$Al_{0.925}Ga_{0.075}As$	0.2720
2	41	GaAs $Al_{0.925}Ga_{0.075}As$	0.0780 0.0906
3	1	GaAs	0.0780
4	1	$Al_{0.925}Ga_{0.075}As$	1.0653
5	1	GaAs	0.0010
6	1	$In_{0.413}Ga_{0.587}P$	0.0855
7	1	GaAs	0.0010
8	1	$Al_{0.925}Ga_{0.075}As$	0.2646
9	1	GaAs	0.0010
10	1	$In_{0.413}Ga_{0.587}P$	0.0855
11	1	GaAs	0.0010

Table A.2: Structure of wafer 2LS, by courtesy of our collaborator Garrett D. Cole.
The low-stress InGaP wafer with Ga content of $x_{2\mathrm{LS}} = 52.8\,\%$ and InGaP thickness of $86\,\mathrm{nm}$ was grown using MBE by the company *IQE NC*. The wafer identification is 056164-068SU.
The GaAs/$\mathrm{Al}_y\mathrm{Ga}_{1-y}$As superlattice is a distributed Bragg reflector intended to be used by our collaborator in optomechanical experiments. Additionally both InGaP layers are each capped by $1\,\mathrm{nm}$ of GaAs.

Layer	Repeat	Material	Thickness (µm)
0	1	GaAs substrate	—
1	1	$Al_{0.921}Ga_{0.079}As$	0.2720
2	41	GaAs $Al_{0.921}Ga_{0.079}As$	0.0780 0.0906
3	1	GaAs	0.0780
4	1	$Al_{0.921}Ga_{0.079}As$	1.0653
5	1	GaAs	0.0010
6	1	$In_{0.472}Ga_{0.528}P$	0.0859
7	1	GaAs	0.0010
8	1	$Al_{0.921}Ga_{0.079}As$	0.2646
9	1	GaAs	0.0010
10	1	$In_{0.472}Ga_{0.528}P$	0.0859
11	1	GaAs	0.0010

Table A.3: Structure of wafer 3HS.
The high-stress InGaP wafer with Ga content of $x_{3\mathrm{HS}} = 59.2\,\%$ and InGaP thickness of $81\,\mathrm{nm}$ was grown using MOCVD by the *Fraunhofer Institute for Applied Solid State Physics IAF*. The wafer identification is: F0278B.
The InGaP layer is capped by $1\,\mathrm{nm}$ of GaAs.

Layer	Repeat	Material	Thickness (µm)
0	1	GaAs substrate	—
1	1	GaAs	0.0500
2	1	$Al_{0.555}Ga_{0.445}As$	1.0000
3	1	GaAs	0.0010
4	1	$In_{0.408}Ga_{0.592}P$	0.0808
5	1	GaAs	0.0010

Table A.4: Structure of wafer 4HS, by courtesy of our collaborator Rémy Braive.
The high-stress InGaP wafer with Ga content of $x_{4\mathrm{HS}} = 58.5\,\%$ and InGaP thickness of $100\,\mathrm{nm}$ was grown using MOCVD at the *Centre de Nanosciences et de Nanotechnologies, CNRS, Université Paris-Saclay*. The wafer identification is: V0218.

Layer	Repeat	Material	Thickness (μm)
0	1	GaAs substrate	—
1	1	$Al_{0.85}Ga_{0.15}As$	1.0000
2	1	$In_{0.415}Ga_{0.585}P$	0.1000

Table A.5: Structure of wafer 5LS, by courtesy of our collaborator Rémy Braive.
The low-stress InGaP wafer with Ga content of $x_{5\mathrm{LS}} = 51.4\,\%$ and InGaP thickness of $100\,\mathrm{nm}$ was grown using MOCVD by our collaborators at the *Centre de Nanosciences et de Nanotechnologies, CNRS, Université Paris-Saclay*. The wafer identification is: V0221.

Layer	Repeat	Material	Thickness (μm)
0	1	GaAs substrate	—
1	1	$Al_{0.85}Ga_{0.15}As$	1.0000
2	1	$In_{0.486}Ga_{0.514}P$	0.1000

Appendix

B Fabrication Details

Table B.1: Fabrication preparations

Process step	Equipment	Parameters
Preparations	Spin coater + resist	Protective layer for wafer frontside
	Hotplate	Bake resist: at least 5 min @ 90 °C
	Diamond scriber	cleave wafer Small scratch on sample side Labeling on backside
Cleaning	Acetone IPA N_2	At least 1 min At least 1 min Drying

Table B.2: Lithography

Process step	Equipment	Parameters
Adhesion promoter	Spin coater TI-Prime	Ramp up: $2.5\,\mathrm{s}$ @ $800\,\mathrm{rpm}$, Accel. $800\,\mathrm{rpm/s}$ Spin: $45\,\mathrm{s}$ @ $4000\,\mathrm{rpm}$, Accel. $2000\,\mathrm{rpm/s}$ Ramp down: $3\,\mathrm{s}$, Accel. $-2000\,\mathrm{rpm/s}$
Bake	Hotplate	$2\,\mathrm{min}$ @ $120\,°\mathrm{C}$
Resist	Spin coater ma-N 2403	Ramp up: $1\,\mathrm{s}$ @ $800\,\mathrm{rpm}$, Accel. $800\,\mathrm{rpm/s}$ Spin: $33\,\mathrm{s}$ @ $6000\,\mathrm{rpm}$, Accel. $2000\,\mathrm{rpm/s}$ Ramp down: $3\,\mathrm{s}$, Accel. $-2000\,\mathrm{rpm/s}$
Softbake	Hotplate	$65\,\mathrm{s}$ @ $90\,°\mathrm{C}$
Lithography Elphy	SEM Zeiss Crossbeam	Aperture: $10\,\mathrm{\mu m}$ Accel. voltage: $10\,\mathrm{kV}$ Working distance: $8.6\,\mathrm{mm}$ Dose: $40\,\mathrm{\mu C/cm^2}$ Clamping point: $100\,\%$ dose Beam: $140\,\%$ dose
Lithography Neomicra	SEM Zeiss Crossbeam	Aperture: $20\,\mathrm{\mu m}$ (fast with slight errors) Aperture: $10\,\mathrm{\mu m}$ (slower with less errors) Accel. voltage: $10\,\mathrm{kV}$ Working distance: $8.6\,\mathrm{mm}$ Dose: $40\,\mathrm{\mu C/cm^2}$ Clamping point: $100\,\%$ dose Beam: $140\,\%$ dose
Develop	ma-D 525	$4 \times 20\,\mathrm{s}$ Each at least $30\,\mathrm{s}$ in DI Water Drying with N_2
Hardbake	Convection oven	$10\,\mathrm{min}$ @ $120\,°\mathrm{C}$

Table B.3: Etching

Process step	Equipment	Parameters
Etch: anisotropic	ICP-RIE	Etch time: 3:24 min:s ICP-Power: 250 W RF-Power: 60 W Flow rate $SiCl_4$: 1.5 sccm Flow rate Ar: 4.5 sccm Pressure: 1.5 mTorr Temperature: 30 °C
Cleaning (ICP chlorine residues)	DI water IPA N_2	10 min At least 1 min Drying
Resist removal (etch mask)	Plasma cleaner	5 min O_2 plasma (level: Hi)
Wet etch: isotropic	Depending on sacrificial material: see Tab. B.4 DI water	 At least 1 min
Digital wet etch (optional)	H_2O_2 (30 %) DI water KOH (10 g/100 mL H_2O) DI water	15 s At least 1 min 30 s At least 1 min
Final rinsing bath	IPA	At least 1 min
Critical point drying	Critical point dryer	Critical point of CO_2

Table B.4: Wet etch solutions and etch rates

Material	Etch solution	Etch rate
Wet etch $Al_{0.92}Ga_{0.08}As$	Buffered oxide etch (BHF)	≈ 50–90 nm/s
Wet etch $Al_{0.55}Ga_{0.45}As$	H_2SO_4(95 %):H_2O_2(30 %):H_2O (1:1:30) - mix properly	≈ 3–5 nm/s
Wet etch $Al_{0.85}Ga_{0.15}As$	H_2SO_4(95 %):H_2O_2(30 %):H_2O (1:1:30) - mix properly	≈ 8 nm/s
Wet etch GaAs	H_3PO_4(85 %):H_2O_2(30 %):H_2O (1:1:30) - mix properly	≈ 1 nm/s
Wet etch InGaP	HCl(37 %):H_3PO_4(85 %) (1:1) - mix properly	≈ 3 nm/s

APPENDIX

C High Resolution X-Ray Diffraction Measurements

The following chapter is based on parts of the publication:

[47] M. Bückle, V. C. Hauber, G. D. Cole, C. Gärtner, U. Zeimer, J. Grenzer, and E. M. Weig. Stress control of tensile-strained $In_{1-x}Ga_xP$ nanomechanical string resonators. *Applied Physics Letters*, 113(20):201903, 2018.

The HRXRD measurements were performed and evaluated by Jörg Grenzer. The description of the characterization setup was written by Jörg Grenzer. Writing of the measurement description was done by me.
Text and figures are reproduced from [47], with the permission of AIP Publishing.

High resolution x-ray diffraction (using Cu-$K_{\alpha 1}$ radiation) is implemented for the characterization of the structural properties as a non-destructive method with a very high sensitivity to lattice parameter changes [46, 84]. The x-rays scatter from the electronic density of the crystal, reproducing the lattice planes of the crystal. Measuring the angle of the scattered x-rays and using Bragg's law it is possible to calculate the distance between lattice planes, which can be related to the lattice constant of the crystal. Thin, mismatched layers distort tetragonally and therefore the lattice parameter parallel to the wafer surface differs from the perpendicular one, $a_{\mathrm{L}}^{\parallel} \neq a_{\mathrm{L}}^{\perp}$.

The reciprocal space maps were performed using an θ-θ Empyrean (panalytical) diffractometer equipped with a combination of a Goebel mirror and a single channel cut (Ge220) monochromator on the source side. The scattered intensity was collected using a Pixcel 2D detector (514×514 pixels at $55\,\mu\mathrm{m}$). The HRXRD line scans (Fig. C.4) were done with a Seifert-GE XRD3003HR diffractometer using a point focus equipped with an spherical 2D Goebel mirror allowing a beam size in the order of $1\,\mathrm{mm}$ horizontally and vertically. A Bartels monochromator and a triple-axis analyzer in front of a scintillation counter were installed to achieve the highest resolution in reciprocal space.

HRXRD measurements on high-stress InGaP wafer

From symmetric RSMs, i.e. the 002 and 004 reflections of Fig. C.1 and C.2, one can extract the perpendicular lattice constant. The following symmetric RSMs show a strong GaAs substrate peak at wave-vectors of about $Q^{002}_{\mathrm{S}[001]} \approx 2.223\,\text{Å}^{-1}$ and $Q^{004}_{\mathrm{S}[001]} \approx 4.446\,\text{Å}^{-1}$, for the 002 and 004 reflection respectively. This corresponds to the substrate lattice constant of $a_{\mathrm{S}} = 5.653\,\text{Å}$. The layer peak of InGaP can be seen at $Q^{002}_{\mathrm{L}[001]} \approx 2.246\,\text{Å}^{-1}$ and $Q^{004}_{\mathrm{L}[001]} \approx 4.493\,\text{Å}^{-1}$ and corresponds to the strained, perpendicular lattice constant $a^{\perp}_{\mathrm{L}} = 5.595\,\text{Å}$.

When additionally measuring asymmetric RSMs, the 224 reflections of Fig. C.1 and C.2 and the 404 reflections of Fig. C.3, it is possible to extract the parallel lattice parameters from the peak position on the $Q_{[110]}$ axis. Since both the substrate and layer peak have the same $Q_{[110]}$ component, their parallel lattice constants equal: $a_{\mathrm{S}} = a^{\parallel}_{\mathrm{L}} = 5.653\,\text{Å}$, this is true for all the scan directions ([110], [$\bar{1}$10], [010], [$\bar{1}$00]).

We can clearly see with these findings, $a_{\mathrm{S}} = a^{\parallel}_{\mathrm{L}} \neq a^{\perp}_{\mathrm{L}}$, that the high-stress InGaP wafer is 100 % pseudomorphic.

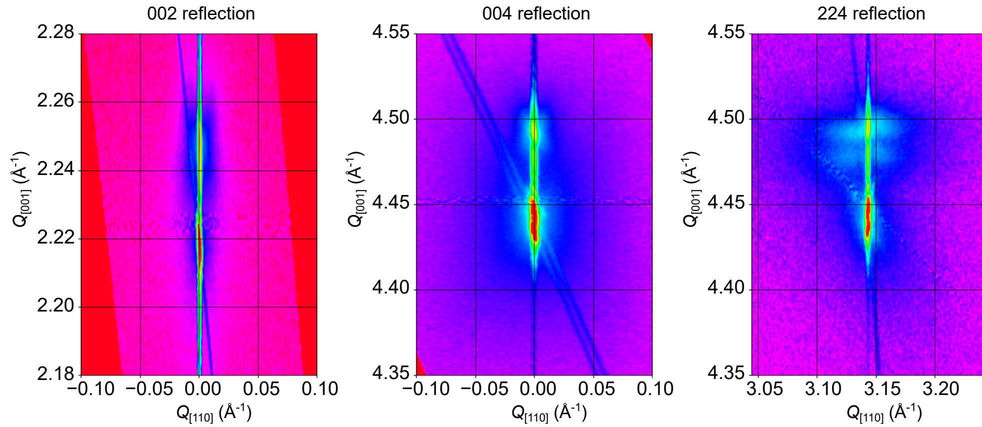

Figure C.1: HRXRD reciprocal space maps depicting the symmetric 002 and 004 and asymmetric 224 reflections of the 1HS wafer for a x-ray beam oriented along the [110] direction. Reproduced from [47], with the permission of AIP Publishing

In addition to the RSMs, to get further insight on the strain, one can look at a reflection curve as a function of scattering angle to extract structural information from the epitaxial structure. Figure C.4 shows a HRXRD curve of the 002 reflection in blue. The substrate peak can be seen at a scattering angle of about 31.6°, and the InGaP layer peak at about 32°. The smaller, regularly distributed peaks arise from the GaAs/AlGaAs super-lattice. By simulating and fitting the slow and rapid oscillations of the curve, it is possible to extract the thicknesses and compositions of the different layers in a heterostructure. The simulation, red line in Fig. C.4, is done with the heterostructure of Tab. C.1. The nominal heterostructure composition is shown in Tab. C.2. From the measurement one can see, that the two InGaP layers have different

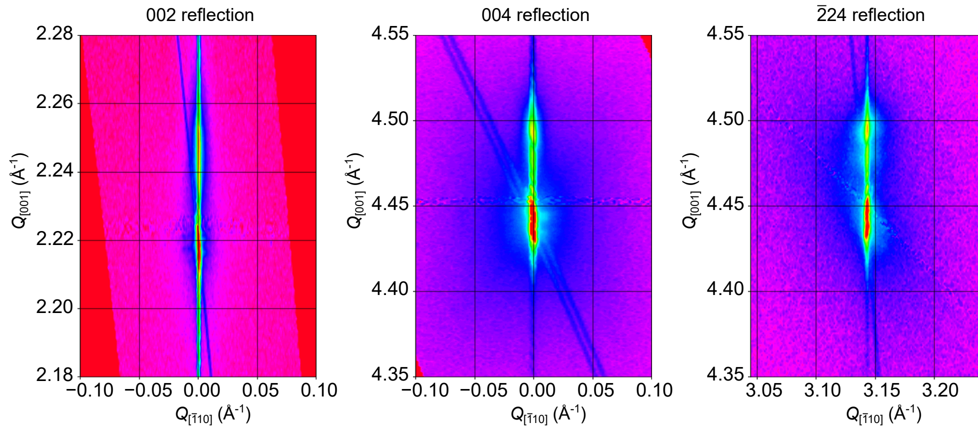

Figure C.2: HRXRD reciprocal space maps depicting the symmetric 002 and 004 and asymmetric $\bar{2}24$ reflections of the 1HS wafer for a x-ray beam oriented along the $[\bar{1}10]$ direction. Reproduced from [47], with the permission of AIP Publishing

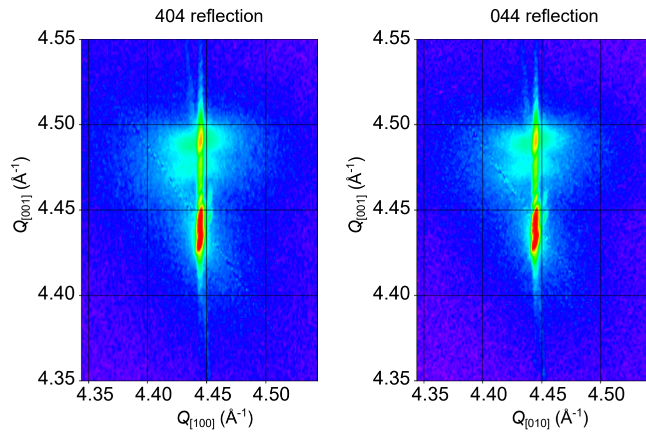

Figure C.3: HRXRD reciprocal space maps depicting 404 and 044 reflection of the 1HS wafer. On the left the beam is along the $[100]$ and on the right along the $[010]$. Reproduced from [47], with the permission of AIP Publishing

compositions and also point to an In gradient along the growth direction. We have not taken into account the compositional gradients in our calculations in the previous section. This will be subject to follow-on work.

HRXRD measurements on low-stress InGaP wafer and comparison to high-stress InGaP

For the low-stress wafer we performed the same RSM measurements as in subsection C. Due to the lower lattice mismatch the InGaP layer peak, at about $Q^{004}_{\mathrm{L}[001]} \approx 4.452\,\text{Å}^{-1}$, is located close to the underlying substrate and AlGaAs super-lattice

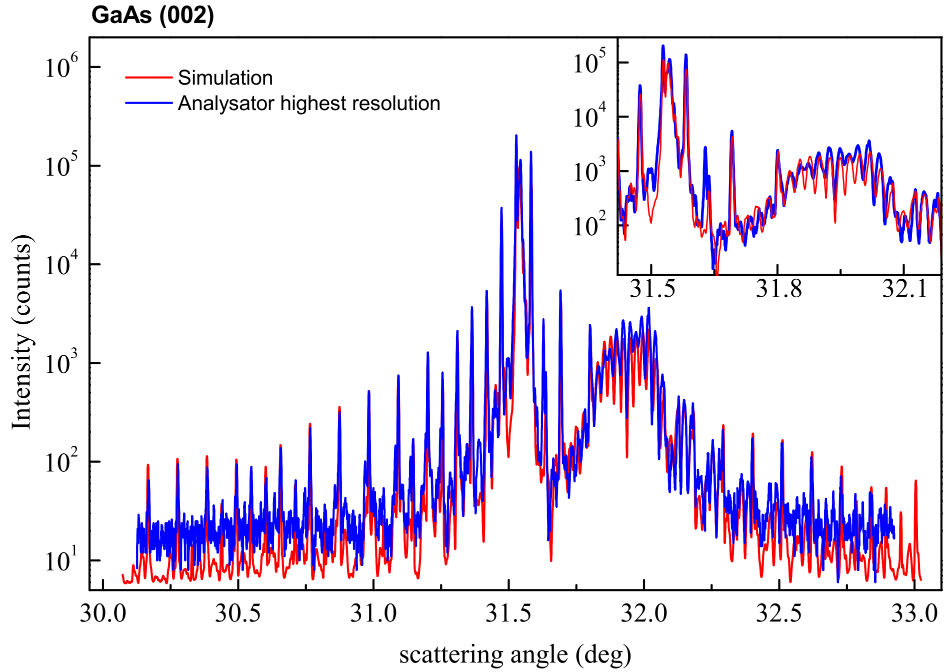

Figure C.4: HRXRD curve of the 002 reflection of the 1HS wafer. Fitting the simulation (red) to the signal (blue) leads to the layer-compositions and -thicknesses shown in Table C.1. Inset: Zoom-in on the InGaP peak at a scattering angle of about 32 degree. Reproduced from [47], with the permission of AIP Publishing

peak. Similar to the high-stress wafer, the InGaP layer peaks show a different diffuse scattering in the asymmetric 224 reflections. We clearly see the enhanced diffuse scattering along the [110] crystal direction.

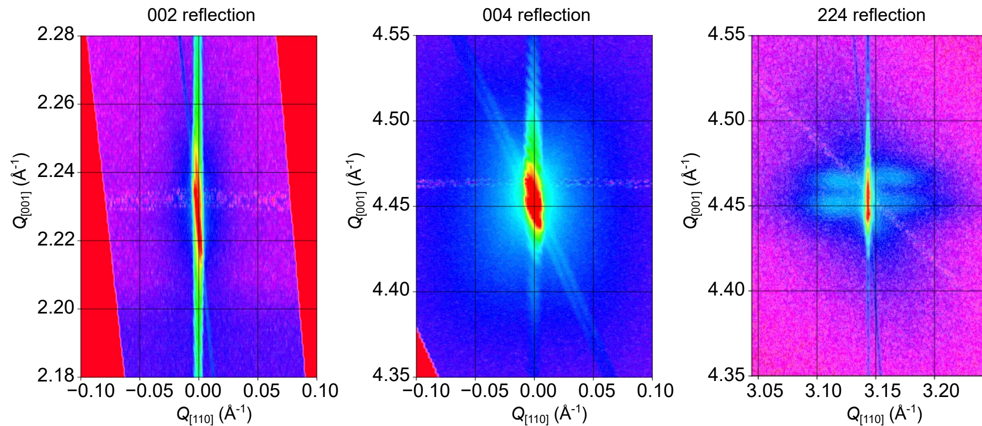

Figure C.5: HRXRD reciprocal space maps depicting the symmetric 002 and 004 and asymmetric 224 reflections of the 2LS wafer for a x-ray beam oriented along the [110] direction. Reproduced from [47], with the permission of AIP Publishing

Table C.1: Heterostructure of the 1HS wafer. Layer-compositions and -thicknesses are extracted by fitting the HRXRD scan of Fig. C.4. One can clearly see deviations from the nominal heterostructure in Tab. C.2. The composition of both InGaP layers differs and they also both have gradient in their In content along the growth direction.

Layer	Repeat	Material	Al content	In content	Thickness (µm)
0	1	GaAs subs.	—	—	—
1	1	AlGaAs	0.99536	—	0.01449
2	41	GaAs	—	—	0.07801
		AlGaAs	0.96612 (top) 0.98612 (bottom)	—	0.09002
3	1	GaAs	—	—	0.07670
4	1	AlGaAs	0.96032	—	1.05490
5	1	GaAs	—	—	0.00100
6	1	InGaP	—	0.46721 (top) 0.42233 (bottom)	0.07762
7	1	AlGaAs	0.98550	—	0.26441
8	1	GaAs	—	—	0.00100
9	1	InGaP	—	0.42227 (top) 0.38401 (bottom)	0.08643
10	1	GaAs	—	—	0.00100

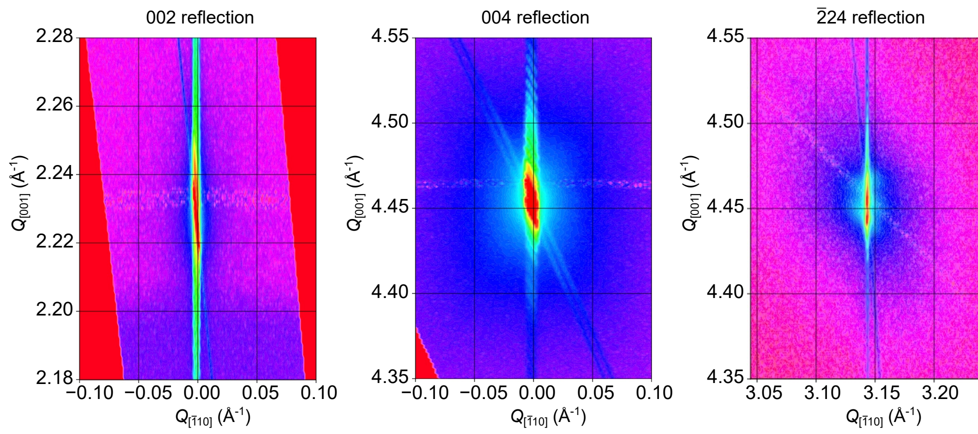

Figure C.6: HRXRD reciprocal space maps depicting the symmetric 002 and 004 and asymmetric $\bar{2}24$ reflections of the 2LS wafer for a x-ray beam oriented along the $[\bar{1}10]$ direction. Reproduced from [47], with the permission of AIP Publishing

Table C.2: Nominal heterostructure composition of the 1HS wafer.

Layer	Repeat	Material	Al content	In content	Thickness (μm)
0	1	GaAs subs.	—	—	—
1	1	AlGaAs	0.92	—	0.2720
2	41	GaAs	—	—	0.0780
		AlGaAs	0.92	—	0.0906
3	1	GaAs	—	—	0.0780
4	1	AlGaAs	0.92	—	1.0653
5	1	GaAs	—	—	0.0010
6	1	InGaP	—	0.41	0.0859
7	1	GaAs	—	—	0.0010
8	1	AlGaAs	0.92	—	0.2646
9	1	GaAs	—	—	0.0010
10	1	InGaP	—	0.41	0.0859
11	1	GaAs	—	—	0.0010

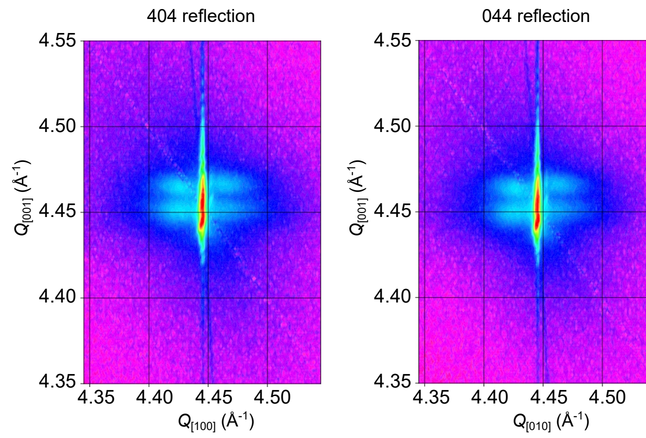

Figure C.7: HRXRD reciprocal space maps depicting 404 and 044 reflection of the 2LS wafer. On the left the beam is along the [100] and on the right along the [010] direction. Reproduced from [47], with the permission of AIP Publishing

Bibliography

[1] D. J. Young, C. A. Zorman, and M. Mehregany. *MEMS/NEMS Devices and Applications*, pages 225–252. Springer, Berlin, Heidelberg, 2004.

[2] K. L. Ekinci, X. M. H. Huang, and M. L. Roukes. Ultrasensitive nanoelectromechanical mass detection. *Applied Physics Letters*, 84(22):4469–4471, 2004.

[3] Y.-T. Yang, C. Callegari, X. L. Feng, K. L. Ekinci, and M. L. Roukes. Zeptogram-scale nanomechanical mass sensing. *Nano Letters*, 6(4):583–586, 2006.

[4] K. Jensen, K. Kim, and A. Zettl. An atomic-resolution nanomechanical mass sensor. *Nature Nanotechnology*, 3(9):533, 2008.

[5] M. S. Hanay, S. Kelber, A. K. Naik, D. Chi, S. Hentz, E. C. Bullard, E. Colinet, L. Duraffourg, and M. L. Roukes. Single-protein nanomechanical mass spectrometry in real time. *Nature Nanotechnology*, 7(9):602, 2012.

[6] J. Chaste, A. Eichler, J. Moser, G. Ceballos, R. Rurali, and A. Bachtold. A nanomechanical mass sensor with yoctogram resolution. *Nature Nanotechnology*, 7(5):301–304, 2012.

[7] H. J. Mamin and D. Rugar. Sub-attonewton force detection at millikelvin temperatures. *Applied Physics Letters*, 79(20):3358–3360, 2001.

[8] J. D. Teufel, T. Donner, M. A. Castellanos-Beltran, J. W. Harlow, and K. W. Lehnert. Nanomechanical motion measured with an imprecision below that at the standard quantum limit. *Nature Nanotechnology*, 4(12):820–823, 2009.

[9] J. Moser, J. Güttinger, A. Eichler, M. J. Esplandiu, D. E. Liu, M. I. Dykman, and A. Bachtold. Ultrasensitive force detection with a nanotube mechanical resonator. *Nature Nanotechnology*, 8(7):493–496, 2013.

[10] M. L. Roukes. Nanoelectromechanical systems face the future. *Physics World*, 14(2):25–32, February 2001.

[11] Y. Tao, P. Navaretti, R. Hauert, U. Grob, M. Poggio, and C. L. Degen. Permanent reduction of dissipation in nanomechanical Si resonators by chemical surface protection. *Nanotechnology*, 26:465501, November 2015.

[12] Y. Tao, J. M. Boss, B. A. Moores, and C. L. Degen. Single-crystal diamond nanomechanical resonators with quality factors exceeding one million. *Nature Communications*, 5:3638, April 2014.

[13] K. Y. Yasumura, T. D. Stowe, E. M. Chow, T. Pfafman, T. W. Kenny, B. C. Stipe, and D. Rugar. Quality factors in micron- and submicron-thick cantilevers. *Journal of Microelectromechanical Systems*, 9(1):117–125, 2000.

[14] T. Faust, J. Rieger, M. J. Seitner, J. P. Kotthaus, and E. M. Weig. Signatures of two-level defects in the temperature-dependent damping of nanomechanical silicon nitride resonators. *Physical Review B*, 89(10):100102, March 2014.

[15] C. Müller, J. H. Cole, and J. Lisenfeld. Towards understanding two-level-systems in amorphous solids: insights from quantum circuits. *Reports on Progress in Physics*, 82(12):124501, October 2019.

[16] G. I. González and P. R. Saulson. Brownian motion of a mass suspended by an anelastic wire. *Acoustical Society of America Journal*, 96:207–212, July 1994.

[17] P.-L. Yu, T. P. Purdy, and C. A. Regal. Control of Material Damping in High-Q Membrane Microresonators. *Physical Review Letters*, 108(8):083603, February 2012.

[18] S. S. Verbridge, J. M. Parpia, R. B. Reichenbach, L. M. Bellan, and H. G. Craighead. High quality factor resonance at room temperature with nanostrings under high tensile stress. *Journal of Applied Physics*, 99(12):124304, June 2006.

[19] T. Faust, P. Krenn, S. Manus, J. P. Kotthaus, and E. M. Weig. Microwave cavity-enhanced transduction for plug and play nanomechanics at room temperature. *Nature Communications*, 3:728, March 2012.

[20] R. A. Norte, J. P. Moura, and S. Gröblacher. Mechanical Resonators for Quantum Optomechanics Experiments at Room Temperature. *Physical Review Letters*, 116(14):147202, April 2016.

[21] A. H. Ghadimi, D. J. Wilson, and T. J. Kippenberg. Radiation and Internal Loss Engineering of High-Stress Silicon Nitride Nanobeams. *Nano Letters*, 17:3501–3505, June 2017.

[22] Y. Tsaturyan, A. Barg, E. S. Polzik, and A. Schliesser. Ultracoherent nanomechanical resonators via soft clamping and dissipation dilution. *Nature Nanotechnology*, 12:776–783, August 2017.

[23] A. H. Ghadimi, S. A. Fedorov, N. J. Engelsen, M. J. Bereyhi, R. Schilling, D. J. Wilson, and T. J. Kippenberg. Elastic strain engineering for ultralow mechanical dissipation. *Science*, 360(6390):764–768, 2018.

[24] A. R. Kermany, G. Brawley, N. Mishra, E. Sheridan, W. P. Bowen, and F. Iacopi. Microresonators with Q-factors over a million from highly stressed epitaxial silicon carbide on silicon. *Applied Physics Letters*, 104(8):081901, February 2014.

[25] T. Watanabe, K. Onomitsu, and H. Yamaguchi. Feedback Cooling of a Strained GaAs Micromechanical Beam Resonator. *Applied Physics Express*, 3(6):065201, June 2010.

[26] K. Onomitsu, M. Mitsuhara, H. Yamamoto, and H. Yamaguchi. Ultrahigh-Q Micromechanical Resonators by Using Epitaxially Induced Tensile Strain in GaNAs. *Applied Physics Express*, 6(11):111201, November 2013.

[27] G. D. Cole, P.-L. Yu, C. Gärtner, K. Siquans, R. Moghadas Nia, J. Schmöle, J. Hoelscher-Obermaier, T. P. Purdy, W. Wieczorek, C. A. Regal, and M. Aspelmeyer. Tensile-strained $In_xGa_{1-x}P$ membranes for cavity optomechanics. *Applied Physics Letters*, 104(20):201908, May 2014.

[28] B. Guha, S. Mariani, A. Lemaître, S. Combrié, G. Leo, and I. Favero. High frequency optomechanical disk resonators in III-V ternary semiconductors. *Optics Express*, 25:24639, October 2017.

[29] I. Ghorbel, F. Swiadek, R. Zhu, D. Dolfi, G. Lehoucq, A. Martin, G. Moille, L. Morvan, R. Braive, S. Combrié, and A. De Rossi. Optomechanical gigahertz oscillator made of a two photon absorption free piezoelectric III/V semiconductor. *APL Photonics*, 4(11):116103, November 2019.

[30] E. A. Sete and H. Eleuch. Controllable nonlinear effects in an optomechanical resonator containing a quantum well. *Physical Review A*, 85(4):043824, April 2012.

[31] I. Wilson-Rae, P. Zoller, and A. Imamoğlu. Laser Cooling of a Nanomechanical Resonator Mode to its Quantum Ground State. *Physical Review Letters*, 92(7):075507, February 2004.

[32] L. Midolo, A. Schliesser, and A. Fiore. Nano-opto-electro-mechanical systems. *Nature Nanotechnology*, 13(1):11–18, January 2018.

[33] J. Bochmann, A. Vainsencher, D. D. Awschalom, and A. N. Cleland. Nanomechanical coupling between microwave and optical photons. *Nature Physics*, 9(11):712–716, November 2013.

[34] K. Schneider, Y. Baumgartner, S. Hönl, P. Welter, H. Hahn, D. J. Wilson, L. Czornomaz, and P. Seidler. Optomechanics with one-dimensional gallium phosphide photonic crystal cavities. *Optica*, 6(5):577, May 2019.

[35] S. Combrié, Q. V. Tran, A. De Rossi, C. Husko, and P. Colman. High quality GaInP nonlinear photonic crystals with minimized nonlinear absorption. *Applied Physics Letters*, 95(22):221108, November 2009.

[36] C. P. Dietrich, A. Fiore, M. G. Thompson, M. Kamp, and S. Höfling. GaAs integrated quantum photonics: Towards compact and multi-functional quantum photonic integrated circuits. *Laser & Photonics Reviews*, 10(6):870–894, 2016.

[37] S. Bogdanov, M. Y. Shalaginov, A. Boltasseva, and V. M. Shalaev. Material platforms for integrated quantum photonics. *Optical Materials Express*, 7(1):111–132, January 2017.

[38] W. Weaver Jr., S. P. Timoshenko, and D. H. Young. *Vibration problems in engineering*. Wiley, 1990.

[39] A. N. Cleland. *Foundations of Nanomechanics: From Solid-State Theory to Device Applications*. Springer, 2002.

[40] S. Schmid, L. G. Villanueva, and M. L. Roukes. *Fundamentals of Nanomechanical Resonators*. Springer, 2016.

[41] Q. P. Unterreithmeier, T. Faust, and J. P. Kotthaus. Damping of Nanomechanical Resonators. *Physical Review Letters*, 105(2):027205, July 2010.

[42] L. G. Villanueva and S. Schmid. Evidence of Surface Loss as Ubiquitous Limiting Damping Mechanism in SiN Micro- and Nanomechanical Resonators. *Physical Review Letters*, 113(22):227201, November 2014.

[43] S. A. Fedorov, N. J. Engelsen, A. H. Ghadimi, M. J. Bereyhi, R. Schilling, D. J. Wilson, and T. J. Kippenberg. Generalized dissipation dilution in strained mechanical resonators. *Physical Review B*, 99(5):054107, 2019.

[44] M. A. Hopcroft, W. D. Nix, and T. W. Kenny. What is the Young's Modulus of Silicon? *Journal of Microelectromechanical Systems*, 19(2):229–238, April 2010.

[45] M. S. Shur, M. Levinshtein, and S. Rumyantsev. *Handbook Series on Semiconductor Parameters, Vol. 2: Ternary and Quaternary III-V Compounds*, volume 2. World Scientific Publishing Co, 1999. See also: http://www.matprop.ru/.

[46] U. Pietsch, V. Holy, and T. Baumbach. *High-Resolution X-Ray Scattering: From Thin Films to Lateral Nanostructures (Advanced Texts in Physics)*. Springer, 2004.

[47] M. Bückle, V. C. Hauber, G. D. Cole, C. Gärtner, U. Zeimer, J. Grenzer, and E. M. Weig. Stress control of tensile-strained $In_{1-x}Ga_xP$ nanomechanical string resonators. *Applied Physics Letters*, 113(20):201903, 2018.

[48] J. W. Matthews, S. Mader, and T. B. Light. Accommodation of Misfit Across the Interface Between Crystals of Semiconducting Elements or Compounds. *Journal of Applied Physics*, 41:3800–3804, August 1970.

[49] R. People and J. C. Bean. Calculation of critical layer thickness versus lattice mismatch for Ge_xSi_{1-x}/Si strained-layer heterostructures. *Applied Physics Letters*, 47:322–324, August 1985.

[50] K. Ozasa, M. Yuri, S. Tanaka, and H. Matsunami. Effect of misfit strain on physical properties of InGaP grown by metalorganic molecular-beam epitaxy. *Journal of Applied Physics*, 68:107–111, July 1990.

[51] C. Baker. *On-chip nano-optomechanical whispering gallery resonators*. PhD thesis, Université Paris Diderot, Laboratoire Matériaux et Phénomenes Quantiques, 2013.

[52] K. Nojiri. *Dry Etching Technology for Semiconductors*. Springer, 2015.

[53] Y.-S. Lee, M. DeVre, D. Lishan, and R. Westerman. Smooth, Anisotropic Etching of Indium Containing Structures Using a High Density ICP System. Technical report, CS MANTECH, Inc. 2003 International Conference on Compound Semiconductor Manufacturing Technology, 2003.

[54] S. Combrié, S. Bansropun, M. Lecomte, O. Parillaud, S. Cassette, H. Benisty, and J. Nagle. Optimization of an inductively coupled plasma etching process of GaInP/GaAs based material for photonic band gap applications. *Journal of Vacuum Science & Technology B: Microelectronics and Nanometer Structures Processing, Measurement, and Phenomena*, 23(4):1521–1526, 2005.

[55] N. G. Einspruch and D. M. Brown. *Plasma processing for VLSI*, volume 8 of *VLSI Electronics Microstructure Science*. Academic Press, 1st edition, 1984.

[56] J.-H. Kim, D. H. Lim, and G. M. Yang. Selective etching of AlGaAs/GaAs structures using the solutions of citric acid/H_2O_2 and de-ionized H_2O/buffered oxide etch. *Journal of Vacuum Science Technology B: Microelectronics and Nanometer Structures*, 16:558–560, March 1998.

[57] P. Kumar, S. Kanakaraju, and D. L. Devoe. Sacrificial etching of $Al_xGa_{1-x}As$ for III V MEMS surface micromachining. *Applied Physics A: Materials Science & Processing*, 88:711–714, September 2007.

[58] L. Midolo, T. Pregnolato, G. Kiršanskė, and S. Stobbe. Soft-mask fabrication of gallium arsenide nanomembranes for integrated quantum photonics. *Nanotechnology*, 26:484002, December 2015.

[59] G. C. DeSalvo, C. A. Bozada, J. L. Ebel, D. C. Look, J. P. Barrette, C. L. A. Cerny, R. W. Dettmer, J. K. Gillespie, C. K. Havasy, T. J. Jenkins, K. Nakano, C. I. Pettiford, T. K. Quach, J. S. Sewell, and G. D. Via. Wet Chemical Digital Etching of GaAs at Room Temperature. *Journal of The Electrochemical Society*, 143(11):3652–3656, 1996.

[60] J. Y. Kim and Chang-Jin Kim. Comparative study of various release methods for polysilicon surface micromachining. In *Proceedings IEEE The Tenth Annual International Workshop on Micro Electro Mechanical Systems. An Investigation of Micro Structures, Sensors, Actuators, Machines and Robots*, pages 442–447, January 1997.

[61] R. Maboudian and R. T. Howe. Critical Review: Adhesion in surface micromechanical structures. *Journal of Vacuum Science Technology B: Microelectronics and Nanometer Structures*, 15:1–20, January 1997.

[62] V. C. Hauber. Herstellung von nanomechanischen Balkenresonatoren hoher Güte aus InGaP und Untersuchung der richtungsabhängigen Zugspannung des Krsitallinen Materials. Master's thesis, University of Konstanz, 2016.

[63] J. M. Dallesasse, N. El-Zein, N. Holonyak, Jr., K. C. Hsieh, R. D. Burnham, and R. D. Dupuis. Environmental degradation of $Al_xGa_{1-x}As$-GaAs quantum-well heterostructures. *Journal of Applied Physics*, 68:2235–2238, September 1990.

[64] J. M. Dallesasse and N. Holonyak, Jr. Oxidation of Al-bearing III-V materials: A review of key progress. *Journal of Applied Physics*, 113(5):051101–051101, February 2013.

[65] D. L. Huffaker, D. G. Deppe, C. Lei, and L. A. Hodge. Sealing AlAs against oxidative decomposition and its use in device fabrication. *Applied Physics Letters*, 68:1948–1950, April 1996.

[66] J. Cheng and N. K. Dutta. *Vertical-Cavity Surfae-Emitting Lasers: Technology and Applications*. CRC Press, 2000.

[67] K. L. Ekinci and M. L. Roukes. Nanoelectromechanical systems. *Review of Scientific Instruments*, 76(6):061101, June 2005.

[68] K. L. Ekinci. Electromechanical Transducers at the Nanoscale: Actuation and Sensing of Motion in Nanoelectromechanical Systems (NEMS). *Small*, 1(8-9):786–797, 2005.

[69] V. M. Kaganer, R. Köhler, M. Schmidbauer, R. Opitz, and B. Jenichen. X-ray diffraction peaks due to misfit dislocations in heteroepitaxial structures. *Physical Review B*, 55:1793–1810, January 1997.

[70] S. Dai, J. Zhao, M.-r. He, X. Wang, J. Wan, Z. Shan, and J. Zhu. Elastic Properties of GaN Nanowires: Revealing the Influence of Planar Defects on Young's Modulus at Nanoscale. *Nano Letters*, 15:8–15, January 2015.

[71] Y. Chen, T. Burgess, X. An, Y.-W. Mai, H. H. Tan, J. Zou, S. P. Ringer, C. Jagadish, and X. Liao. Effect of a High Density of Stacking Faults on the Young's Modulus of GaAs Nanowires. *Nano Letters*, 16:1911–1916, March 2016.

[72] M. Bückle, Y. S. Klaß, F. Nägele, R. Braive, and E. M. Weig. Universal dependence of tensile stress on the length of nanomechanical string resonators. In preparation, 2020.

[73] N. Maluf and K. Williams. *An Introduction to Microelectromechanical Systems Engineering*. Artech House, Boston, 2nd edition, 2004.

[74] M. J. Bereyhi, A. Beccari, S. A. Fedorov, A. H. Ghadimi, R. Schilling, D. J. Wilson, N. J. Engelsen, and T. J. Kippenberg. Clamp-Tapering Increases the Quality Factor of Stressed Nanobeams. *Nano Letters*, 19(4):2329–2333, April 2019.

[75] T. C. Taylor and F. L. Yuan. Thermal stress and fracture in shear-constrained semiconductor device structures. *IRE Transactions on Electron Devices*, 9(3):303–308, May 1962.

[76] O. M. Jadaan, N. N. Nemeth, J. Bagdahn, and W. N. Sharpe Jr. Probabilistic Weibull behavior and mechanical properties of MEMS brittle materials. *Journal of Materials Science*, 38(20):4087–4113, 2003.

[77] A. Kaushik, H. Kahn, and A. H. Heuer. Wafer-level mechanical characterization of silicon nitride MEMS. *Journal of Microelectromechanical Systems*, 14(2):359–367, 2005.

[78] I. Wilson-Rae. Intrinsic dissipation in nanomechanical resonators due to phonon tunneling. *Physical Review B*, 77(24):245418, June 2008.

[79] D. Parrain, C. Baker, G. Wang, B. Guha, E. Gil Santos, A. Lemaître, P. Senellart, G. Leo, S. Ducci, and I. Favero. Origin of optical losses in gallium arsenide disk whispering gallery resonators. *Optics Express*, 23(15):19656–19672, 2015.

[80] B. Guha, F. Marsault, F. Cadiz, L. Morgenroth, V. Ulin, V. Berkovitz, A. Lemaître, C. Gomez, A. Amo, S. Combrié, B. Gérard, G. Leo, and I. Favero. Surface-enhanced gallium arsenide photonic resonator with quality factor of 6 $\times$ 10ˆ6. *Optica*, 4(2):218, February 2017.

[81] M. Hamoumi, P. E. Allain, W. Hease, E. Gil-Santos, L. Morgenroth, B. Gérard, A. Lemaître, G. Leo, and I. Favero. Microscopic Nanomechanical Dissipation in Gallium Arsenide Resonators. *Physical Review Letters*, 120(22):223601, June 2018.

[82] M. J. Seitner, K. Gajo, and E. M. Weig. Damping of metallized bilayer nanomechanical resonators at room temperature. *Applied Physics Letters*, 105(21):213101, November 2014.

[83] Q. P. Unterreithmeier, E. M. Weig, and J. P. Kotthaus. Universal transduction scheme for nanomechanical systems based ob dielectric forces. *Nature*, 458, 2009.

[84] G. Bauer, J. H. Li, and V. Holy. High resolution x-ray reciprocal space mapping. *Acta Physica Polonica A*, 89(2):115–127, February 1996. II International School and Symposium on Physics in Materials Science Surface and Interface Engineering, Jaszowiec, Poland, July 17-23, 1995.